CERN-LHCC-2014-NNN
CMS-TDR-MMM
ISBN 978-92-9083-396-3
23 June 2014; Draft V02-00

CMS TECHNICAL DESIGN REPORT FOR THE MUON ENDCAP UPGRADE: GE1/1 - THE STATION 1 GEM PROJECT

This report describes the technical design and outlines the expected performance of the Phase 2 Upgrade of the CMS Muon System with Gas Electron Multiplier (GEM) detectors to be installed in the first endcap station during the 2nd LHC Long Shutdown (LS2). After LS2, the LHC luminosity and pileup level will be double the design value. The upgrade is designed to improve the muon trigger and tracking performance at high luminosity, and to add redundancy to the muon system in the $1.6 < |\eta| < 2.4$ region, where the number of muon hits is actually least, while the background rates are highest and the muon trajectory bending is reduced. GEM detectors have been identified as a suitable technology to sustain the specific high radiation environment in that region. The first muon endcap station will be instrumented in the aforementioned η region with a double layer of triple-GEM chambers. The chamber front-end electronics is based on the digital VFAT3 chip and provides fast input for the level-1 muon trigger and full granularity information for offline muon reconstruction. The expected performance of the muon system after this upgrade is discussed, including a study of some benchmark physics channels. The planning for the detector construction, testing, integration into CMS is presented, including the project schedule, cost and organization.

Editors

M. Abbrescia, A. Sharma and M. Tytgat

Chapter Editors

P. Aspell, L. Benussi, S. Bianco, O. Bouhali, A. Cimmino, A. Colaleo, G. De Lentdecker, P. Giacomelli, J. Hauser, K. Hoepfner, M. Hohlmann, H. Hoorani, P. Karchin, A. Lanaro, M. Maggi, A. Marinov, A. Safonov, A. Sharma and M. Tytgat

Language Editors

M. Hohlmann and P. Karchin

Cover Design

S. Cittolin

Acknowledgments

We would like to thank the technical staff from the various institutions for the design, R&D and testing of all components of this upgrade.

We thank G. Alverson for tireless technical assistance in the preparation of this document.

We acknowledge the warm support received from the CMS management team and the CMS offline and computing projects.

Contents

Chapter 1

Introduction

Editors: J. Hauser, K. Hoepfner

1.1 Motivation for Additional Detectors in the Muon Endcaps

The CMS muon system was originally designed as a highly hermetic and redundant muon system, composed of three detection technologies [REF MU TDR]. Precision measurements are provided by Drift Tubes (DT) in the barrel, covering acceptances up to $|\eta|$¡1.2, and Cathode Strip Chambers (CSC) in the endcaps covering 1.0¡$|\eta|$¡2.4. Resistive Plate Chambers (RPC) ensure adequate redundancy and triggering up to $|\eta| \mathit{implementedbeyond}$—$\eta|$¿1.6 where the background particle rates are highest and the bending in the magnetic field is lowest.

During most of LHC run 1, the inclusive muon trigger covered the region up to the instrumentation boundary of $|\eta|$=2.4 with typical thresholds of pT$\sim$20-25 GeV. Several analyses excluded the region between 2.1 and 2.4 to avoid mis-reconstructed muons which occur with a relatively high frequency due to the challenging conditions.

This TDR proposes to re-establish the originally foreseen redundancy in the forward region beyond 1.6 based on modern, high-resolution and fast gas detectors capable to operate up to MHz rates. While at $|\eta|$=0 there are 44 individual DT layers for precise position measurements and 12 RPC layers for primarily triggering, in the region 1.6¡$|\eta|$¡2.4 only 24 CSC layers are present. The forward region $|\eta|$¿1.6 is especially challenging: particle rates can be as high as MHz/cm^2 and the magnetic bending is reduced. This leads to reduced resolution and longevity issues and exceeds in some cases the capabilities of existing electronics.

Performance studies with muon gun samples show an improvement in the the efficiency up to 4% by adding the track segments from GE1/1. The charge misidentification probability (rising steeply with momentum) improves up to 40% for medium - high pT muons. The benefit of including additional hits can be up to 15% for low-medium pT standalone muons. CHECK NUMBERS FOR LATEST UPDATE.

The data recorded between LS2 and LS3 should yield important precision measurements of the Higgs boson properties as well as extending the search for new physics. At this time the phase-II track trigger will not yet be available. For many signatures, such as H4Mu and H2Tau, about 20% of the events have one or more final state muons in the GE1/1 instrumented region. Those events would be lost if the existing CSC chambers mailfunction or perform at reduced efficiency. In the endcaps CSCs, geometrical gaps are seen in the eta projection, resulting in no hits along the muon track. Inefficiencies could occur along the boundaries of CSC high voltage segments. Concerns exist for the eventual availability of CF_4, a vital component of the CSC gas mixture contributing to their fast drift velocity and preventing aging. Redundancy, as existing everywhere else in the muon system, would guarentee those events.

Another issue derives from the muon trigger: pT mis-measurements and multiple scattering in the iron yoke contribute fake triggers to the high pT tail of the single muon trigger rate (shown in red in Fig. 1.1) thus requiring to increase the trigger threshold to stay within the allocated bandwidth. A large trigger reduction is achievable when measuring the bending angle in forward region, a concept already is successfully applied in the CMS muon barrel but - up to now - not applicable in the forward since the existing CSC chambers are too thin. Adding GE1/1 chambers significantly increases the lever arm and by combining ME1/1 and GE1/1 in the same station allows for a good separation of soft and harder muons. Considerably lower fake contributions reduce the trigger rate which allows to lower the trigger threshold (shown in green in Fig. 1.1). For some physics channels, such as H2Tau, a trigger threshold of about 15 GeV nearly doubles the sensitivity since the muons from the subsequent tau decay(s) are of low-medium pT and thus strongly affected by the trigger threshold. It should be noticed that the bending angle measurement is most precise in station 1, else radial B-field and multiple scattering quickly diminish the discrimination.

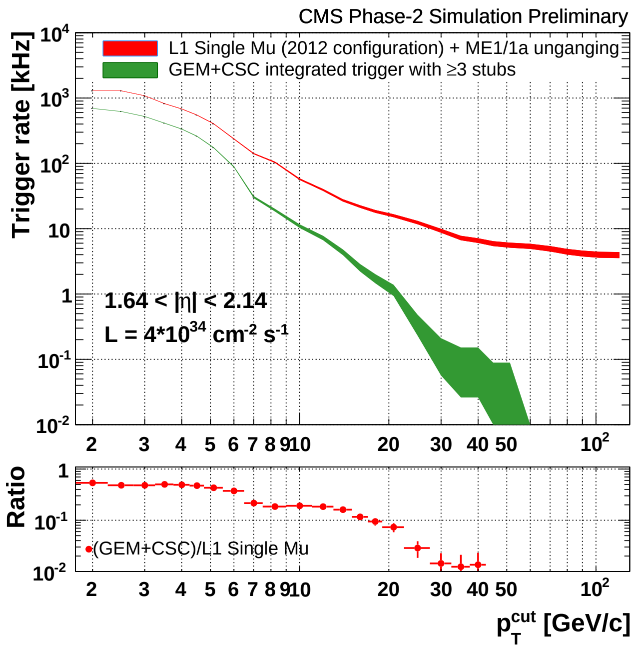

Figure 1.1: Trigger rates before (red) and after (green) the GE1/1 upgrade.

The proposed upgrade targets the following improvements:

- Re-establish the redundancy in the difficult region between 1.5¡$|\eta|$¡2.2 by using the space originally foreseen for RPC detectors which were not built due to concerns about hit rate capability and due to cost concerns.
- Improve tracking performance in the high rate environment where the background rates of all types are highest and the magnetic bending is reduced.
- The combined operation of CSC and GEM detectors allows for measuring the bending angle at trigger level, thus strongly reducing the rate of mis-measured muons driving the trigger rate.

1.2 Overview of the upgrade project

The chosen technology for the upgrade discussed in this TDR are Gas Electron Multipliers (GEM) where amplification occurs in the narrow wholes of a thin (50 μm) kapton foil placed inbetween two conductive layers. The foil is perforated with biconical holes of typically 70 μm diameter in a hexagonal pattern with 140 μm pitch. Three subsequent stages/foils allow for a reasonable amplification at every stage/foil and providing a high total amplification of about 15000 with operational voltages across the GEM foil of 380-400 V which is far from any critical value. A pair of such triple-GEM chambers is combined to a so-called superchamber that complement the existing ME1/1 detectors.

Each superchamber covers a 10-degree sector with two readout points spaced 20 mm from each other, and a total lever arm (for reconstruction) of 88 mm. In each endcap, 36 superchambers will be installed, making the construction a project of 72 superchambers or 144 individual GEM triple-layer detectors. The superchambers are to be installed in the prepared slots formerly foreseen for RPCs, in the gap between the YE1 nose and the CSC ME1/1 chambers (see Fig. 1.2). The superchambers alternate in phi between long (1.5 - 2.2) and short (1.6 - 2.2) versions of η range. This geometry has been implemented in detector simulation and used for performance studies.

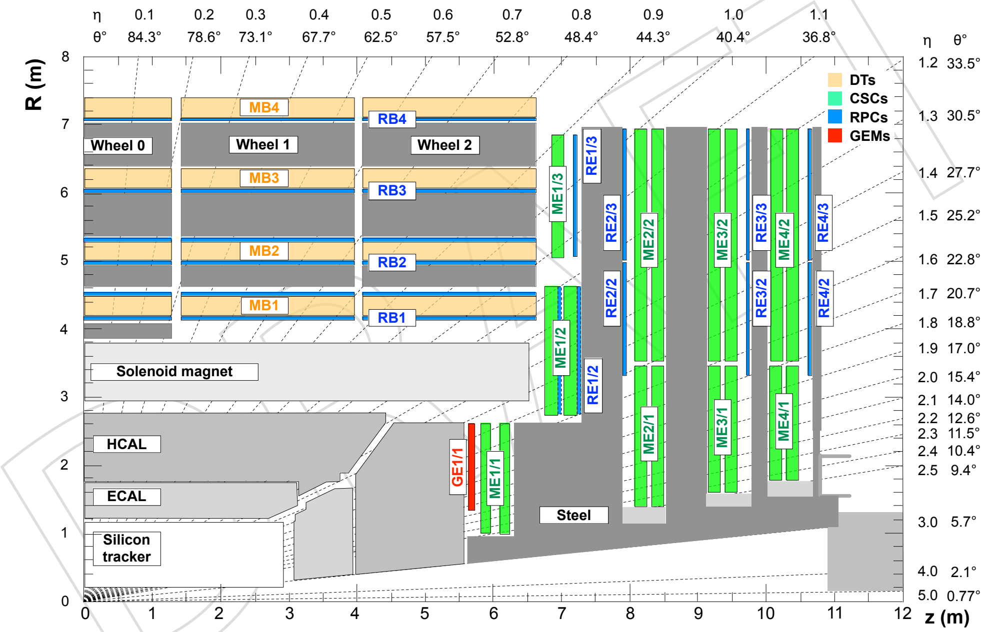

Figure 1.2: Location of the proposed GE1/1 detector in the CMS Muon system.

Small size GEM detectors have demonstrated their rate capability and robustness in the past. To cover the large area of XXX m^2 in CMS, new technologies for large size detectors had to be developed. Within the CMS GEM R&D, cost-effective industrial production of large size Kapton foils was demonstrated and shown efficiencies of >98% in testbeams. A novel technique has recently been developed where three foils are mounted into a single stack under tension, keeping a constant inter-GEM spacing. Since no gluing is involved, a large size chamber is assembled in about two hours, compared to one week in gluing technique. As an additional benefit, such chamber can be re-opened if needed.

The off-detector electronics provides the interface from the detector and its VFAT3 front-end electronics to the CMS DAQ and trigger systems. It is based on the preferred CMS μTCA standard and fully compatible (and integrated) in CMS. Trigger information is sent directly to the CSC Trigger Mother Board (TMB) where GEM and CSC data are combined at the earliest stage of CSC trigger processing. This trigger path will use existing optical fibers located along the ME1/1 detectors. With this version of the readout, spatial resolutions of about 250 μm have been measured which is sufficient for the CMS application where resolution is limited by multiple scattering in the iron return yoke. In principle, resolutions of the order of 100 μm are achievable.

Chapter 2

GE1/1 GEM Chambers

Editors: L. Benussi, M. Hohlmann

2.1 Technology Overview

A Gas Electron Multiplier [**?**] is a thin metal-clad polymer foil chemically perforated by a high density of microscopic holes. The polyimide (Kapton [**?**]) used as the bulk material of the foil is 5 μm thick and has a dielectric constant of 3.5; the cladding metal is copper. As shown Fig. 2.1 (left), the GEM holes have outer diameters of the order of 70 μm and are spaced with a pitch of 140 μm.

A Triple-GEM chamber consists of a stack of three GEM foils placed at a relative distance of a few mm and immersed in a counting gas. The voltage applied across the two copper faces of a foil produces an electric field as high as $\sim$ 80 kV/cm in the GEM hole as seen in Fig. 2.1 (right). The electrons produced by a charged particle passing through the chamber due to ionization of the counting gas drift towards the holes and once they start to experience the very intense electric field in the holes, they acquire enough kinetic energy to produce secondary ionization in the gas. This produces an electron avalanche process, which induces an electrical signal on the readout strips. A schematic view of this operation principles is given in Fig.2.2.

Typical dimensions of the different regions in a Triple-GEM chamber are as follows: Drift field region of 3 mm, spaces of 1 mm and 2 mm in the electron transfer gaps, and a 1 mm space in the induction field region. A standard gas mixtures for operating the Triple-GEM is

2.1.1 Requirements on GE1/1 chamber performances and design

The desired trigger and physics performances outlined in Ch.1 impose the following fundamental requirements on the detection performance of the GE1/1 chambers:

- Maximum geometric acceptance within the given CMS envelope.
- Rate capability of 10 kHz/cm^2 or better.
- Single-chamber efficiency of 97% or better for detecting minimum ionizing particles.
- Angular resolution of 300 μrad or better in the azimuthal direction.
- Timing resolution of 10 ns or better for a single chamber.
- Gain uniformity of 15% or better across a chamber and between chambers.
- No gain loss due to aging effects after 200 mC/cm^2 of integrated charge.

We briefly review the rationale for these requirements: Clearly, maximum acceptance will yield maximum physics yield. The maximum expected hit rate within the GE1/1 acceptance is about

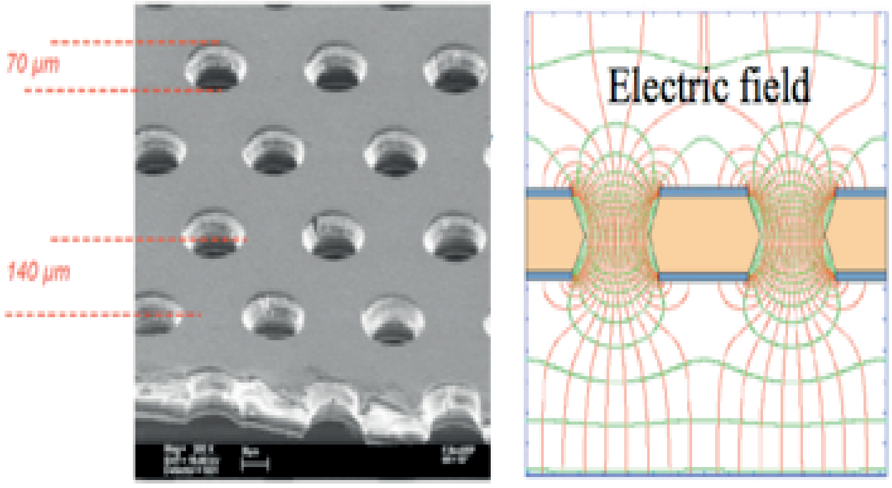

Figure 2.1: A SEM picture of a GEM foil. The hole size is 70 μm and the hole pitch is 140 μm [**?**].

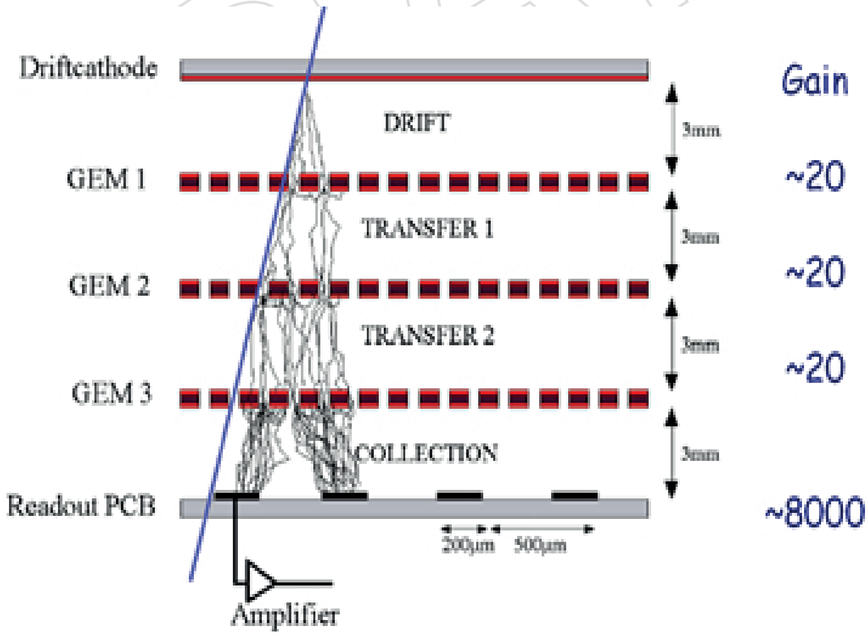

Figure 2.2: Principle of operation of a Triple-GEM chamber[**?**].Need to change "'collection"' to "'induction" in this figure!

5 kHz/cm^2 for HL-LHC running at 14 TeV and 5 $\times 10^{34}$ cm^{-2}s^{-1}. Multiplying with a safety factor of two then requires a hit-rate cabability of 10 kHz/cm^2. With 97% individual chamber efficiency, a "superchamber" that contains two chambers will have an efficiency above 99.9% when the signals from the two chambers are combined as a logical OR. An azimuthal resolution of 300 μrad or better will not significantly smear the difference $\Delta\phi = \phi_{GE1/1} - \phi_{ME1/1}$ of the angular muon positions measured in GE1/1 and ME1/1. Consequently, a resolution of that magnitude will enable the trigger to discriminate high-p$_T$ muons from low-p$_T$ muons reliably. For a binary readout, 300 μrad resolution corresponds to a pitch of $\sqrt{12} \cdot 300\mu$rad = 1040 μrad for trigger strips. At the outer radius (r = 2.6m) of the GE1/1 chambers, this azimuthal resolution of 300 μrad corresponds to a 0.8 mm resolution in the azimuthal $\hat{\phi}$ direction. Since two chambers can provide independent timing information that can also be combined wth timing provided by the CSCs, a $\leq$ 10 ns time resolution for a single chamber is sufficient to reliably match GE1/1 hits to ME1/1 stubs in time when running with a 25 ns bunch crossing time at the LHC. A uniform chamber response will ensure that there are no geometrical trigger or reconstruction biases. The gain of a single GEM foil typically varies across the foil surface by 5-8% due to intrinsic variations in hole diameters that stem from the production process. The corresponding typical gain variation in a triple-GEM detector is $\sqrt{3}$ times larger, i.e. about 10-15%. The chambers should not incur significant additional response non-uniformities due to any other factors. The chambers must be able to integrate a charge of 200 mC/cm^2 over their lifetime without any gain loss or other loss in reponse. The charge expected to be integrated in the GE1/1 sector at highest η over 20 years of operation at the HL-LHC is about 100 mC/cm^2. A calculation of this estimated integrated charge value is given in appendix B. The stated requirement of 200 mC/cm^2 includes an additional safety factor of two.

THE ABOVE CLAIMS ON SPACE AND TIME RESOLUTION ETC. AND HOW THEY ARE WORDED SHOULD BE CAREFULLY REVIEWED (MH).

In addition, several technical constraints and requirements need to be taken into account in the chamber design. As a baseline, it must be possible to operate the chambers using only counting gases that have low global warming impact. The material budget must be low enough so that multiple scattering within the GE1/1 itself will not affect the muon bending measurement in the GE1/1–CSC trigger. Sufficiently small readout segmentation in η, i.e. along the readout strips, is needed to allow the GE1/1–CSC trigger to remove CSC ghosts effectively when reconstructing events with multiple muon hits in a CSC chamber. The chambers must be designed so that a superchamber is less than 10cm thick and will easily fit into the available slot in the muon endcap nose. The on-chamber service interfaces must be layed out so that pre-exisiting cabling and tubing infrastructure can be used effectively.

2.1.2 Gas Electron Multiplier principles

This sections still needs to be edited - MH

In this section, we present studies of the transport parameters for two gas mixtures, ($Ar/CO_2/CF_4$) and (Ar/CO_2) in the ratios 45 : 15 : 40 and 70 : 30 respectively. Some discussions on transport properties in gaseous detectors can be found here[**?**]. Recently GEM detectors have been operated with $Ar/CO_2/CF_4$ successfully in a high rate environment in the LHCb experiment[**?**], and with Ar/CO_2 in a 70 : 30 ratio in the TOTEM experiment[**?**]. We are investigating the usage of $Ar/CO_2/CF_4$ as this gas combines a high drift velocity along with a small Lorentz angle (almost comparable to Ar/CO_2), which will be useful for triggering and other physics studies in the forward region. Also, this gas was found to give a better time resolution of $\sim$ 5 ns as compared to Ar/CO_2 which gave a time resolution of $\sim$ 10 ns [**?**]. We do a feasibility study of these gas mixtures for the CMS scenario. Since CMS has a magnetic field of 4 T in particular, we would like to study the effect of the magnetic field and the effect of the angle between the E-field and B-field. Possible concerns about CF_4 usage and studies about possible alternative gas mixtures with low environmental impact parameter but still CMS compliant in tems of detector performances will be discussed in section 2.3.5.3.

When electrons and ions in a gas are subjected to an electric field, they move on an average along the electric field, but individual electrons deviate from the average due to scattering on the atoms and molecules of the gas. Scattering leads to variations in velocity, called longitudinal diffusion, and to lateral displacements, called transverse diffusion. The scattering process in each direction can to a good approximation be considered Gaussian on a microscopic scale. Electric field affects the transverse and longitudinal diffusion differently and so the two coefficients are plotted separately in the figures. In cold gases like carbon-dioxide for example, the diffusion is small, while drift velocity is low and unsaturated for values of electric fields which are usually used in gas detectors. Warm gases like argon on the other hand, have a higher diffusion, but when they are mixed with polyatomic/organic gases having vibrational and rotational modes, diffusion is reduced in most cases, while the drift velocity is increased.

Fig. 2.3 shows the diffusion coefficients for two gas mixtures as a function of the electric field. As can be seen from the plot, the diffusion in the mixture $Ar/CO_2/CF_4$ is lower, as expected, because of a higher polyatomic gas component; both CF_4 and CO_2 having vibrational modes which contribute to lowering the diffusion. CF_4 is advantageous to use in a high-rate environment because of its high drift velocity but it suffers from electron attachment. Therefore CO_2 is used to "cool" the electrons and reduce the electron attachment which occurs in CF_4.

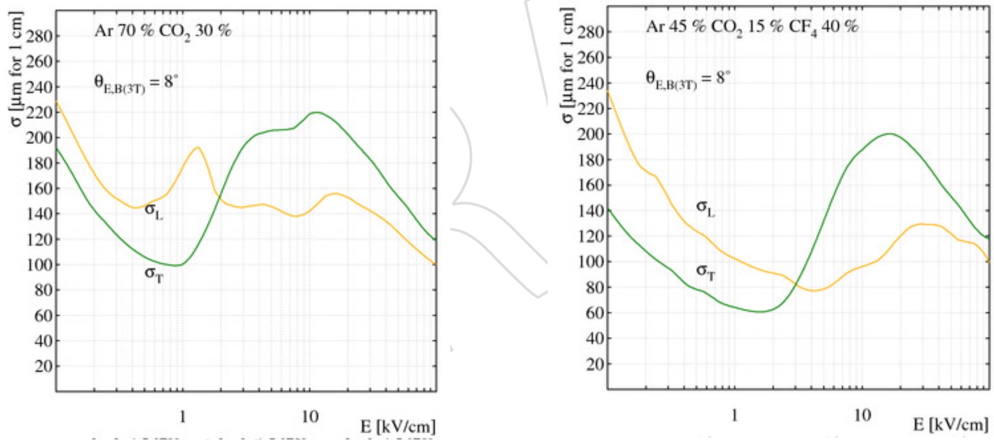

Figure 2.3: Diffusion coefficient for two different gas mixtures under study in presence of magnetic field and with angle $\theta(E, B) = 8°$

In Fig. 2.4, the diffusion coefficients can be seen for magnetic fields of 0 T and 3 T. The effect of the magnetic field is to reduce the transverse diffusion coefficient w.r.t to its direction, while the longitudinal coefficient is unchanged. This effect is seen in the two figures.

In the presence of both an electric field, and a magnetic field, the electrons are deflected due to the magnetic field and drift along a direction at an angle to the electric field, called the Lorentz angle. It is the angle between the electric field and drifting electron. Too large a Lorentz angle leads to worsening of the spatial resolution, although a small Lorentz angle may give better spatial resolution due to charge sharing in the readout strips. Knowledge of this angle is important in order to correct for this effect and improve spatial resolution. The Lorentz angle can be seen in Fig. 2.5, for the gas mixture $Ar/CO_2/CF_4$ for two $\theta_{(E,B)}$ angles in order to show

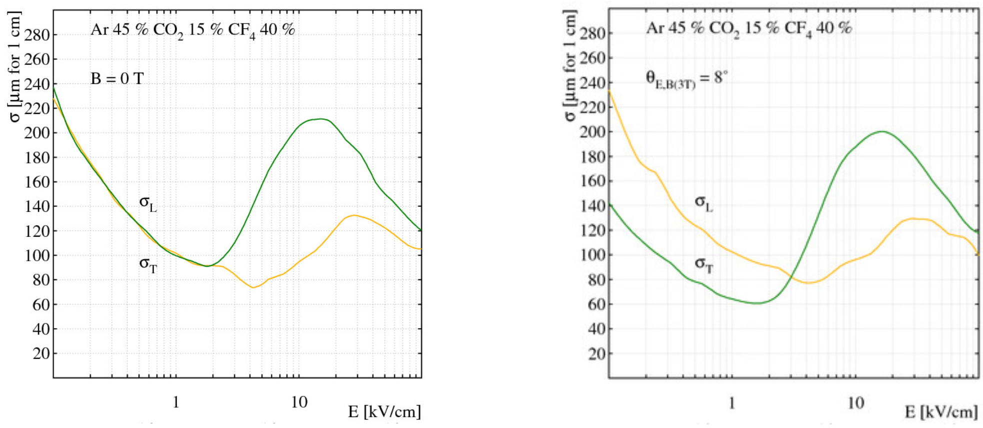

Figure 2.4: Diffusion coefficients for magnetic fields = 0T and 3T with $\theta(E, B) = 90°$.

the expected range of Lorentz angles we can expect in this gaseous mixture.

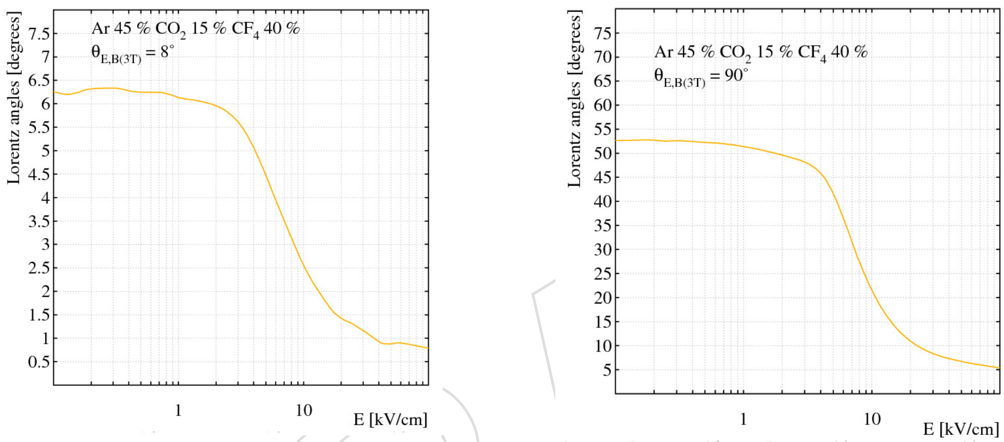

Figure 2.5: Lorentz angles for the gas mixture $Ar/CO_2/CF_4$ for the angles $\theta(E, B) = 8°$ (left) and $\theta(E, B) = 90°$ (right) for a magnetic field of 3 T.

The diffusion effect leads to variations in drift velocity. In Fig. 2.6 shows a comparison of simulation results with experimental LHCb test beam results[**?**]for different gas mixtures. The $Ar/CO_2/CF_4$ mixture is a faster gas due to the addition of the CF_4 gas.

2.1.3 Choice of GEM technology for GE1/1 as motivated by other experiments

We briefly review the experience with GEM technology that exists within the community. GEM detectors have been operated successfully and long-term in several major HEP and nuclear physics experiments, i.e. COMPASS, PHENIX, STAR, TOTEM, and LHC-b. The main features of the GEM applications in those experiments are highlighted below.

- **COMPASS:** This is the pioneering experiment for GEM technology. It is the first high-rate experiment to use GEM detectors[1]. Running at the CERN SPS, COMPASS has been employing 22 medium-size Triple-GEM detectors with 3/2/2/2 mm gap sizes in 11 inner tracking stations. Detectors are operated with Ar/CO_2 70:30 at a gas gain around 8,000 and are read out with two-dimensional Cartesian strips and APV25 chips. The detectors operate at rates up to 2.5 MHz/cm^2, which corresponds to roughly 1000 times the expected rate for the CMS GE1/1. Operating with two OR'ed GEM trackers, each tracking station has an efficiency of 97.5%. A single COMPASS GEM achieves about 70 μm spatial resolution and 12 ns time reso-

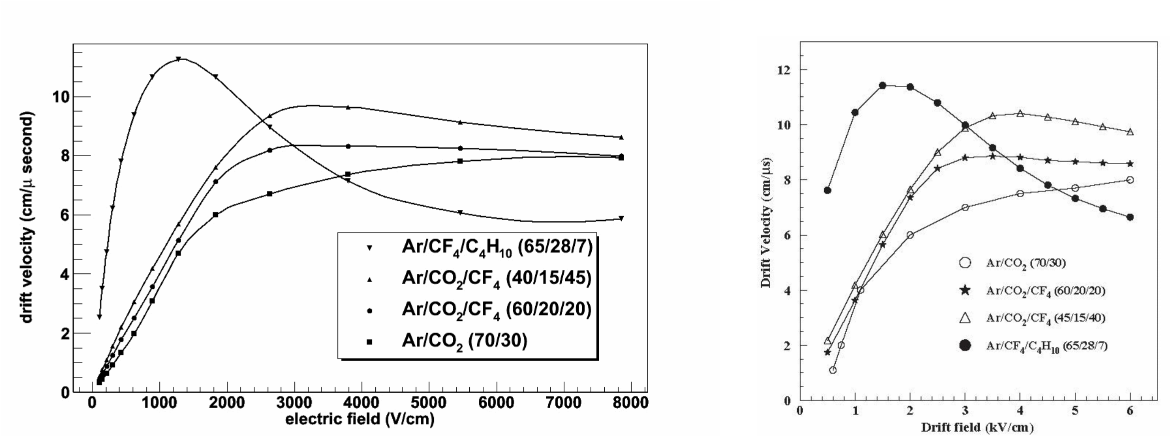

Figure 2.6: The drift velocities for various gas mixtures from simulation and the experimental values from LHCb studies. The simulation shows good agreement with the experimental results.

lution. During the 2002-2007 running period the detectors accumulated total charges around 200 mC/cm^2 without any gain drop while in earlier bench tests with x-rays 700 mC/cm^2 had been collected without any observed gain loss. COMPASS also operated five small-size GEM trackers with 1 mm^2 pixel readout[2] that were exposed to muon rates up to 12 MHz/cm^2 in the 2008/09 COMPASS runs and achieved 7 ns time resolution.

- **PHENIX:** This experiment operated 20 medium-size Triple-GEM detectors at RHIC as a "hadron-blind" detector system[3] for electron identification. A special feature of this system was a reverse bias of the HV between drift mesh and first GEM, which desensitized the GEM to charged particles, while a CsI coating on the first GEM made the detector sensitve to Cherenkov radiation from electrons. The detector was operated in pure CF_4 and achieved a hadron rejection factor of 50 in the 2010 PHENIX run.
- **STAR:** Since late 2012, STAR has been operating 24 medium-size Triple-GEM detectors read out with r-ϕ strips and APV25 chips as a forward tracker[4] at RHIC. GEM foils are shaped as circular quadrants and were produced industrially in the USA.
- **TOTEM:** This experiment employs 20 medium-size Triple-GEM detectors of semi-circular shape that are read out with concentric strips and radial pads and VFAT2 chips. These detectors form two T2 telescopes for charged-particle tracking and triggering in the very forward region at the LHC. They were exposed to a total fluence of a few 10^{13}/cm^2 particles during the 2012 LHC run and had sustained a total ionizing dose of about 5×10^4 Gy by the end of the 2012 LHC run while performing as expected[5].
- **LHCb:** The LHCb experiment employs 12 pairs of medium-size Triple-GEM detectors with 3/1/2/1 mm gap sizes as the inner section of the LHCb M1 muon station, which is located in immediate vicinity of the beam pipe. Using a pad readout, this GEM system produces input for the LHCb L0 muon trigger. Unusual for a muon station, this subdetector is located in front of the calorimeters rather than behind them. Consequently, it sustains rather high rates for a muon detector of up to 500 kHz/cm^2. It operates with an $Ar/CO_2/CF_4$ 45:15:40 gas mixture that is one of the mixtures being considered for the CMS GE1/1. Read out with TDCs and running at a gain around 4,300, the GEMs have a time resolution of 4 ns when the signals

from two paired detectors are logically OR'ed and an efficiency of 97-99% in a 20ns time window. The most irradiated LHCb GEM detector has integrated about 120 mC/cm^2 during the 2010-12 LHC running period without signs of aging[6]. This value happens to correspond closely to the GE1/1 requirement for ten years of running at the HL-LHC (see section 2.1.1).

This strong track record for GEMs in high-rate applications for HEP and NP experiments demonstrates that GEMs represent a mature and robust technology for high-rate experiments. The CMS GE1/1 project represents the next major step in the evolution of GEM detector systems by going from systems with a small number of medium-size detectors to a large number of large-size detectors; it builds mainly upon the more recent experiences with the LHCb and TOTEM GEMs.

2.2 GE1/1 prototyping results

2.2.1 R&D program on full-size GE1/1 prototypes

The crucial first step in the 5-year R&D program that led to this design report was a demonstration that large-area GEM foils can indeed be manufactured reliably and that Triple-GEM detectors built with such foils can satisfy the performance requirements listed in section 2.1.1. Five generations of prototype detectors (Fig. 2.7) were built and tested in 2010-14 with one generation being developed every year based on the experience with the previous generation(give all chamber-related papers from CMS GEM coll. here). Since the GE1/1 prototype performances discussed below are obtained from tests of different prototype generations, we briefly review the evolution of the GE1/1 detector prototypes.

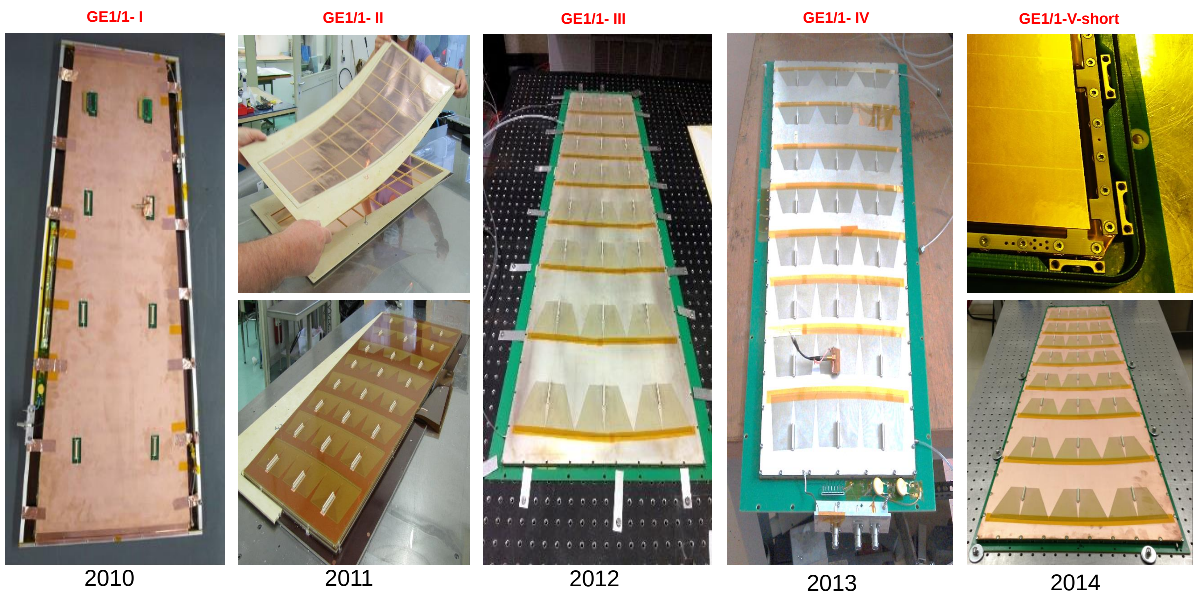

Figure 2.7: Five generations of GE1/1 prototype chambers constructed and tested by the GEM collaboration in 2010-2014.

The first prototype GE1/1-I was the first 1m-class GEM detector ever constructed and operated (put Ref.: 2010 IEEE and RD51-Note-2010-005). Components were glued together and spacer ribs were used to keep the GEM foils apart; it had only 8 readout sectors total. In the GE1/1-II the readout segmentation was increased to 24 sectors and the foil gap configuration was changed from 3/2/2/2 mm to 3/1/2/1 mm to speed up the signal (put also Ref. 2011 IEEE and RD51-Note-2011-013)[7]. The GE1/1-III prototype was the first detector in which foils were stretched purely mechanically against the outer detector frame, but this frame was made from several pieces and was glued to the drift board. This generation was also the first prototype to use a miniaturized ceramic high voltage divider for powering. (put Ref.: 2012 IEEE N14-137) When bolting the readout board onto the outer frame in this design, the O-ring acted as a fulcrum creating a torque on the board as the bolts were tightened. This caused the readout board to deform slightly after assembly, which in turn caused a response non-uniformity across that chamber prototype as the foil gap sizes were not kept uniform enough. In the GE1/1-IV prototype, both readout and drift boards were pre-bent in the opposite way before assembly in an attempt to compensate for the bending that occurs after assembly. They were bolted to the outer frames and sealed with O-rings making the GE1/1-IV the first large-area GEM detector produced without gluing any components. Consequently, it could be assembled in a few hours (put Ref.: MPGD 2013 and 2013 IEEE). While the pre-bending technique works in principle, it is not deemed reliable enough for future mass production purposes and it is a time-consuming production step. Instead, the problem has been rectified in the current GE1/1-V prototype design by tensioning the foils against independent "pull-out" pieces (see Fig. 2.7 top right). The drift and readout boards are now bolted onto the pull-out pieces. The outer frame is made from a single piece and only serves as a wall for the gas volume; it is sealed against readout and drift boards with O-rings. This final prototype design with a few improvements of details is being adopted as the final design of the GE1/1 Triple-GEM chambers, which is described in this report (see section 2.3).

2.2.2 Performance measurements and simulation studies

The performances of the different generations of GE1/1 prototypes were studied in a series of beam tests at CERN in 2010[8], 2011[9], and 2012[10], and at Fermilab in 2013[11]. The beam tests at CERN focused on measuring the performance when the chambers were operated with the Ar/CO_2/CF_4 45:15:40 gas mixture and read out with binary-output VFAT2 front-end chips, whereas in the Fermilab beam test the chambers were operated with Ar/CO_2 70:30 and read out with analog APV front-end chips that produce full pulse height information.

In addition to this multi-year experimental effort, the GEM collaboration has mounted an extensive GEM simulation effort, which is described below in section 2.2.2.4.

2.2.2.1 Measurements of detector gain and response uniformity

Gas gain:

The gas gain was measured for each GE1/1 prototype generation. Typically, for this measurement a high-rate X-ray generator is used to irradiate the GEM chamber. The gas gain can then be calculated from measured hit rates and anode currents. For example, gain measurements performed at CERN for a GE1/1-IV operated at different high voltages applied to the drift electode are shown in Fig. 2.8 for both Ar/CO_2 70:30 and Ar/CO_2/CF_4 45:15:40 counting gases. The typical exponential dependence of the gas gain on HV is evident. The plot also shows the hit rates observed in the GE1/1-IV for a fixed rate of incident X-rays, which feature the beginnings of rate plateaus where the chamber starts operating with full efficiency.

Response uniformity:

An X-ray generator is also employed to study the response uniformity across the detector[12]. Fig. 2.9 shows results from a GE1/1-III scan as an example. The variation of the peak position in the pulse charge distributions is taken as a measure of the response uniformity. From the data

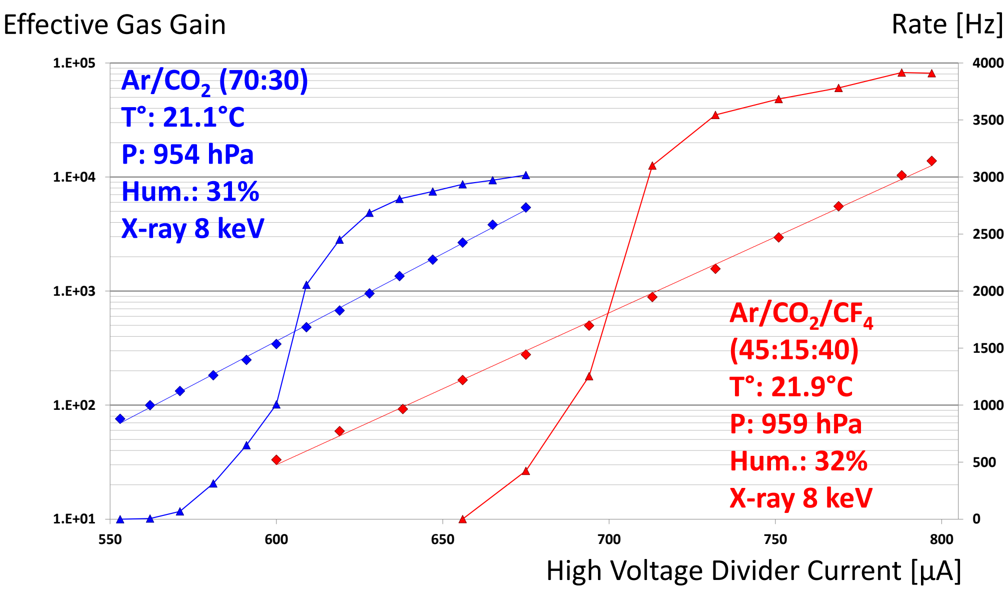

Figure 2.8: Measured gas gains and hit rates as a function of current through the high voltage divider for a GE1/1-IV. Measurements with Ar/CO_2 70:30 (blue) and with Ar/CO_2/CF_4 45:15:40 (red) gas mixtures are displayed. Note that the log scale (left) applies to the gain whereas the rates are plotted on a linear scale (right).

shown in Fig. 2.9 (right) we conclude that the response varies not more than 15% across the detector in this slice. Corresponding measurements for the GE1/1-V are currently in progress.

2.2.2.2 Measurements of detection efficiency, angular resolution, and timing resolution

Efficiency:

Fig. 2.10 shows GE1/1 efficiency measurements for charged particles from two separate beam tests at CERN and Fermilab. A GE1/1-IV prototype reaches a plateau efficiency of 98% for pions when operated with Ar/CO_2/CF_4 45:15:40 and read out with VFAT2 chips. When a GE1/1-III is operated with Ar/CO_2 70:30 and offline cuts are placed on the strip charge measured by the APV to emulate VFAT2 thresholds, the plateau efficiency is 97%. When full APV pulse height information is used, the hit threshold can alternatively be set individually for each strip as a multiple of the pedestal width. For example, with a 5σ pedestal width cut the efficiency is measured slightly higher at 97.8%[11].

Angular resolution:

Results from independent GE1/1 angular resolution measurements obtained in two test beam campaigns are shown in Fig. 2.11. In the 2012 CERN beam test conducted with Ar/CO_2/CF_4 45:15:40 counting gas and binary-output VFAT2 chips, the distribution of track-hit residuals in the azimuthal $\hat{\phi}$ directions shows a width of 268±2 μm when the GE1/1 is excluded from the track fit ("exclusive residual"). This width represents an upper limit on the intrinsic chamber resolution because the exclusive residual width overestimates the intrinsic resolution as the residual width is due to a convolution of intrinsic hit resolution and uncertainty in extrapolated track position. This result is obtained from sector 6 of the chamber at radius r $\approx$ 1.95 m, where the strip pitch in azimuthal direction is 0.88 mm. Consequently, this residual in the $\hat{\phi}$ direction corresponds to an exclusive angular residual of 137±1 μrad. This measured upper limit on the angular resolution in ϕ is close to the expected intrinsic resolution for a binary readout, which is given by: angular strip pitch $/\sqrt{12}$ = 455 μrad $/\sqrt{12}$ = 131 μrad. This performance exceeds

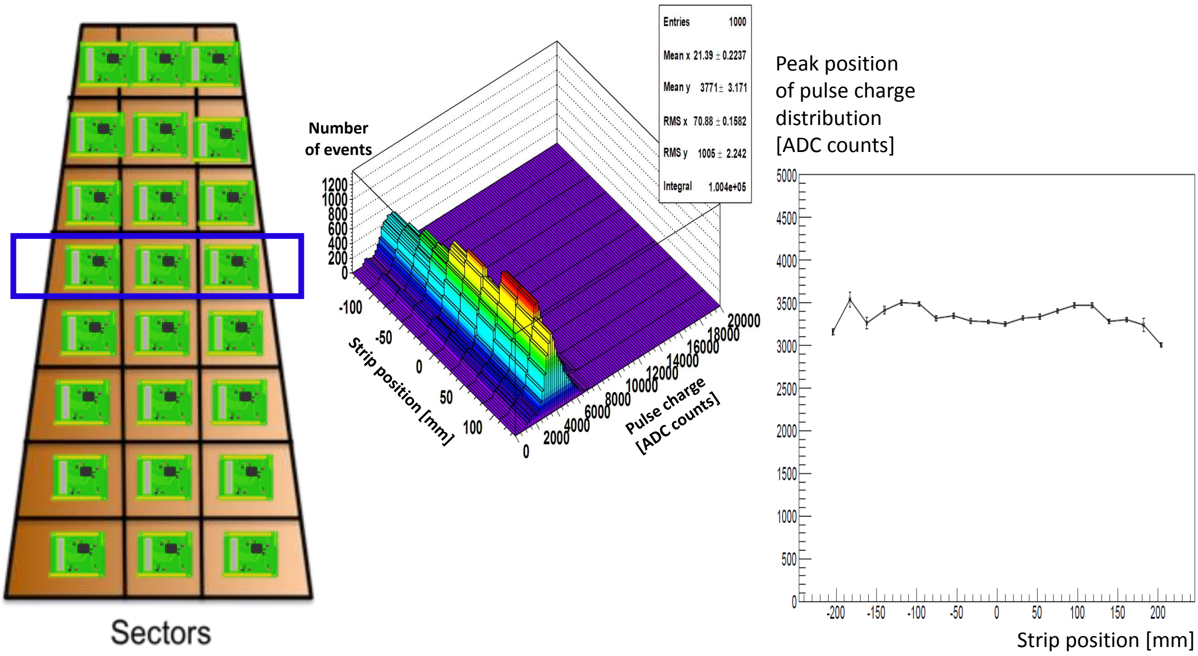

Figure 2.9: Results from a response scan across three sectors (left) of a GE1/1-III with an X-ray generator. The pulse charges measured on several adjacent strips are grouped together and histogrammed (center). The peak position of the pulse charge distributions for the strip groups are then plotted vs. the positions of the strip groups across the chamber (right).

the minimum requirement of 300 μrad with a comfortable safety margin.

For the 2013 Fermilab beam test data obtained with Ar/CO_2 70:30 counting gas and analog-output APV chips, the measured strip charges can be used to determine the hit position in the GE1/1 from the barycenter of the strip charges (centroid). For these data, exclusive residuals and "inclusive" residuals were calculated. For the latter, the GE1/1 hit is included in the track fit. Measurement of both residual types are shown at the center and bottom of Fig. 2.11. The inclusive residual underestimates the intrinsic resolution of the chamber because including the hit of the probed chamber biases the track towards that hit. However, it can be shown put ref.! that the intrinsic chamber resolution can be obtained to good approximation from the geometric mean of the widths of the inclusive and exclusive residuals. At a radius r = 1.95 m (sector 6), we then find an angular resolution

$$\sigma_{resolution} = \sqrt{\sigma_{incl.residual} \times \sigma_{excl.residual}} = 102 \pm 2\ \mu\text{rad}\,, \quad (2.1)$$

which is 22% smaller than the upper limit on the resolution obtained with VFAT2 chips in the same radial position. Corresponding residuals and angular resolutions measured for other sectors using the centroid method are shown in Fig. 2.12. The measured angular resolution varies over a range of 100 - 150 μrad in sectors 2-7. Sector 6 mentioned above happens to have the best resolution in this measurement. The resolution could not be measured for the outer sectors 1 and 8 of the prototype due to geometric constraints in the test beam setup.

The number of strips in a strip cluster is observed to increase with high voltage (Fig. 2.13 left) because the lateral size of the electron avalanche in the Triple-GEM increases as the gain increases. At the start of the efficiency plateau around 3200 V in Ar/CO_2 70:30, two-strip clusters dominate; these also produce the best angular resolutions of $\approx$ 115 μrad (Fig. 2.13 right) when the centroid method is used for calculating the hit position.

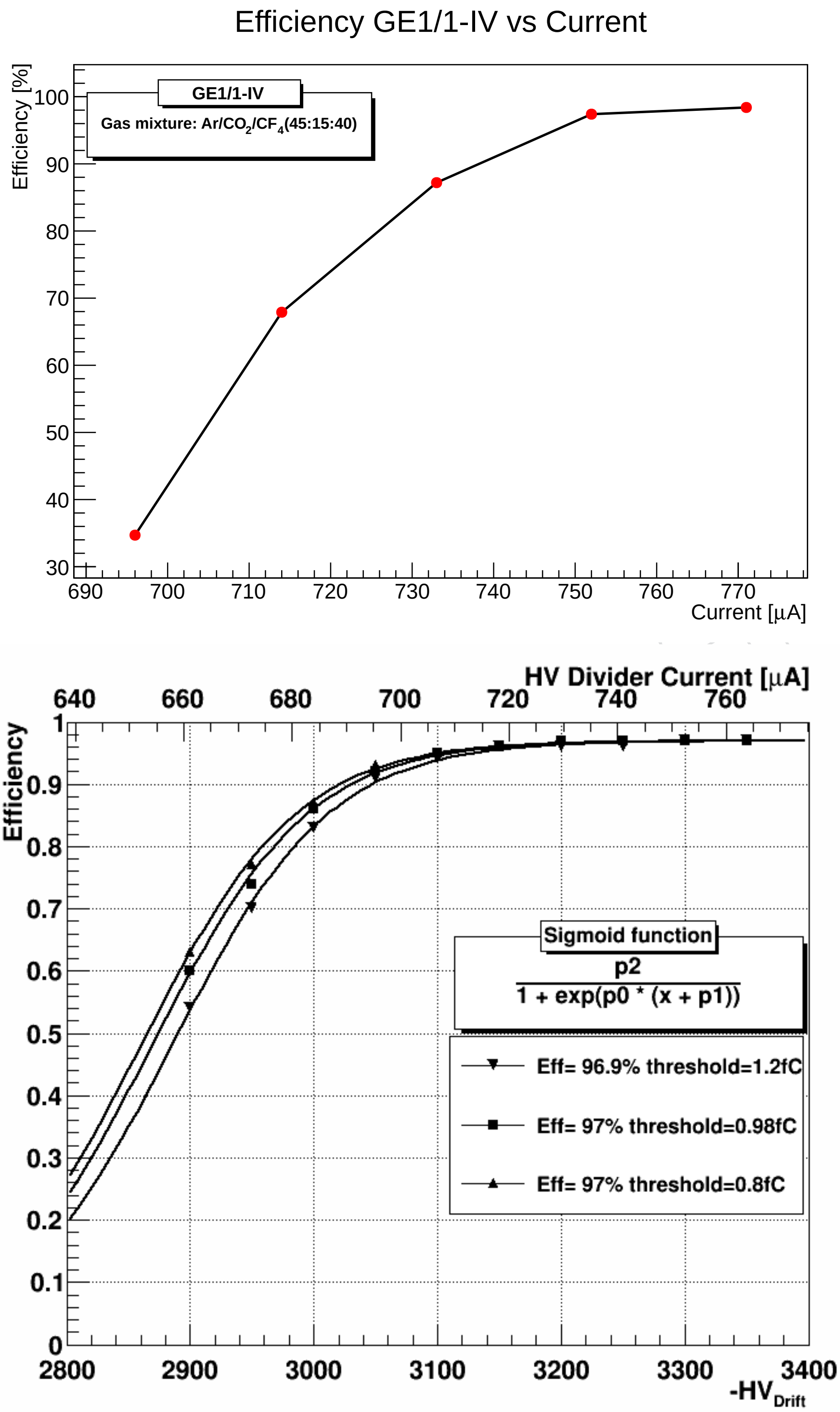

Figure 2.10: Measured detection efficiencies of GE1/1 prototypes for charged particles. *Top:* Eff. vs. current in the HV divider when GE1/1-IV is operated with $Ar/CO_2/CF_4$ 45:15:40 and read out with VFAT2 chips configured with 0.8 - 1.2 fC strip-hit thresholds. *Bottom:* Eff. vs. HV applied to the drift electrode measured in central sector 5 of a GE1/1-III operated with Ar/CO_2 70:30 and read out with APV chips. Three different cuts are applied offline to the strip charges to simulate VFAT2 threshold behavior and the resulting efficiency curves are fitted to sigmoid functions.

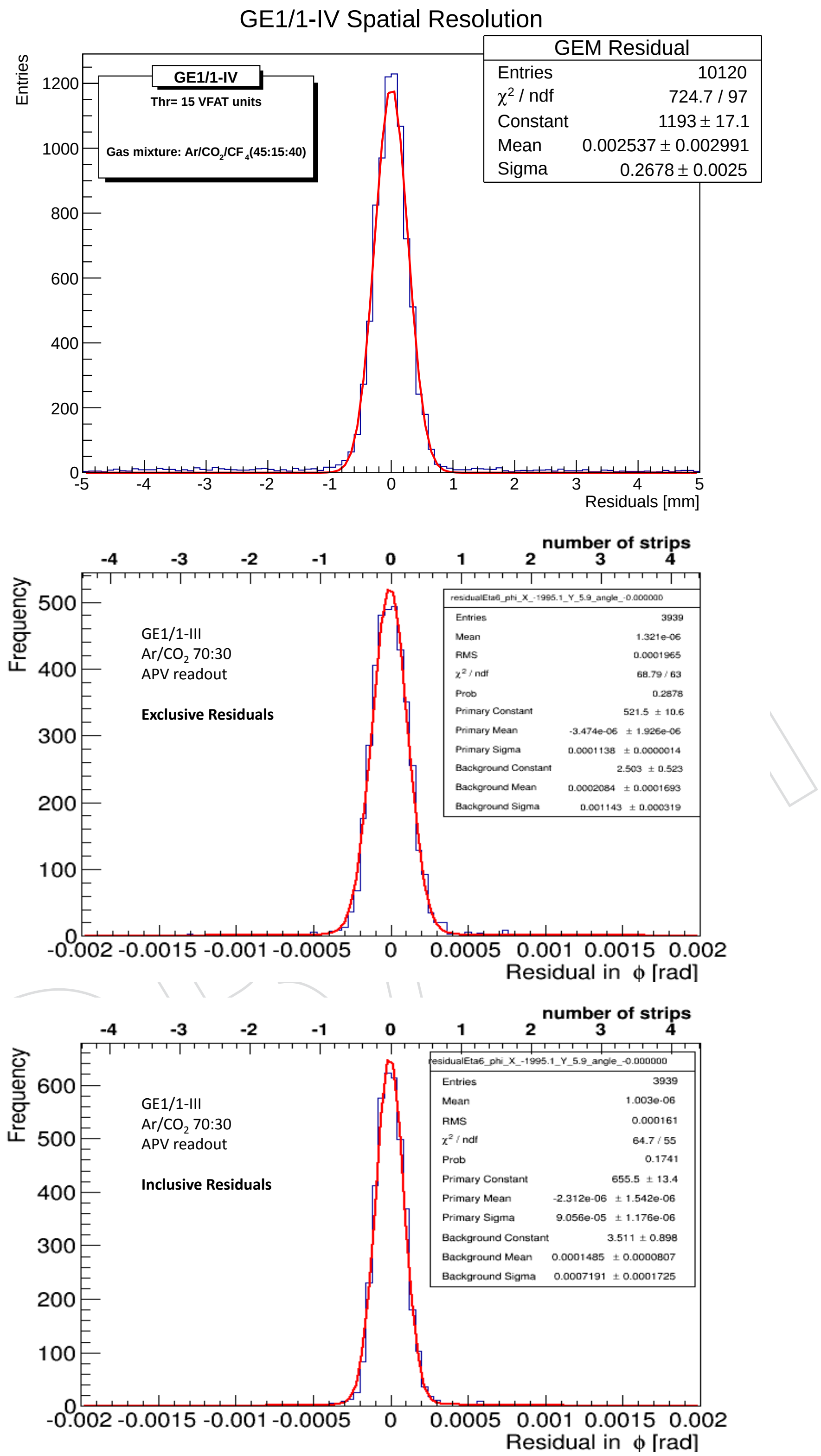

Figure 2.11: Track-hit residuals measured in central sectors of GE1/1 prototypes at r=1.95m. *Top:* Exclusive residuals in azimuthal $\hat{\phi}$-direction measured with a pion beam at CERN when GE1/1-IV is operated with $Ar/CO_2/CF_4$ 45:15:40 and read out with binary-output VFAT2 chips. *Center:* Exclusive angular residuals measured with a mixed pion and kaon beam at Fermilab when a GE1/1-III is operated with Ar/CO_2 70:30 at 3300 V and read out with APV chips. Here the barycenter of the strip cluster charge (centroid) is used to determine the hit position. The residuals are fitted with a double Gaussian function. *Bottom:* Corresponding inclusive angular residuals for same measurement as center plot.

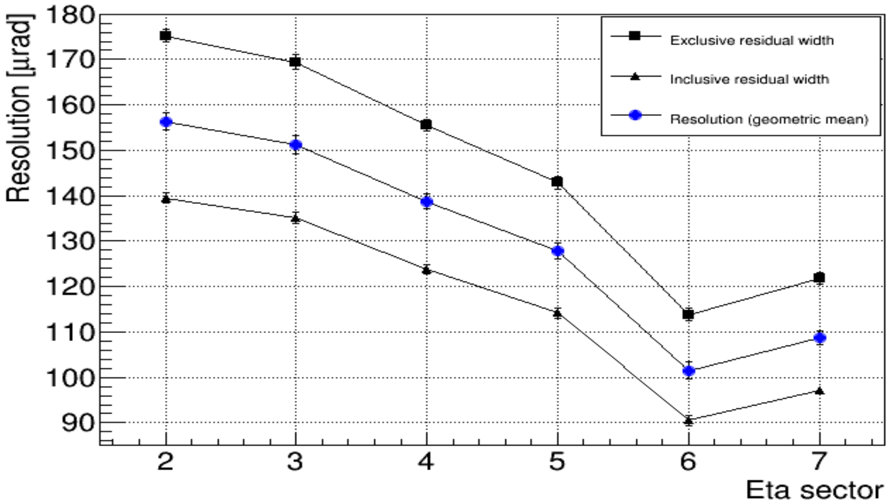

Figure 2.12: Measured residual widths and angular resolutions in six of the eight η-sectors of a GE1/1-III operated with Ar/CO_2 70:30 at 3300V and read out with APV chips. Sector numbers increase with increasing radius and decreasing η.

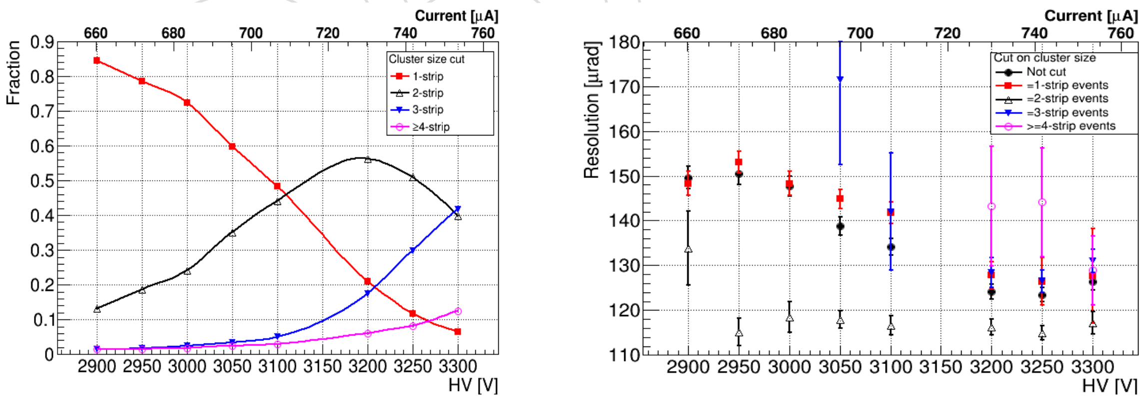

Figure 2.13: *Left:* Relative fractions of strip multiplicities observed for strip clusters in sector 5 of a GE1/1-III operated with Ar/CO_2 70:30 and read out with APV chips as a function of high voltage applied to drift electrode. *Right:* Corresponding measured angular resolutions for different strip multiplicities of strip clusters vs. high voltage.

Timing resolution:

The timing performance measured with a 10 cm × 10 cm Triple-GEM equipped with standard double-mask GEM foils is shown in Fig. 2.14. The timing resolution for Ar/CO_2 70:30 and a 3/2/2/2 mm gap configuration is compared with the timing resolution for $Ar/CO_2/CF_4$ 45:15:40 and a 3/1/2/1 mm gap configuration. With the faster gas and the shorter drift distances, the timing resolution improves by a factor of two from 8 ns to 4 ns.

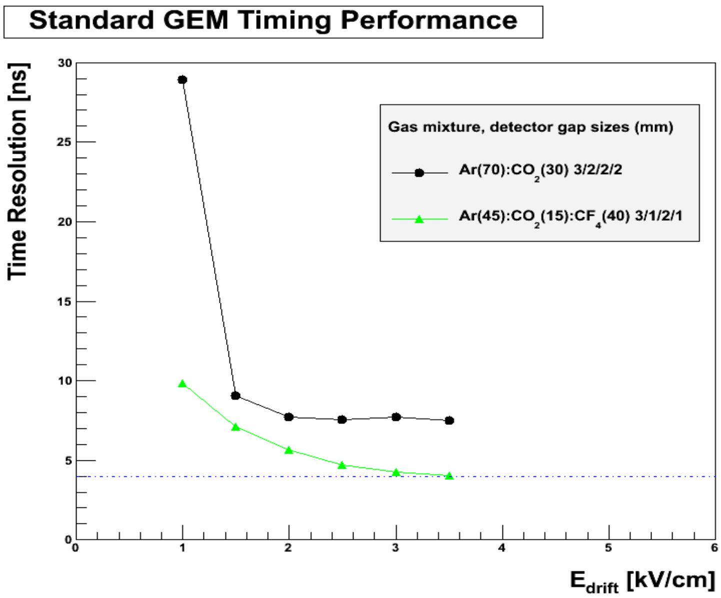

Figure 2.14: Timing resolutions measured with a TDC for a small Triple-GEM detector equipped with GEM foils produced with the standard double-mask technique as a function of drift field for the counting gases under consideration.

The timing performance of an actual GE1/1-III prototype operated with $Ar/CO_2/CF_4$ 45:15:40 and read out with VFAT2 chips in the 2012 test beam at CERN[10] is shown in Fig. 2.15. Dedicated timing hardware selects events within a 2 ns time window from the asynchronous SPS beam. Rather than performing direct TDC measurements, here the relative fraction of GEM hits in adjacent 25 ns time bins is measured (Fig. 2.15 left). For the configuration used, 97% of all hits occur within the correct 25 ns clock cycle.

One can then ask what value of a Gaussian width σ would produce that plot when a close to perfect ($\delta(t)$-like) input time distribution is smeared with that Gaussian and binned in 25 ns bins. We take the width σ of the Gaussian that best reproduces the timing fraction histogram of Fig. 2.15 (left) as our measurement of the GE1/1 timing resolution. The GE1/1 time resolution measured with this method is shown as a function of current in the HV divider in Fig. 2.15 (right). On the efficiency plateau, the GE1/1-III has a timing resolution of 6 ns. For two GE1/1 chambers in one superchamber operated with $Ar/CO_2/CF_4$ 45:15:40, we would expect a timing resolution of 6 ns / $\sqrt{2}$ = 4 ns. Based on the results in Fig. 2.14, we then expect an overall timing resolution of 8 ns for a superchamber operated with Ar/CO_2 70:30.

2.2.2.3 Performance in magnetic field

This sections still needs to be edited - MH

During a dedicated beam test with the CMS M1 superconducting magnet, a GE1/1-II prototype was operated in a strong magnetic field[9, 13]. The CMS M1 superconductive magnet is located

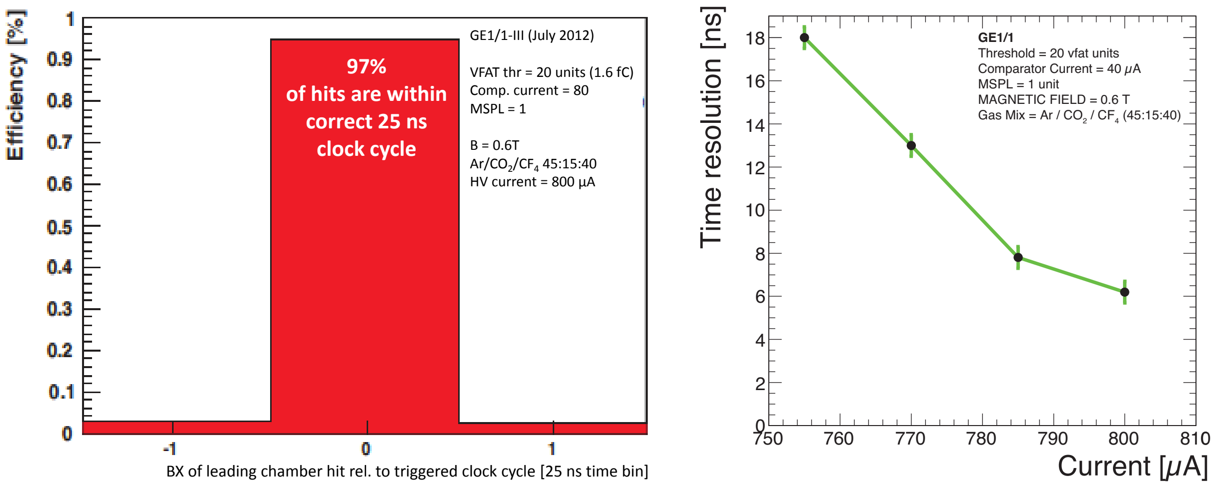

Figure 2.15: Timing measurements for a GE1/1-III prototype with VFAT2 readout in a beam with 25 ns bunch crossing time. *Left:* Fraction of hits measured in bunch crossings relative to the trigger clock cycle. *Right:* Timing resolution vs. current in the high voltage divider derived from plots as shown on the left assuming a Gaussian time resolution.

in the SPS H2 beam line at CERN that provides 150 GeV muon and pion beams. This magnet is a solenoid that can produce a field of up to 3 T. The GE1/1-II was placed in between the two magnet coils to validate the detector performance in an environment similar to the high-η region of the CMS muon endcap.

In Fig. 2.16 the measured mean strip multiplicity of strip clusters and the cluster displacements are shown as a function of magnetic field while Fig. 2.17 gives the measured strip multiplicity distribution for strip clusters in presence of the magnetic field. The cluster size does not appear to be affected by the magnetic field, while the signal induced on the strips is displaced due to the presence of the magnetic field. The measurement of this displacement is in good agreement with simulations performed with GARFIELD**??**. The timing performance was also measured with and without magnetic field as shown in Fig. 2.18. The overall conclusion is that the magnetic field does not influence the performance of the GE1/1 detector in such a way as to invalidate the conclusions from the measurements without field presented above.

2.2.2.4 GEM performance simulations

This sections still needs to be edited - MH

The simulation effort ranges from simple single-GEM simulations to a full simulation including signal generation and electronics. To simulate the detector response, one has to simulate the electric field map, the electron transport in the gas medium, the avalanche production, and signal formation and induction. The simulation flowchart is presented in Fig.2.19.

Before proceeding with the electric field simulation, it is important to define the detector geometry (Fig.2.20).

This part is done using ANSYS [**?**], a simulation package for computational fluid dynamics applications. In this part, first the GEM based detector geometry (Fig.2.28) is defined in the ANSYS code and the potential and voltages are assigned to each part of the device. The field map is then generated in both 2D and 3D formats.

Once the electric field map is produced for a given configuration, the electron transport in the

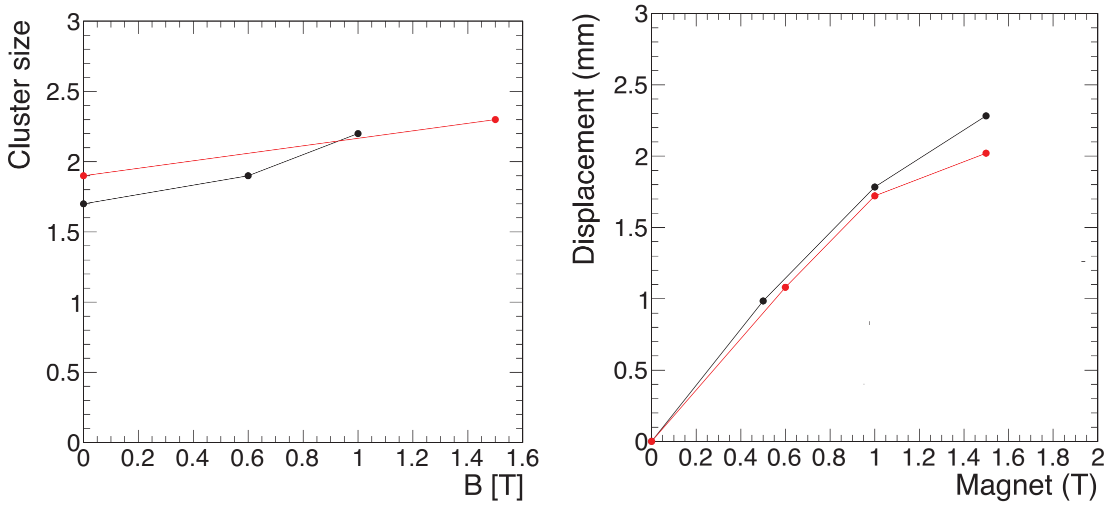

Figure 2.16: GE1/1-II performance inside a strong magnetic field. *Left:* Mean strip multiplicity of strip cluster. *Right:* Strip cluster displacement due to the magnetic field.

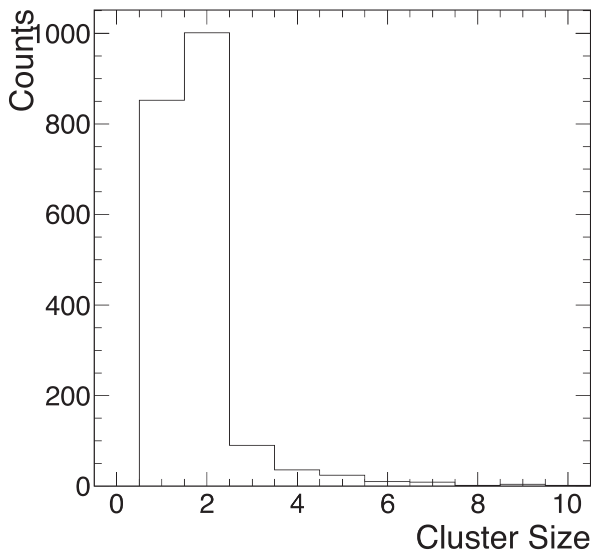

Figure 2.17: Strip multiplicity distribution for strip clusters at B=0.6 T when operating GE1/1-II chamber on the efficiency plateau.

gas medium, the avalanche production and signal formation and induction are simulated and computed. In this part we use the GARFIELD suite. It is a software developed at CERN in 1984 to simulate drift chambers. Since then it has been extended to simulate additional gas mixtures and to include external field maps from different software. It also supports 2D and 3D simulation. Originally GARFIELD was written in FORTRAN and recently a C++ version (GARFIELD++) was released. The group at TAMUQ is suing the C++ version. In Garfield, the field map is loaded as an input file. Then the gas ionization process by primary and secondary electrons is simulated, taking into account their position, direction and energy. Then electron transport properties are computed using MAGBOLTZ software [?] which is now integrated in GARFIELD. It performs a Monte Carlo resolution of the Boltzmann transport equation in various gas mixtures. For ion mobility parameters, existing tabulated data are given as input to the code. Another program HEED [?] (also integrated in GARFIELD) is used to simulate the

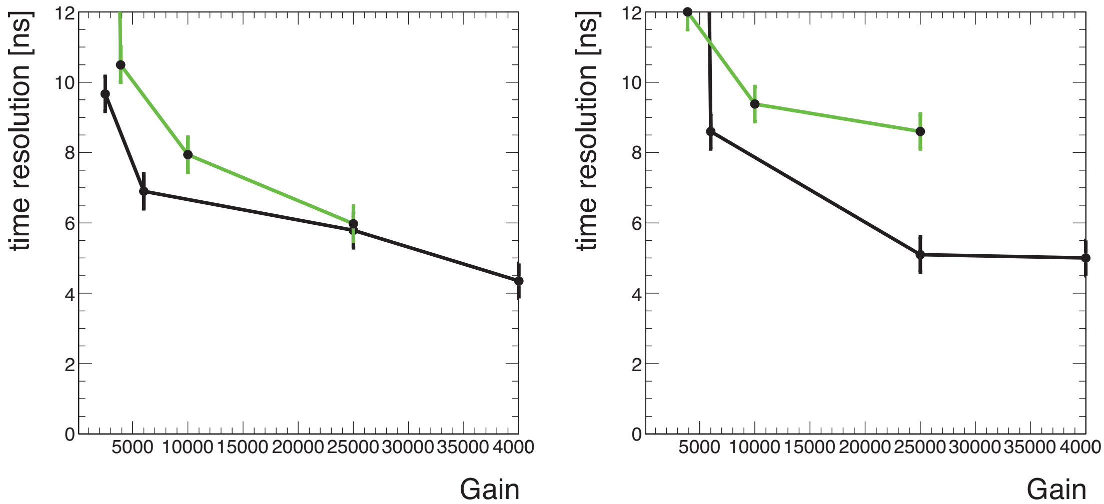

Figure 2.18: Detector time resolution as function of gain without (left) and with (right) magnetic field equal to 1.5 T. The green curves are for the GE1/1-II while the black curves are for a small-size prototype.

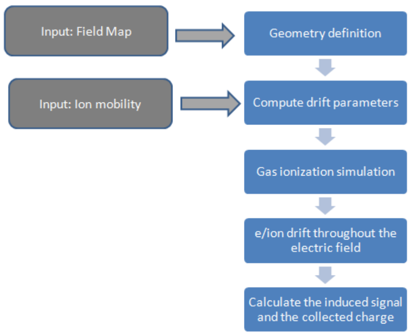

Figure 2.19: Flowchart of the simulation workflow.

ionization of gas molecules by the incident particle. The electric/ion drift under the effect of the electric field is computed as well as the avalanche effect. Finally we compute the induced current in the detector strips as function of time.

Several parameters have been studied with the simulation, among them:

- variation of the detector gain as a function of the applied voltage
- variation of the gain as a function of the gas mixture used. Two gas mixtures are of interest: Ar/CO_2 and $Ar/CO_2/CF_4$. Other gas mixtures have been recently tried in the simulation
- uniformity of the gain across the detector active area (along the detection strips)
- signal formation and timing resolution

Each simulation consisted of 5000 electrons randomly distributed on X and Y directions and fixed at 0.25 mm on the Z-axis as shown in Figure FIXME.

Detector gain

The detector gain was simulated with two different gas mixtures as a function of the HV. The total gain is defined as the total number of electrons produced in the avalanche, whereas the

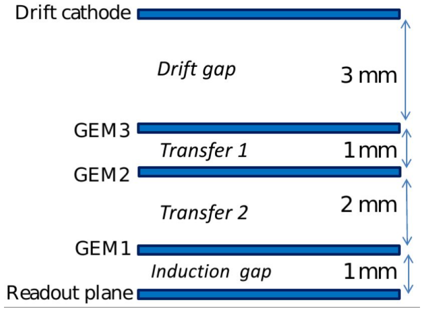

Figure 2.20: Cross section of a 3-GEM based detector.

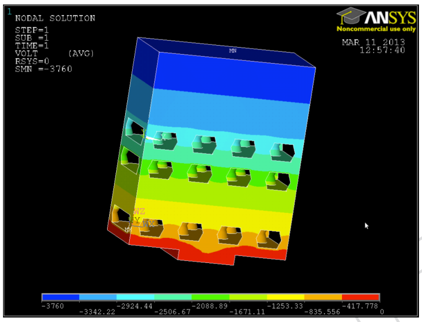

Figure 2.21: Description to be provided

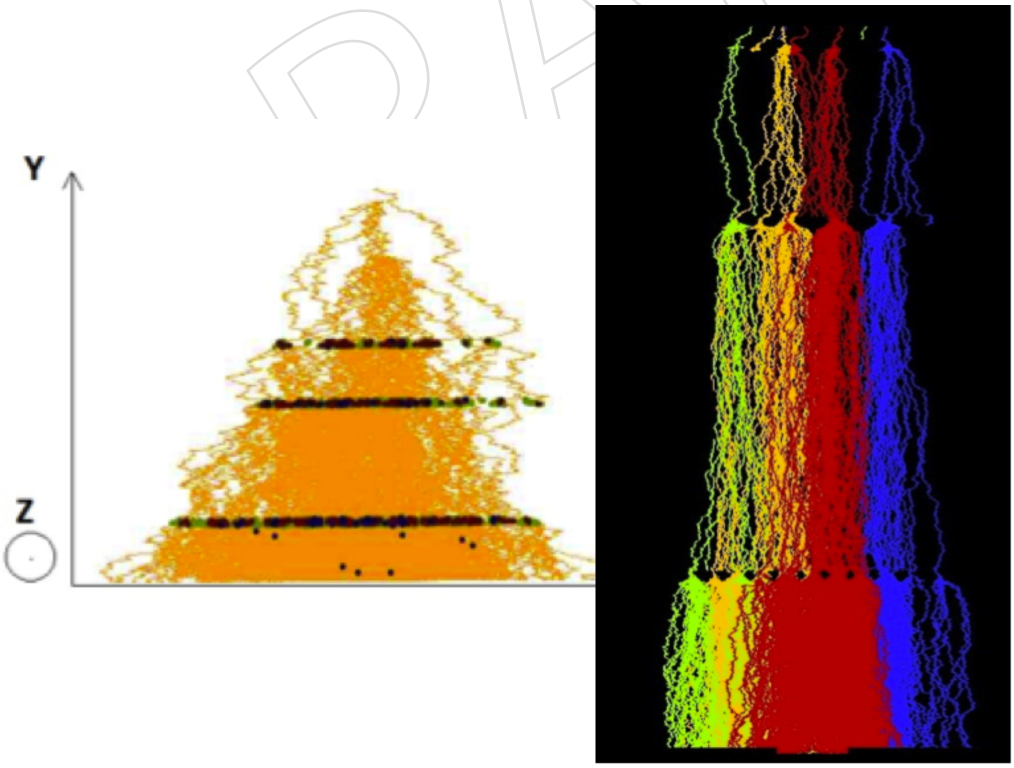

Figure 2.22: Examples of avalanche development in the triple GEM chamber

effective gain is the number of electrons reaching the readout electrodes. Figure 2.23 shows the total and effective gains as a function of the HV for different values of the penning effect when the detector is filled in with Ar/CO_2/CF_4. Figure 2.24 shows the same but with Ar/CO_2. The simulation results were validated by comparing to the experimental measurement taken during previous test beam []. This is not ready, in progress... Figure XXX also shows the effective gain as a function of the HV for different gas proportions. Figure FIXME shows the effective as a function of the HV for different gas mixtures with the same proportions but with different noble gas (He, Ne and Ar). As shown previously in other detectors [], Ne is a promising gas mixtures leading to higher gas gains.

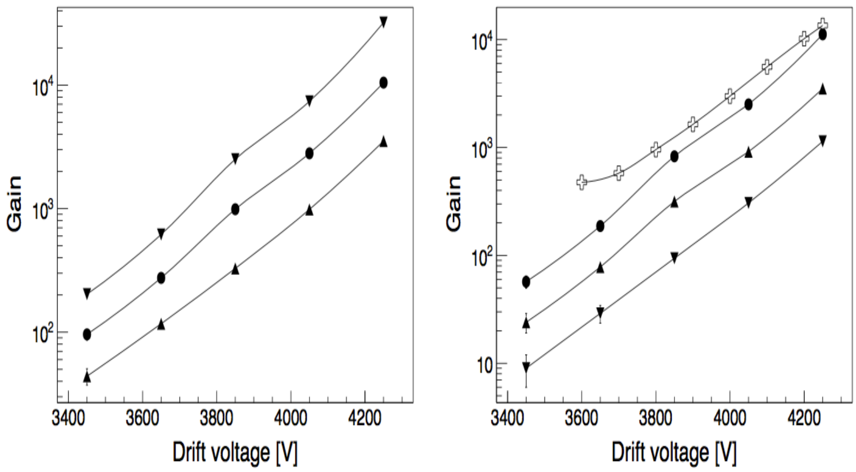

Figure 2.23: Total (left) and effective (right) gain as a function of divider drift voltage for different penning transfer efficiencies (1, 0.7 and 0.4 from top to bottom) in a 45/15/40:Ar/CO_2/CF_4 gas mixture, compared to experimental data (open crosses) taken from [].

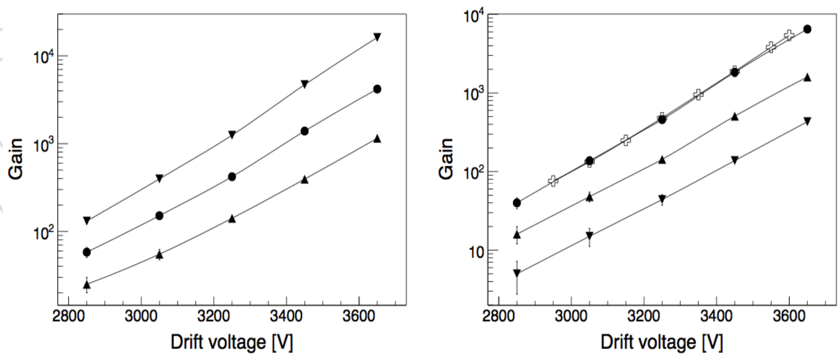

Figure 2.24: Total (left) and effective (right) gain as a function of divider drift voltage for different Penning transfer efficiencies (1, 0.7 and 0.4 from top to bottom) in a 70/30:Ar/CO_2 gas mixture, compared to experimental data (open crosses) taken from [].

Uniformity One important parameter to measure is the uniformity of the gain across the strips. Due to the trapezoidal shape, it is important to check the gain variations along the chamber area. Figure 2.25 shows the effective gain as a function of the readout pitch in Ar/CO2/CF4 with different values of the Penning effect. The readout pitches in $\hat{\phi}$-direction are 0.6, 0.8 1.0 and 1.2 mm, thus covering the complete GEM chamber pitch variation. There is a slight increase of the effective gain with the pitch size, but the variation does not exceed 15%. **Timing resolution**

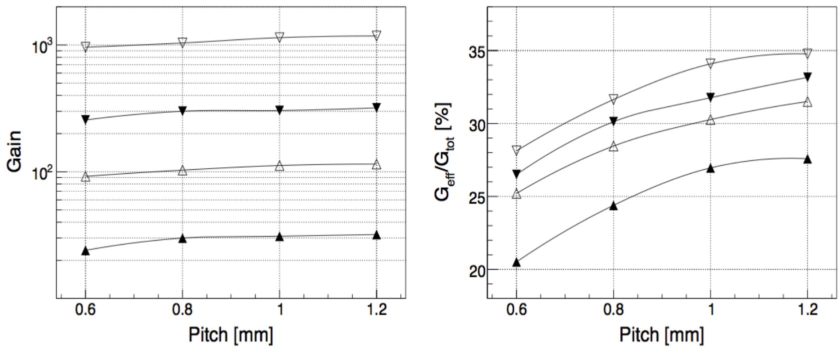

Figure 2.25: Effective gain (left) and ratio of effective to total gain (right) for 3650, 3850, 4050 and 4250 V (from bottom to top) as a function of readout strip pitch for V_d = 4050 V and r_P = 0.4 in 45/15/40:Ar/CO_2/CF_4

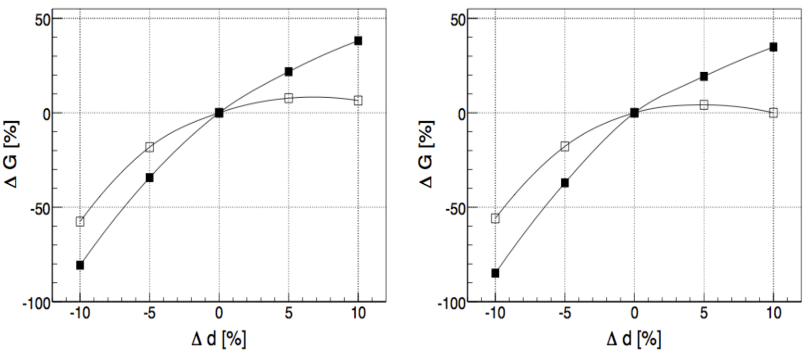

Figure 2.26: Effect on the total (full square) and effective (open square) gain of a variation in the outer (left) and inner (right) hole diameter for V_d = 4050 V and r_P = 0.4 in 45/15/40:Ar/CO−2/CF_4 mixture

In a triple-GEM detector, the signal on the strips is induced by the electrons produced by primary ionization and amplified through the three stages of amplification. Both processes have fluctuations which lead to some large fluctuation in the shape of the induced signal as shown in Figure FIXME . To better understand the signals shown in Figure FIXME, lets remind that in the $Ar/CO_2/CF_4$ (45:15:40) gas mixture, the drift velocity is 10 ns/mm. Therefore we can identify the contribution of the primary ionization to the signal from the different gas gaps of the detector. Between 0 and 10 ns we see the signal induced by the electrons coming from the Inducing gap, between 10 and 30 ns we see the signal given by the electrons coming from the Transfer 2 gap and amplify by the third GEM, between 30 and 40 ns we see the signal given by the electrons coming from the Transfer 1 gap and amplified by the second and third GEM, and finally between 40 and 70 ns we see the signal given by the electrons coming from the Drift gap and fully amplified by the three GEM foils. The front-end electronics foreseen for the triple-GEM is the VFAT3 (see Chapter FIXME). In order to estimate the performance of the triple-GEM detector like time resolution, efficiency, etc., one has to simulate the response of this electronics. The simulation is done by convoluting the induced signal given by Garfield, with the VFAT3 transfer function given by: $F(t) = (\frac{t}{t})^n exp(\frac{-nt}{\tau})$, where t is the time, the peaking time(25 ns, 50 ns, 75 ns, 100 ns, 200 ns or 400 ns) and n the filter order (n = 3 for VFAT3). In the VFAT3 electronics, the output signal of the shaper will be sent to a Constant Fraction Discriminator (CFD) which allows to identify the arrival time of the signal. The CFD method consists of building a bipolar signal from the output of the shaper. This bipolar signal has the property to have his zero crossing point occurring at the same time for every amplitude. We have applied the CFD method for 5 differents peaking time (25 ns, 50 ns, 75 ns, 100 ns and 200 ns). For each peaking time, we used 500 events simulated with Garfield. As we can see on Figure FIXME showing the time resolution as function of the VFAT3 peaking time, the time resolution is better than 5 ns for a peaking time longer than 50 ns. This result confirms the very good time resolution of the CMS triple-GEM detector measured during the test beam 305 with $Ar/CO_2/CF_4$ (45:15:40) gas mixture [].

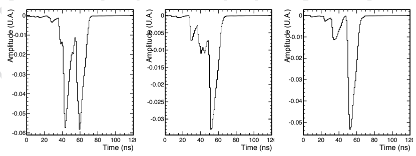

Figure 2.27: Description to be provided

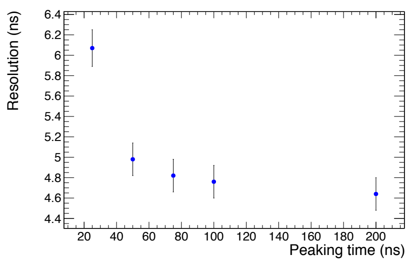

Figure 2.28: Description to be provided

2.2.3 Considerations for environmentally-friendly counting gas mixtures

Text for this section still needs to be provided by LB - MH

2.3 Technical Design of GE1/1 Chambers for CMS

2.3.1 GEM foil design and production technology

The production of GEM foils is based on photolithographic techniques commonly used by the printed circuit industry. The copper-clad kapton substrate gets laminated on both sides with solid photoresist of 15 μm thickness that the GEM hole pattern is transferred onto by UV exposure through flexible masks. In order to get good homogeneity of the hole geometry across the foil, it is very important to keep the alignment error between the masks on the two GEM foil sides within 10 μm. However, since both the raw material and the two masks are made from flexible material, the manual alignment procedure becomes extremely cumbersome when the linear dimensions of the GEM exceed 40 cm.

A natural way of overcoming this problem is the use of single-mask photolithography. In this case the GEM pattern is transferred only to one side of the raw material, thus removing any need for alignment. The exposed photoresist is developed and the hole pattern is used as a mask to chemically etch holes in the top copper electrode of the GEM foil. After stripping the photoresist, the holes in the top copper electrode are in turn used as a mask to etch the polyimide.

Single-mask photolithography (Fig. 2.29) has been proven to be a valid manufacturing technique for making GEMs. This technology was used to build a prototype detector for a possible upgrade of the TOTEM T1 detector. More recently, the production process has been refined even more, giving great control over the dimensions of the GEM holes and the size of the hole rims during the production process. Effects of the hole shape are also being explored in simulation studies (see below). Production issues have been studied and single-mask GEMs are compatible with industrial production using roll-to-roll equipment, which is a very important aspect of this new technique. Consequently, a price reduction for GEM foils is expected from large-scale industrial production that is now possible.

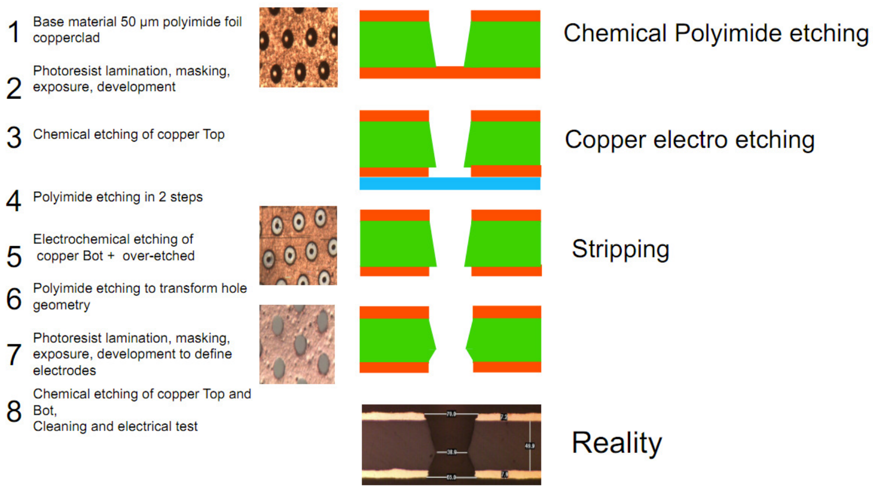

Figure 2.29: Overview of single-mask etching process for GEM foils.

2.3.2 Validation of chamber materials

This sections still needs to be edited - MH

The known challenges for the GEM detector consist of mechanisms of aging, due to the presence of highly radiogenic environments, as well as interactions with gas mixture and system fluids, and the need to obtain standard procedures for proper quality control. After identifying the parameters of interest for the system and the characteristics of the materials making up the detector, we report on preliminary results on studies of diffusion of water in the detector materials, and of tensile properties of mechanically tensioned chamber elements. The materials studied in this section were kapton and GEM foils. Studies are ongoing on gas mixture, glue, cured resins, o-rings, gas inlet/outlet, screws, washers.

Analyses have been performed on unused samples of kapton and GEM foils in order to have data for later comparison to samples to be irradiated at the GIF (Gamma Irradiation Facility). The samples reference state was obtained by means of FTIR (Fourier Transform Infra Red) analysis, optical microscopy and SEM-EDS (Scanning Electron Microscopy - Energy Dispersive Spectrometry) characterization (figure 2.30).

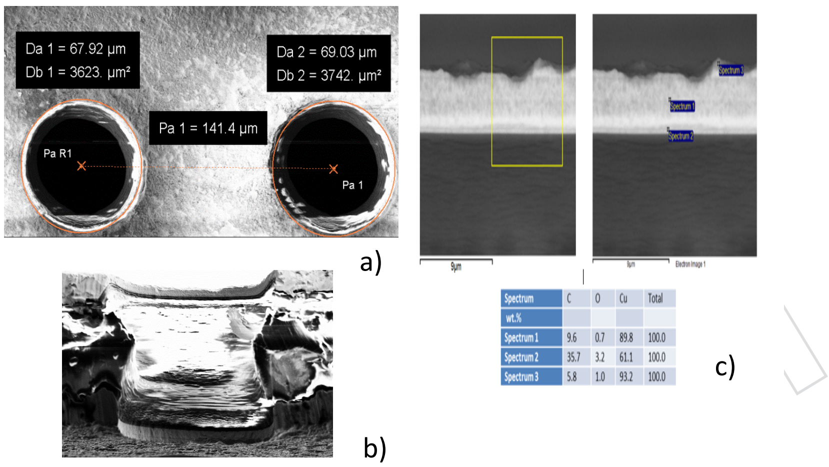

Spectrum	C	O	Cu	Total
wt.%				
Spectrum 1	9.6	0.7	89.8	100.0
Spectrum 2	35.7	3.2	61.1	100.0
Spectrum 3	5.8	1.0	93.2	100.0

Figure 2.30: Microscopy images (top and bottom left) and spectra (bottom right) from SEM-EDS on a section (top right).

GEM foils interact with humidity both before assembly because of cleaning procedures where water is used, and via atmospheric air intake by means of leaks in gas mixture piping. It is very important to characterize the GEM foil behaviour as a function of humidity in order to determine the amount of water contained in the chambers during the activity of detector. Water content is expected to affect both electrical and mechanical GEM foil properties. Diffusion of water in the GEM foil as a fucntion of time was parametrized according to formula

$$\frac{M(t)}{M(\infty)} = 1 - \frac{8}{\pi^2} e^{-\frac{D\pi^2 t}{4\ell^2}} \tag{2.2}$$

where $M(t)$ is the mass of water adsorbed on kapton surface and diffusing at time t, $M(\infty)$ is the mass of water at equilibrium (saturation), D is the diffusion coefficient and ℓ is the half-thickness of polyimide layer. Two GEM samples with dimensions 10 mm by 15 mm, approximate weight 1080 mg, were pre-conditioned in oven at 110^{o}C for 36 hours. Samples were located in a drier vessel (figure2.31) with controlled humidity obtained using K-carbonate saturated solution (45% RH) along with a standard hygrometer to monitor internal conditions. Data have been collected in continuum. The test has operated at controlled environment typical of GEM operation, i.e. $T = (20 - 22)^o$C and RH=(45-50)%. The constant of diffusion of water in the GEM foils D_{GEM} was determined by best fit of Eq.2.2 to data. Preliminary results yield $D_{GEM} = (3.3 \pm 0.1)\,10^{-10}$cm^{2}s$-1$, corresponding to an 8.5 hours saturation time.

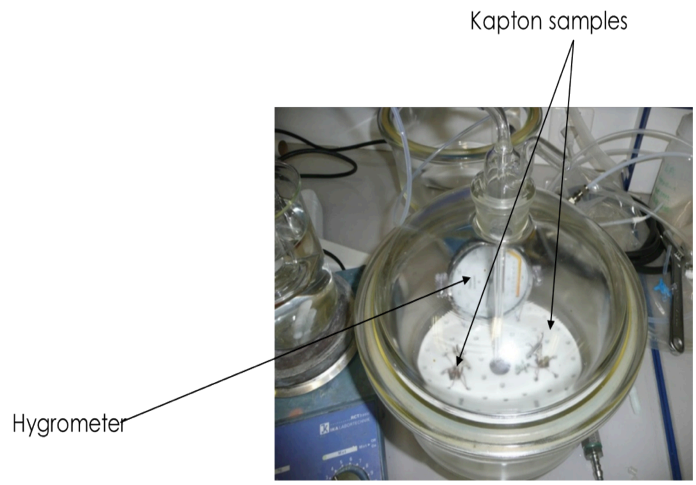

Figure 2.31: Setup for measurement of diffusion coefficient for the kapton-water and GEM-water systems.

The mechanical response of materials was analysed by uniaxial tensile tests [**? ? ?**] for samples of kapton and GEM foils, in both dry and wet conditions. Four samples of GEM foils [10 mm by 110 mm by 60 (50 kapton + 5 Cu + 5 Cu) μm] and four samples of kapton (10 mm by 100 mm by 50 μm) have been dried at 100^{o}C for 36 hours and tested using standard industrial procedures [**? ?**]. For the test in humidity, the samples were humidified at 99.5% RH for 7 days prior to measurement. Figure 2.32 shows preliminary results of the tensile tests. As expected, the GEM foil shows a slight increase of Young's modulus compared to the kapton foil, due to the presence of Cu coating. However, the holes for the electronic multiplication are harmful to the resistance of the structure, behaving as defects and amplifying local stress. Humidity has a larger effect on kapton than on GEM foils. The tensile properties of GEM foils do depend on the extrusion direction. The characterization of mechanical properties of GEM foils before and after irradiation will provide specification on correct standard assembly procedure of GEM chambers, and on their long-term mechanical stability.

In conclusion, a detailed and complete campaign of materials characterization was performed to determine the GEM mechanical assembly parameters, and to guarantee long-term mechanical stability over long term periods. The diffusion coefficient for the kapton-water and GEM-water system was measured, as well as the Young modules for humid/dry kapton/GEM foils. The GEM foil mechanical properties are marginally modified by adsorption of water. Tensile properties depend on the kapton lamination direction.

2.3.3 Mechanical Design

2.3.3.1 Foil stretching

This sections still needs to be edited - MH *Start with description of GEM stack with inner frames and how they are stretched against the brass pull-outs.*

Tolerances inherent in the S2 method to stretch GEM foils and their relative positioning have an impact on the uniformity of gain nd time response. Previous studies on a small area GEM foils (by LHCb experiment) [**?**] have set mechanical precision in gap dimension and uniformity at $\pm$10% ($\pm$100μm for 1 mm-gap), corresponding to a 6% gain variation. In case of $Ar/CO_2/CF_4$

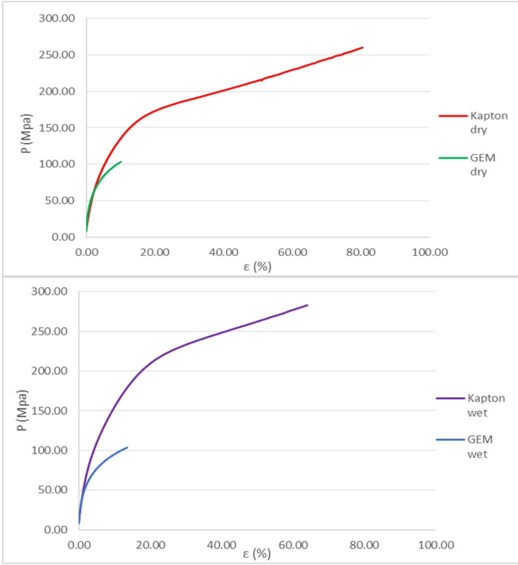

Figure 2.32: Kapton and GEM mechanical properties during tensile stress test.

gas mixture there is a small dependance of drift velocity on the electric field which translate into a small dependence of the timing performance on both mechanical precision and tension stability.

Thus it is crucial to ensure the assembly precision, to determine reliable QC procedures for mechanical tension, and to study the long term stability of the mechanical foil tension. The assembly precision will be provided via Moirè interferometry. Interference patterns assure flatness and uniformity in the plane orthogonal to the foil up to better than 100μm. Long-term stability will be guaranteed by optical strain gauges. The technique has been applied to several detectors in HEP for strain and deformations, temperature and humidity measurements, with a great deal of experience in the Collaboration [**?** **?** **?**].

2.3.3.2 Gas volume enclosure

2.3.3.2.1 Outer frames

2.3.3.2.2 Gas distribution within chamber **[LB]** *Will contain the simulation from Stefano C. about the gas flow through the GE1/1 chamber done with ANSYS. Also Luigi's experimental results on how gas passes through GEM foils. The point is to demonstrate that a simple design with one inlet and one outlet at the opposite corner is good enough to ensure good gas exchange within the chamber. [MH]*

2.3.4 HV distribution to GEM foils

PCB description with GERBER drawings.

Will describe here also the spring-loaded connectors that go through the inner frames to make contact. It appears to be working well, but we should add some info on validation of this system. [MH]

2.3.5 Readout board design

Shouldn't this also be moved to 5.1? [MH]: This sub-section will contain a detailed schema of the GE1/1 chamber assembly procedure, results from Moire measurements and possibly also FBG test done on a S2 prototype. It should also contain results on a long term stability test on a S2 GEM foil stretched.

Resistor	Value
R2, R5, R9, R13	1 MΩ
R1, R3, R6, R10	10 MΩ
R4, R7, R11	580 kΩ
R8	5,6 MΩ
R12	2,2 MΩ

Table 2.1: Values of the resistors for the HV divider

2.3.5.1 Readout strips

A view of the pcb board; maybe design and various photos from the prototypes. [MH]

2.3.5.2 Connections to front-end electronics and GEM Electronics Board

Views of the Panasonic connector including a clear mapping of each strip to the Panasonic pins. [MH]

2.3.5.3 HV Power Supply

This sections still needs to be edited - MH

Needs two separate main subsections: Baseline design with simple HV divider and advanced design with individual powering of each electrode. [MH]

To power all the elements of the detector we initially used a HV resistor divider shown on fig. 2.33. Based on the total current trough the divider chain we have a voltage drop on every resistor which gives the potential needed to power the elements of the detector. The fields inside the detector based on the HV divider shown in figure 2.33 can be calculated based on the following:

For the drift Field E_D [kV/cm]

$$E_D = \frac{I_{div} R_2}{x1} \tag{2.3}$$

where I_{div} is the divider current, $x1$ is the distance between the drift electrode and the top of GEM1 as it is shown in table **??**. This filed plays important role for the drift of primary electrons toward the first GEM and eliminate the ions produced during the ionization of the gas.

For the transfer fileds E_T [kV/cm]

$$E_{T1} = \frac{I_{div} R_4}{x2}; \qquad E_{T2} = \frac{I_{div} R_9}{x3} \tag{2.4}$$

where the $x2$ is the distance between the bottom of GEM1 and the top of GEM2 and $x3$ is the gap between the bottom of GEM2 and the top of GEM3.(table **??**)

For the induction field E_I [kV/cm]

$$E_I = \frac{I_{div} R_{13}}{x4} \tag{2.5}$$

where $x4$ is the induction gap distance. All resistors values are shown in table 2.1. To reduce the possible current provoked due to a discharges there are protection resistors connected to the drift and top of the GEM foils. They are R1, R3, R6 and R10.

Fig. 2.34 show the physical connection between the HV divider 2.33 and the detector electrodes.

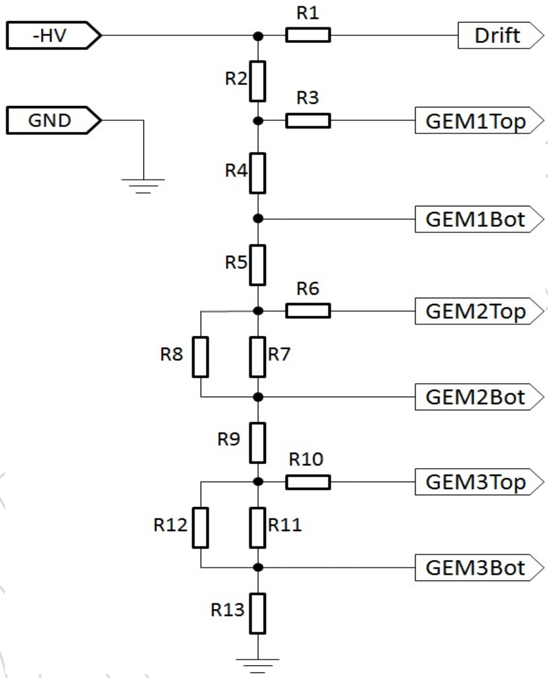

Figure 2.33: HV divider schema used for the Timing GEM

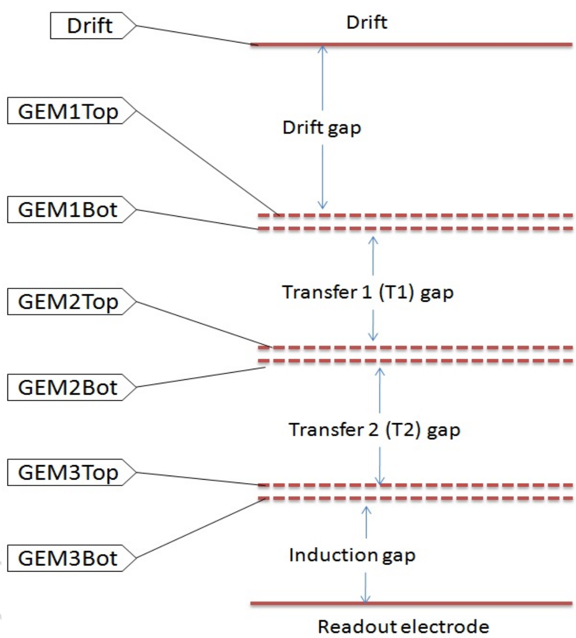

Figure 2.34: Triple GEM detector, HV divider connections

All other resistors like (R4, R7——R8 and R11——R12) provide the potentials needed for the GEM foils.

The used HV power supplies for this project are made on the principle of the DC to DC conversion by using an internal push-pull oscillator. In this case the output DC voltage always contains an AC component with non negligible amplitude which disturbs the output signal from the GEM detector. For this reason a small HV RC filter was made as it is shown in fig. 2.39. It represents a symmetric RC LPF (Low Pass Filter) housed in an aluminum box. The electric diagram of the filter is shown in fig. 2.35. All the resistors are with 100 kΩ value and the capacitors are 2.2 nF at 6000V with ceramic dielectric.

Figure 2.35: Electric diagram of the HV filter

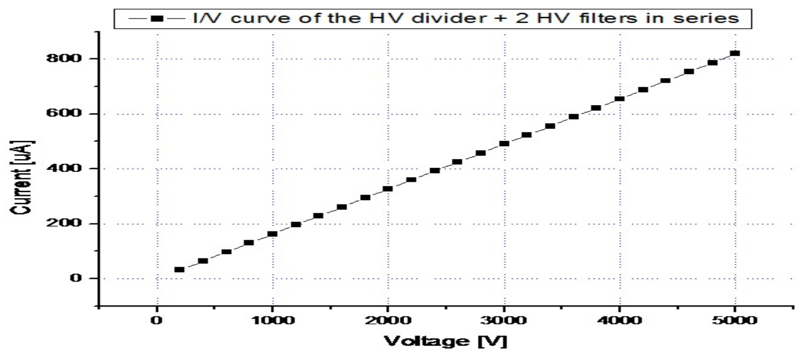

Figure 2.36: Measured I/V response of the HV divider connected with 2 HV filters in series

Usually during measurements we sue two filters connected in series to the HV divider. Buy this way we have increased the total resistivity of the circuit with 600 kΩ which needs to be put in to account when we are applying the HV supply. Fig. 2.36 show the I/V response of the divider plus two HV filters. It represent an calibration curve showing the expected detector HV current consumption.

Having this filter on every HV line is limit dramatically the noise and improves the stability of the output signal. The amplitude and phase response versus frequency is shown in fig. 2.37. The filter start attenuating signals with frequency higher then 1 kHz as it is shown in the figure. Experimentally we found that it helps a lot when we use it with different commercial HV supplies as well as when we use it with the multichannel divider emulation supply.

During the test program it was necessary to change very frequently the values for all the fields and GEM voltages. Using a fixed resistor divider this can be a very difficult task. For this reason we used special multichannel power supply made for the LHCb GEM detectors which has seven channels as output and works with the same behavior as the resistor divider. A scheme of the HV connection of this power supply is given in fig. 2.38. It is necessary to have a 10 MΩ protection resistor between the power supply channel and the detector HV terminal (R1, R2, R3, R4, R5, R6, R7). It is to reduce the current which can be provoked due to discharges. This power supply is controlled trough a LabView software where the values for the voltages and the fields are set.

When is used the multichannel power supply in order to make the powering of the detector more understandable, all the values of the potentials across the detector electrodes are normalized to the corresponding current trough the HV divider. Another way to present the operational parameters of the detector is to give them as a function of the detector gain instead of the HV divider current.

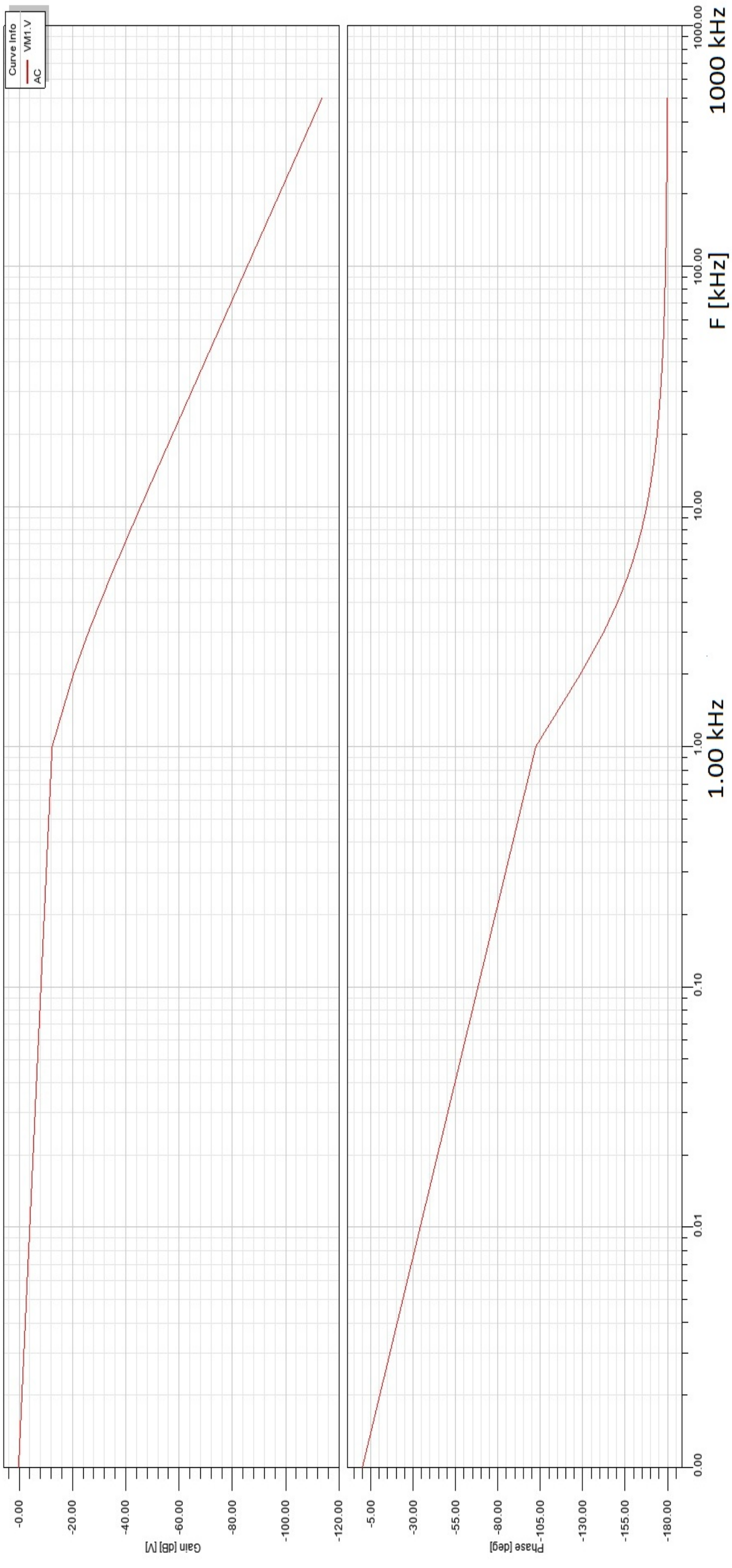

Figure 2.37: Amplitude and phase response as function of frequency.

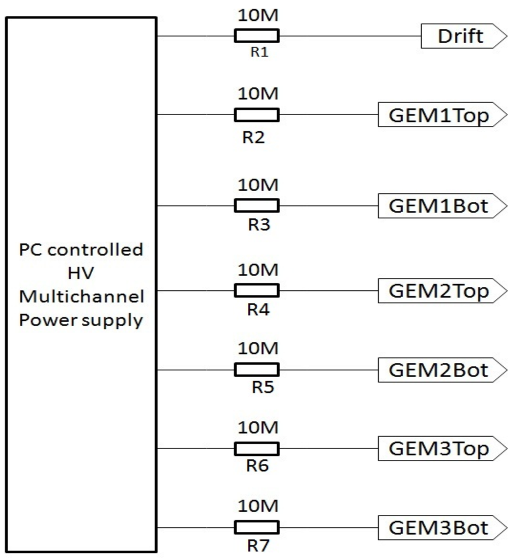

Figure 2.38: Multichannel HV divider emulation power supply schema

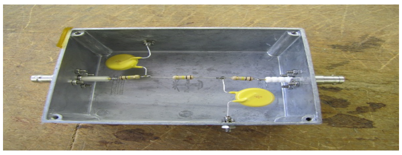

Figure 2.39: HV RC filter used to reduce the AC noise from the HV power supply

Chapter 3

Electronics

Editors: P. Aspell, G. De Lentdecker

3.1 Electronics system overview

Each GEM detector is subdivided in both phi and eta creating sectors which are then further subdivided into 128 strips. The strips (sometimes referred to as pads) are the electrodes to which charge is induced by the passage of an ionizing particle through the detector. This in turn creates the detector signal. This chapter focuses on the hardware used for the treatment and readout of the detector signal from this starting point through the data acquisition system (DAQ) to the interface with CMS.

A block diagram of the main system components in the signal/control path is shown in figure 3.1.

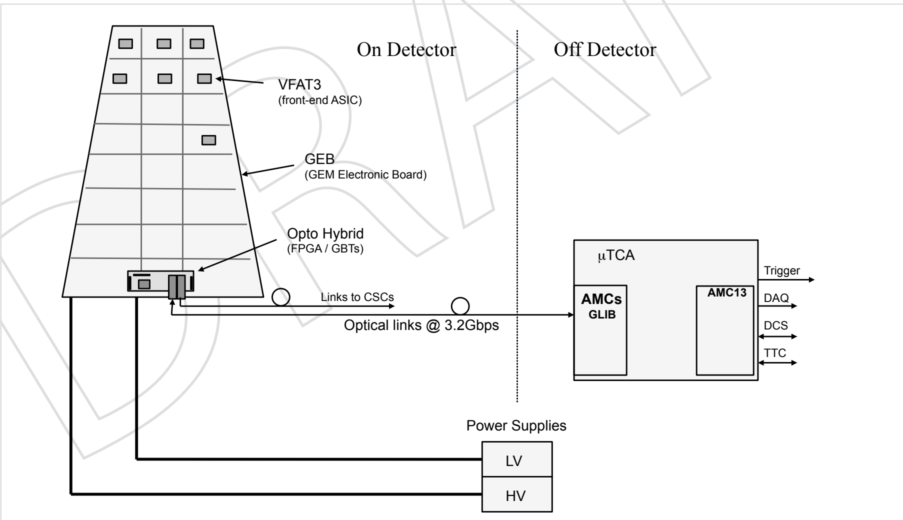

Figure 3.1: The GEM Electronics Readout System

The block diagram illustrates the main system components for the readout of a single GEM chamber and is divided into 2 main regions, namely On-Detector and Off-Detector. Visible in the On-Detector part is the division of the GEM chamber into 24 sectors. The 128 strips from each sector are connected to the inputs of the front-end ASIC (VFAT3) via a connector on a board known as the GEM readout board. VFAT itself is mounted on a hybrid which plugs into the GEM Readout Board connector. The control, readout and power to/from the VFAT hybrid is delivered via electrical signals (E-links) running through a large flat pcb known as the GEM Electronic Board (GEB). An Opto hybrid board also plugs into the GEB which contains the

GBT chip set, an FPGA as well as optical receivers and transmitters to provide the link to the Off-Detector region.

There are two optical paths to the Optohybrid. The first is bidirectional and runs between the mico-TCA crates located in the counting room and the opto-hybrid. This path is used for sending set-up and control signals to the front-end chips. The return path is used for VFAT3 tracking data packets and return slow control data. The second path is uni directional and takes VFAT3 fixed latency trigger data from the GEM system to the CSC system.

The two data paths are illustrated in figure 3.2.

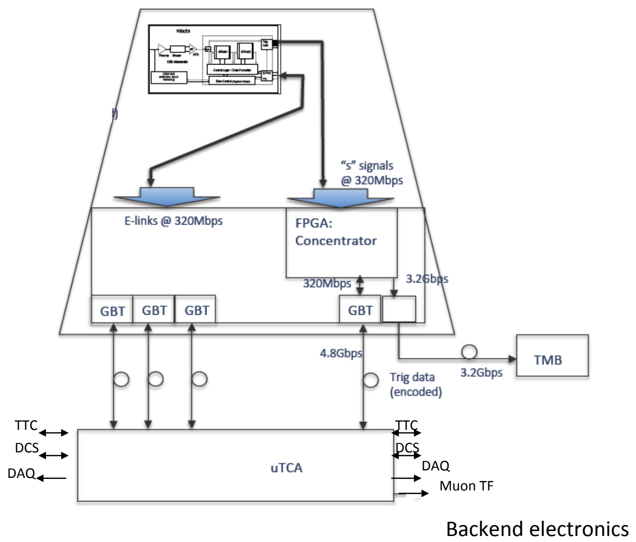

Figure 3.2: Block diagram of the system showing the tracking and trigger paths

3.2 The VFAT3 front-end ASIC

The GEM detectors will be used to provide information relevant to triggering and tracking. The VFAT2 chip was used within the TOTEM experiment for the readout on GEM detectors. The requirements within TOTEM also necessitated tracking and triggering functionalities within the front-end chip. The VFAT2 architecture consisted of 128 channels continuously sampling the GEM strips. It's outputs provided "fast OR" fixed latency trigger information grouping together 16 channels at a time and also full granularity tracking information after the receipt of a level 1 trigger. The requirements of GE11 are similar however there are some important differences that necessitate a new ASIC design. The most fundamental changes are the following :

Charge readout : The signal charge delivered from a GEM detector on the passage of an ionising particle has a duration of many tens of ns depending on the exact gas mixture used. VFAT2 has a fixed shaping time of 25 ns which is much shorter than the duration of the signal. This results in a ballistic deficit. VFAT3 is being designed with a programmable shaping time to be able to integrate all the signal charge. The result will be an increased signal to noise ratio compared to VFAT2.

Timing resolution : The timing resolution is dominated by the properties of the GEM detector. Since this is a very important parameter for optimal trigger performance; the electronics must process the charge delivered without degrading the intrinsic detector timing resolution. VFAT2 achieves this by acting on the rising edge of the GEM charge signal with a short (25 ns) shaping time. VFAT3 will have the option to operate in this mode or extend the shaping to integrate all of the charge and hence boosting the signal to noise ratio. In this later case the timing resolution would normally be degraded due to time walk of a comparator. VFAT3 is being designed to compensate for this effect to maintain the timing resolution to the level given by the detector itself.

Trigger granularity : VFAT2 had a trigger granularity of 16 channels. The specification for GE11 is a trigger granularity of 2 channels. VFAT3 will hence be designed for this increased granularity specification.

Level 1 Latency : The level 1 trigger latency within CMS will be increased. VFAT2 was designed for a LV1A latency of 3.2 μs (with a maximum programmable latency upto 6.4 μs. VFAT3 will increase the latency capability to beyond 20 μs. This complies with the requirements from the CMS trigger upgrades.

Level 1 trigger rate : The trigger rate within CMS will be increased. The requirement being asked is possible LV1A rates upto 1 MHz. This is an order of magnitude greater than the present trigger rates. VFAT2 can cope with LV1A rates upto 200 kHz. The important parameter here is the length of time needed for the readout of a data packet and the depth of the buffer for trigger data. The VFAT3 interface will run at 320 Mbps which is a factor 8 faster than VFAT2. In addition VFAT3 has many programmable options to significantly reduce pay load. This results in a much increased data throughput going well beyond the CMS specification.

VFAT3 is also being designed to be compatible with other system components foreseen for the CMS upgrades. Of particular importance is the GBT which communicates directly with the front-end chip. VFAT3 has direct compatibility with the GBT interface.

The most basic requirments for the front-end ASIC are summarized here:

- 128 channel chip
- Read positive and negative charge from the sensor
- Provide tracking and trigger information
- Trigger information : Minimum fixed latency with granularity of 2 channels
- Tracking information : Full granularity after LV1A.
- LV1A capability: LV1A latency up to 20 μs
- Time resolution of less than 7.5 ns (with detector).
- Integrated calibration and monitoring functions
- Interface to and from the GBT at 320 Mbps
- Radiation resistant up to 100 MRads (up to 1MRad needed for the muon application)
- Robust against single event effects

The block diagram for VFAT3 is shown in figure 3.3.

The VFAT3 architecture is composed of 128 channels of charge sensitive preamplifier and shaper. This is followed by a constant fraction discriminator per channel. Following the discriminator is a synchronization unit which synchronises the comparator result with the 40 MHz clock. The data then splits into two paths, one with a fixed latency for trigger signals, and the

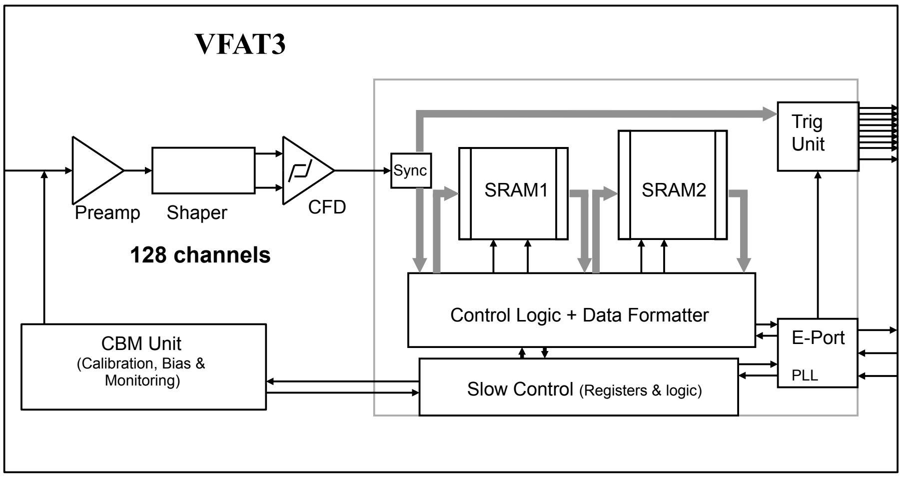

Figure 3.3: VFAT3 block diagram

second for tracking data which is non-synchronous. All communication with VFAT3 occurs through the E-port. This includes Slow Control commands and response as well as fast trigger commands, clock and calibration signals. The chip is highly programmable to offer maximum flexibility. This document aims to highlight the main characteristics and options.

3.2.1 The Analog Front-end

The analog front-end is optimized for the readout of gaseous (and in particular GEM detectors) but could also be used to read out silicon detectors. The front-end Preamplifier and Shaper are programmable to offer flexibility when connecting to detectors of different capacitances and charge characteristics. Each channel contains internal input protection to offer robustness to charge (discharge) spikes. The frontend specification is shown in table 3.1 including a list of the programmable options.

Key Parameter	Comment
detector charge polarity	Positive and Negative
Detectore capacitance range	5 - 80pF
Peaking Times (Tp)	25, 50, 75, 100, 200 ns
Programmable gain	1.25 to 50 mV/fC
Max Dynamic Range (DR)	Up to 200 fC
Linearity	$<$ 1% of DR
Power Consumption	2mW/ch
Power Supply	1.5V
ENC	$\approx 1100e\ (withTp = 100ns, Cd = 30pF)$
Technology	IBM 130nm

Table 3.1: Table of the main specifications of the analog frontend.

Signal charge from GEM detectors can last for approximately 60ns or so depending on the gas mixture. The shaping time of the front-end can be adjusted to fully integrate this charge and hence maximize signal to noise. Optimum timing resolution is maintain by the use of a CFD. Simulations show that the overall timing resolution can be maintained at around 5ns even with shaping times of 100ns or more.

The calibration system provides internal charge pulses to the input of the of the front-end preamplifier. The magnitude, phase and polarity of the charge pulses are programmable. The channel to which the charge is injected is also programmable. This feature helps significantly in the production test and charaterisation stage as well as the detector setup and commissioning stage. The functionality has two modes, one which injects a quick charge pulse (similar to a delta pulse) and the second which injects charge via a constant current for a programmable length of time.

3.2.2 Variable Latency Data Path

The block diagram for the variable latency data path is shown in Figure 3.4.

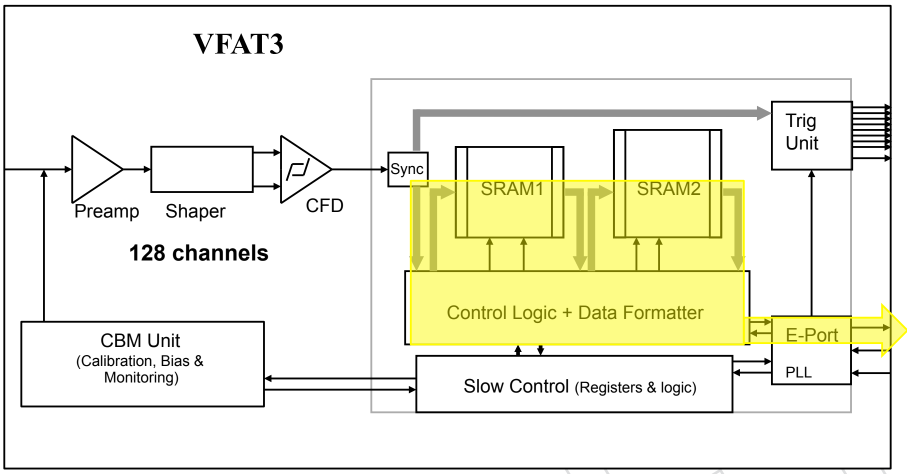

Figure 3.4: The VFAT3 Block Diagram with the Variable Data Path highlighted.

This path is used for transmitting full granularity information via the e-port. The data is reduced in time by the application of a trigger arriving with a fixed latency. For operation in LHC for tracking data, this trigger is the LV1A. The data transmitted therefore has to be accompanied via a timestamp to identify the bunch crossing associated with the data. The SRAM memories are sized to satisfy the LV1A maximum latency and rate specifications.

3.2.2.1 Data Formats

For the variable latency path there are two Data Types. The first is Lossless which is used to transmit full granularity information. The second is SPZS (Sequential Partition Zero Suppression) which has reduced size but can give losses in high occupancy environments.

An important concept for the data packet description is the use of Control Characters (CC) as headers. Encoding in the E-Port allows the use of unique CC which can act as data packet headers and inform the receiving DAQ system what type of data it is receiving.

3.2.2.2 Data Type : Lossless

The lossless data packet style is derived from the VFAT2 data packet but is optimized in terms of content.

The basic data packet is shown in the upper left corner of Figure 3.5. A unique CC acts as a header identifying the start of the packet, in this case CC-E. The timestamp is next in the form of the EC and BC numbers. The *Hit* data is represented by one bit per channel, a logic 0 represents *nohit* and a 1 represents a *hit*. If 1 or more channels are hit then there is no further attempt to zero suppress. The final piece of information is the CRC to confirm the integrity of the data packet.

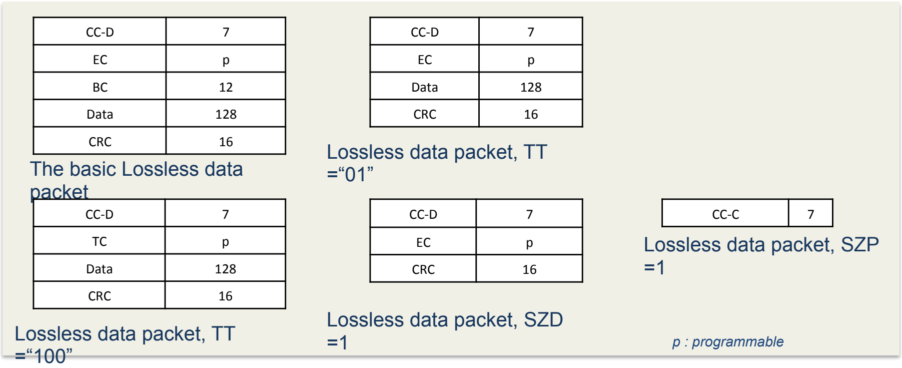

Figure 3.5: The VFAT3 Block Diagram with the Variable Data Path highlighted.

It is possible to suppress the BC time tag if only the EC is required. It is also possible to suppress the entire data field if no channels are *hit*. Indeed a further possibility is to suppress the entire data packet if no *hit* is registered and transmit only a control character. The data packets for the afore mentioned possibilities are shown in Figure 3 .

It gives flexibility for the DAQ system to decide if it requires all VFAT3s to operate synchronously sending data packets regardless of their content or to have a data driven operation where data packets are sent only when registering hits. Since most of the chips will record nothing in any given bunch crossing the latter option optimizes bandwidth enormously. Each chip however, even in the minimum setting, will respond to a LVA1 trigger by sending at least a Control Character to acknowledge receipt of the trigger signal and transmit the information no hits corresponding to this trigger.

3.2.2.3 Data Type : SPZS (Sequential Partition Zero Suppression)

The SPZS style incorporates zero suppression and is a variant on the CMS RPC data format. In this case the size of the data packet is a function of the number of hits in the chip. This enables very small data packets and hence the highest possible data transmission rate. This is very good for operation at high trigger rate. The disadvantage is that for high occupancy some losses could be incurred.

The principle is as follows: The 128 channels is divided up into 16 partitions. Each partition contains 8 channels. For each event only the partitions containing data will be transmitted. If the overall occupancy is low, there will be a bandwidth saving on the payload transmitted per event.

The basic SPZS data packet is shown in Figure 3.6. The top 3 data packets show how the basic packet would appear for 0, 1 and 2 partitions hit. The bottom 3 packets show the same but with the BC suppressed.

Since the size of the data packets vary dynamically depending on data content different CC headers are allocated to each packet size indicating the number of partitions hit.

The maximum number of partitions per data packet is limited to a programmable limit (options are from 3 to 10 partitions limit). If more than the maximum number of partitions are hit then an $Overflow$ occurs generating its own CC . Hits causing an overflow are lost.

The sequence for generating the SPZS data field is shown Figure 3.7 . The packet will have already identified how many partitions are contained within the data field. Then a sequence of *partition* bits arrive to identify which partition contains data. A 0 means empty partition and a 1 means partition containing hits. The sequence is in order, hence the first bit represents

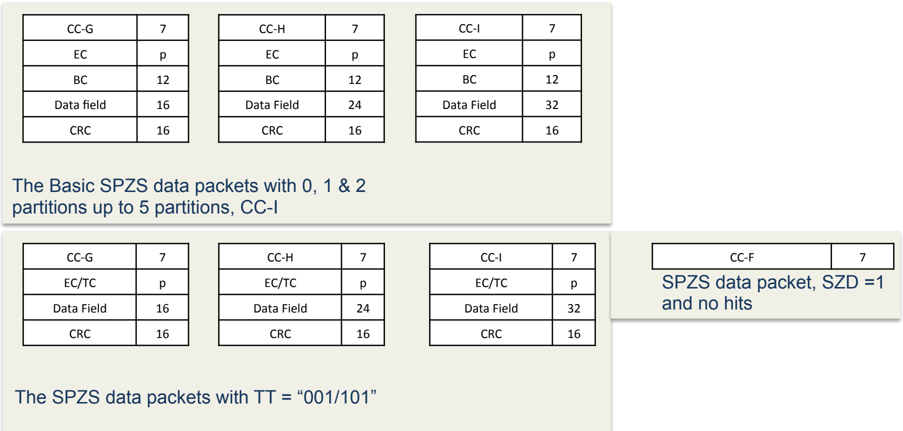

Figure 3.6: The SPZS Data Packet

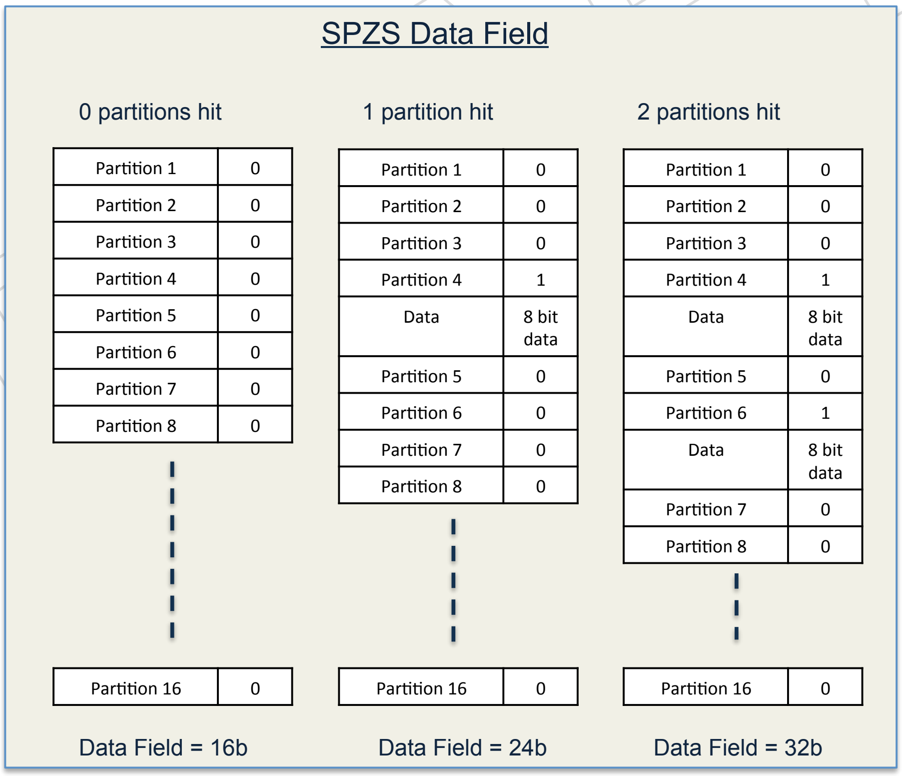

Figure 3.7: The SPZS sequence.

partition one containing channels 1-8, the second bit partition 2 containing channel 9-16 etc. If a 1 is detected in the sequence then the following 8 bits represent the 8 channels within that partition. Hence the example with 2 partitions hit shows hits within partitions 4 and 6. Once all the partitions have been read (as indicated by the CC) the sequence stops.

Time Slots per Event (TSPE) VFAT3 gives the possibility to record multiple timeslots per event, options range from 1 to 4 timeslots per event. Examples of resulting data packets (for both Lossless and SPZS) are shown in Figure 3.8 . In the lossless case the data field is increased in multiples of 128 bits for increased number of time slots. The BC will correspond to the first timeslot. Similarly the SPZS data fields can be concatenated to form a single string for multiple time slots.

Lossless Examples (PZS = “0”)

CC-D	7
EC	p
BC	12
Data	384
CRC	16

Lossless TSPE = “10” (3 time slots)

CC-D	7
EC	p
Data	256
CRC	16

Lossless TSPE = “10” (2 time slots), TT = “01”

CC-L	7
EC	p
Data Field	48-168
CRC	16

SPZS, TSPE = “10” (3 time slots)

Figure 3.8: Multiple Time Slots per Event.

An example of using this would be to program VFAT3 to get 3 times slots and setting the latency to correspond to the central time slot. It would then be possible to search for hits in the slots before and after the triggered time slot.

3.2.3 Fixed Latency Trigger Path

The fixed latency path is highlighted in Figure 3.9. The purpose is to provide fast *hit* information which is synchronous with the LHC 40 MHz clock. The *hit* information can then be put in coincidence with other detectors (such as the CSCs) to build CMS muon triggers. There are 8 SLVDS pairs are used to transmit 64 bits/bx . The format can be programmable to have trigger information based on a Fast OR of channels or using the SPZS format. 64 bits/bx allows : Fast Or : Granularity = 2 channels, SPZS : Full granularity up to 6 partitions hit.

3.2.4 Slow Control

The slow control allows the writing and reading of internal registers which in turn provides the functions of programmability and monitoring.

VFAT3 uses the E-port for all data communication including the slow control. The use of CC in the e-port allows slow control commands and data to be distinct from all other commands and

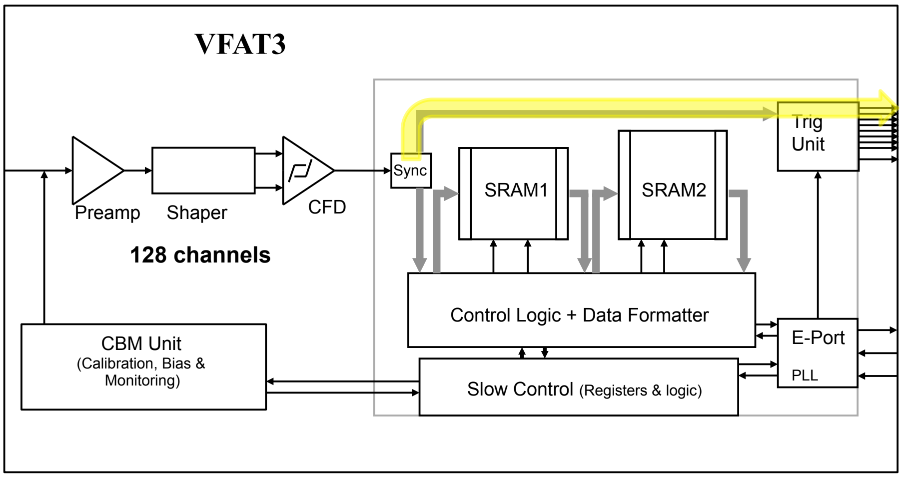

Figure 3.9: The VFAT3 block diagram with the Fixed Latency Trigger Path highlighted.

data fields. This is achieved by having two slow control CC, one for communicating a slow control 0 and the other for writing a slow control one 1.

The slow control protocol adopts the IP-bus protocol (standard within CMS upgrades) and wraps this within the HDLC protocol. This ensures correct chip addressing and error checking of slow control packets. Reception and transmission of slow control commands/data must take *low* priority when compared to real data traffic. It is therefore possible to start and stop the slow control communication in mid flow and resume when the e-port is free. The maximum allowable slow control communication rate is 40Mbps.

3.2.5 Programmability

VFAT3 is very flexible and has extensive programmability. The main programmable functions and their options are detailed in Table 3.2

3.3 The GEB board

The GEM chamber (complete with readout electronics) fits into a very narrow slot where the mechanical constraints are very tight. The limited space means that running individual flat cables to each VFAT3 hybrid is not possible. The GEM Electronic Board (GEB) was hence conceived to provide the electrical link between VFAT3 hybrids and the opto-hybrid within the limited space available.

Fabricated as a single large multilayer PCB, the GEB is a crucial element in the design of the GEM detector readout system. It's principle roles are three fold; to carry electrical signals between the front-end chips and the opto-hybrid board, distribute power and provide electrical shielding to the detector.

Biasing		
Internal Biasing		Frontend biasing via programmable 8 bit DACs
Calibration		
Channel Selection	CalChan	Selection of any individual or multiple channels for calibration.
Calibration mode	CalMode	Calibrate via V or I pulse
Charge Pulse phase (V,I)	CalPhase	Vary calibration pulse timing in steps of 3.3ns
Charge Pulse magnitude (V,I)	VCal	8 bit control on charge magnitude
Charge Pulse duration (I)	ICalDur	Current pulse length control
Charge Pulse polarity (V,I)	CalPolarity	Polarity of charge pulse (positive or negative)
CFD		
Coarse Threshold		8 bit coarse threshold affecting all 128 channels
TrimDAC per channel	TrimDAC	5 bit trimDAC for fine threshold adjustment per channel
Sync Unit & Monostable		
MSPolarity	MSPolarity	Adjust to match front-end
Mask channel	Mask	Mask possibility for each channel
Pulse Stretcher	Ps	Spreads hit over multiple time slots (1-8 timeslots)
UnSyncTrig	UnSyncTrig	Can be used to de-synchronis the trigger outputs.
Monitoring		
Monitoring of all DACs		Monitor all DACs through the slow control
Monitoring of Temperature		Internal temperature sensor and monitoring through slow control.
Control Options		
Sleep/Run Mode	SleepB	Control of SLEEP and RUN modes
LV1A Latency	Lat	Latency 25ns to 25.6μ s
Self Trig	Self Trig	For use in test beams
Probe Mode		Testability option
Data Packet Options		
Data Type	DT	Lossless, SPZS
Bunch counter	BCb	BC bits = 12 or 24 bits
Event counter	ECb	EC = 4,6,8,10,12 or 24 bits
Time Tag Type	TT	Time tag options in datapacket. EC+BC, EC only, BC only.
Suppress zero data	SZD	Suppress the data field if no hits to reduce data packet size.
Suppress zero packet	SZP	If no hits = Suppress whole data packet and send CC.
Maximum Partitions	Partitions	Max. partitions in data packet for SPZS mode; 3 to 10
Trigger Settings		
Trigger Outputs	TrigMode	FastOR of 2 channels, SPZS, 1 channel/bit, FastOR of 128 ch.

Table 3.2: VFAT3 main programmable options

3.4 The opto-hybrid and optical links

The opto-hybrid consists of mezzanine board mounted along the large side of the GEB board, with typical dimensions of 10.0 cm $\times$ 20.0 cm $\times$ 1.1 cm. The tasks of the Opto-hybrid board are to synchronize the data sent by the VFAT3 chips, zero-suppress the trigger data, code them and send them via optical links to the trigger electronics. The opto-hybrid, of which a first schematic prototype is shown in Fig. 3.10, is composed of a powerful FPGA, 3 GBT chipsets and 2 optical connectors of type SFP+.

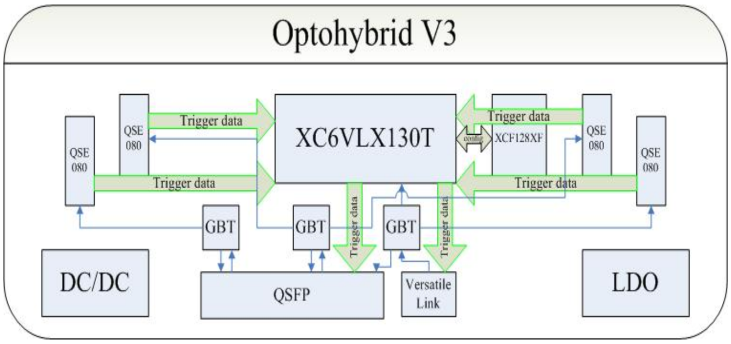

Figure 3.10: Schematic drawing of the opto-hybrid board.

3.4.1 The Gigabit Transceiver (GBT) and the Versatile Link

The CMS GEM readout system includes the use of the GBT and Versatile Link technologies under development at CERN [14]. These technologies are tolerant to radiation greater than the GE1/1 exposure levels. The GBT is an optical data link technology providing bidirectional 4.8 Gb/s serial communication with the capability to receive parallel data with an arbitrary phase, at the frequency of the LHC or at multiples of 2, 4, 8. Additionally the GBT can recover the frame clock, can reduce the jitter from an input clock, and distribute phase-controlled clock signals. The data rate (bandwidth) available to the user is lower than the 4.8 Gb/s line rate, and depends on how the GBT is configured. For the CMS GEM project the data bandwidth will reach 3.2 Gbps.

The GBT Transceiver (GBTX) will work as a full link transceiver with bidirectional data communication with the front-ends and the counting room. The GBTX delivers the global system clock reference, coming from the counting room, to all front-ends. The communication with the VFAT3 chips is made through sets of local Electrical Links (E-Links). Depending on data rate and transmission media, the E-links connections can extend up to a few meters. E-Links use the Scalable Low-Voltage Signaling (SLVS-400), with signal amplitudes that are programmable to suit different requirements in terms of transmission distances, bit rate and power consumption. The E-links are driven by the so-called E-Ports which should also be integrated in the FE chips.

The optical link will simultaneously carry readout data, trigger data, timing information, trigger and control signals and experiment-control data that must be transferred with very high reliability. To ensure an error free data transmission at high data rates in harsh radiation environments, the GBT adopts a robust line coding and correction scheme that can correct bursts of bit errors caused by Single Event Upset (SEU).

This is important because a single bit error in the control path can affect many readout channels for many clock cycles. In this mode, the GBT system can be configured over the GBT link itself. The counting room electronics will use the LHC clock to transmit commands to the VFAT3 chips and the Opto-hybrid; the GBTX will recover the LHC clock and provide it as a system clock for the entire front-end electronics.

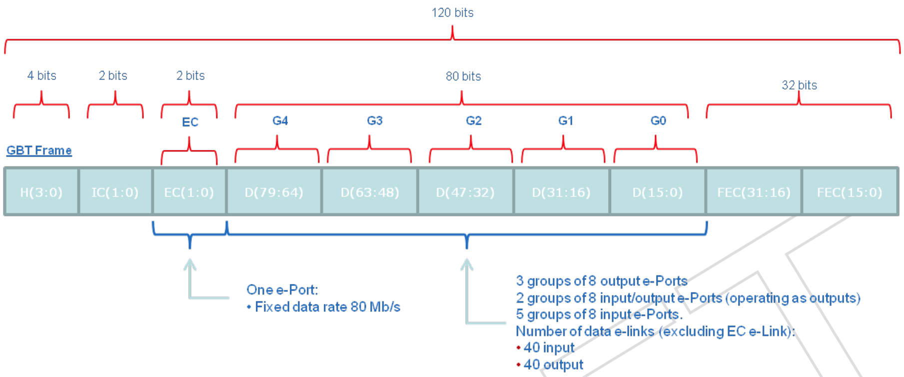

Figure 3.11: The GBT frame format.

Fig. 3.11 represents the GBT frame format consisting of 120 bits transmitted during a single LHC bunch crossing interval (25 ns) resulting in a line rate of 4.8 Gbps. Four bits are used for the frame Header (H) and 32 are used for Forward Error Correction (FEC). This leaves a total of 84 bits for data transmission corresponding to a user bandwidth of 3.36 Gb/s. Of the 84-bits, 4 are always reserved for Slow Control information (Internal Control (IC) and External Control (EC) fields), leaving 80-bits for user Data (D) transmission. The D and EC fields use is not pre-assigned and can be used indistinguishably for Data Acquisition (DAQ), Timing Trigger Control (TTC) and Experiment Control (EC) applications. DC-balance of the data being transmitted over the optical fibre is ensured by scrambling the data contained in the SC and D fields. For forward error correction the scrambled data and the header are Reed-Solomon encoded before serialization. The 4-bit frame header is chosen to be DC balanced.

3.5 The back-end electronics

The back-end Electronics provides the) interfaces from the detector (and front-end electronics) to the CMS DAQ, TTC and Trigger systems. The design foreseen for the CMS GEM off- detector electronics is based on FPGAs and Multi-GBit/s links that adhere to the micro-TCA (μTCA) standard. Micro-TCA is a recent standard that has been introduced for the Telecom industry and aims at high data throughput (2 Tbit/s) and high availability (with very low probability of interruption at 10-5). It is compact, hot swappable and has a high speed serial backplane. The μTCA is now a common standard for all the CMS upgrades and will replace the VME electronics.

The CMS GEM off-detector electronics, shown in Fig 3.12, will be composed of the preferred CMS μTCA crate, the VadaTech VT892, which supports 12 double-width, full-height AMC cards and two μTCA Carrier Hub (MCH) slots. The MCH1 slot houses a commercial MCH

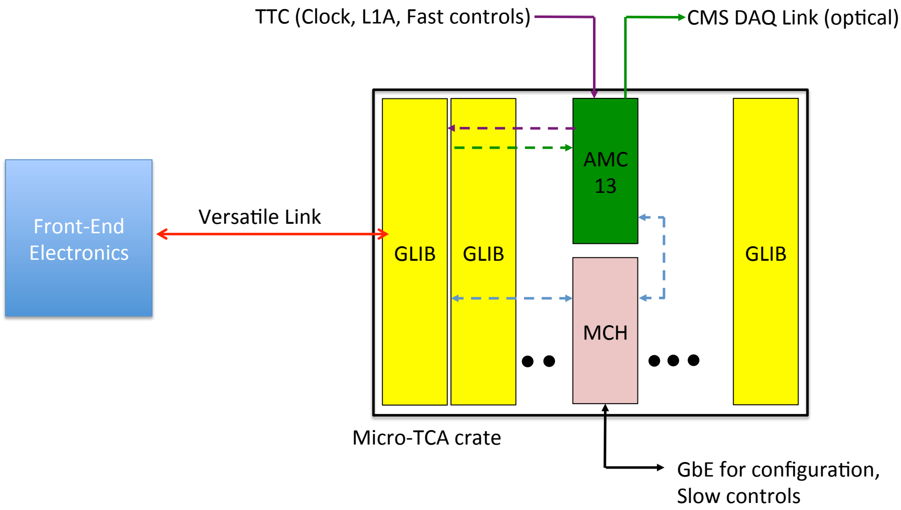

Figure 3.12: Layout of the back-end electronics μTCA crates.

module, used for gigabit Ethernet communication and IPMI control. The MCH2 slot houses a custom AMC developed by the Boston University and called AMC13. The AMC13 became the standard module within CMS to interface the μTCA crates to the CMS data acquisition system and to provide the CMS Trigger Timing and Control (TTC) signals downlink.

The AMC cards that will equip the μTCA crates will be the MP7 (Master Processor) card developed by Imperial College, London. The MP7, based on the Xilinx Virtex-7 FPGA and Avago MiniPOD optical modules, can provides 72 optical transceivers and 72 optical receivers, capable of operating above 10 Gbps. Eight MP7 boards would be needed to read-out the entire GE1/1 system. They would all be hosted in one μTCA crate.

For the optical link between the opto-hybrid and the MP7 boards, the GBT protocol will be used for data transmission over 48 way MTP cables.

3.6 Trigger path to the CSC

The trigger data will be sent in parallel to the Cathode Strip Chamber (CSC) Trigger Mother Board (TMB) to be combined with the CSC data and to improve the Level-1 trigger efficiency of the CSC system. To send the trigger data to the CSC TMB we will use existing optical fibers located along the CSC detectors inside CMS. These fibers cannot sustain the GBT protocol. The 8B/10B protocol will be used instead. The GEM-CSC data flow is described in section 4.2.

Chapter 4

Data Acquisition and Trigger

Editors: G. De Lentdecker, J. Hauser, A. Marinov, A. Safonov

4.1 DAQ data flow

Upon Level-1 Accept (L1A) signal, the full granularity data stored in the VFAT3 SRAM2 memories will be formatted by the Data Formatter and sent-out the chip through the E-port towards the GBT chipset. One GBT chipset will read-out 8 VFAT3 chips. The format and content of the data packets has multiple different options and are described in section 3.2.2.1. In the case of the basic lossless data format, the data rate per optical link will amount to less than 200 Mbps at L1A rate of 100 kHz.

Note that the GBT is fully transparent to the user data being transferred. In the GBT chip, after phase alignment, the data coming from the VFAT3 chips through the E-ports is first processed by the scrambler, a 4-bits header is then added, the Reed-Solomon (RS) encoding and interleaving takes place and finally the data is serialized. While the scrambler maintains the word size, the RS encoder adds the 32-bit Forward Error Correction (FEC) field adding up to a total frame length of 120 bits. This leads to an overall line code efficiency of 84/120 = 70%. At the receiver end the inverse operations are repeated in the reverse order. There the tasks will be performed by the AMCs located in the μTCA crates (see section 3.5).

As described in section 3.4.1, each GBT data link will carry 80 bits of user data for every LHC bunch crossing. Each GBT link will handle the data of 8 VFAT3 as shown in table 4.1. The control character indicates which data format is being sent. The possible data formats are described in section 3.2.2.1. BC0 indicates that this sample is from the bunch with number zero in the orbit. This bit is used for latency/alignment of the data links. The packet number indicates the sample number.

Figure 4.2 shows the sharing of the optical links from the GEM detectors to the back-end electronics. Each MP7 can receive up to 72 high speed optical links, that is 12 GE1/1 super-chambers tracking data. In total, one GE1/1 endcap require 3 MP7 boards to read-out the tracking data and 1 MP7 for the trigger data. The full GE1/1 data can be hosted by one μTCA crate.

The rate of the incoming GEM data per MP7 card will be $\sim$ 10 Gbps at 100 kHz for the loss less data format. After data reduction, the DAQ data will be sent through the μTCA backplane from each MP7 board to the AMC13 board which will then transmit the data fragments to the CMS DAQ system. The DAQ capacity of the AMC13 amounts to three 10 Gbps links. Data reduction on the MP7 boards can be easily achieved by requiring the matching of hits in the two GEM detectors making one super-chamber.

Byte	7	6	5	4	3	2	1	0
0	Control Character							
1	Packet Nbr [6:0]							BC0
2	VFAT 0							
3	VFAT 1							
4	VFAT 2							
5	VFAT 3							
6	VFAT 4							
7	VFAT 5							
8	VFAT 6							
9	VFAT 7							

Figure 4.1: GBT link data format. The control character indicates which data format is being sent. BC0 indicates that this sample is from the bunch with number zero in the orbit (used for latency/alignment of the data links). Packet Nbr indicates the sample number.

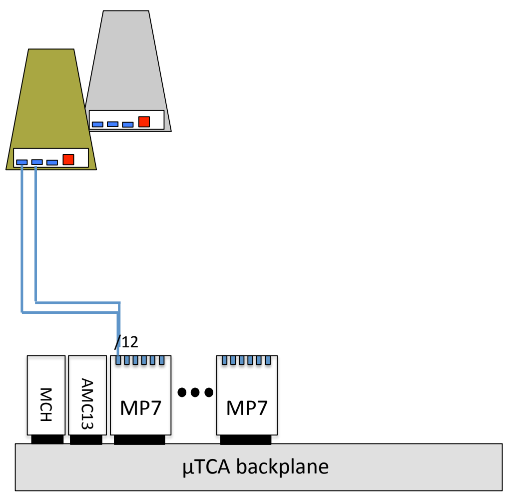

Figure 4.2: Sharing of the optical links.

4.2 GEM-CSC trigger data flow

The fixed latency data, also called trigger data, will be sent by each VFAT3 chip (see section 3.2.3) to the front-end FPGA on the Opto-Hybrid board through 8 SLVDS pairs to transmit 64 bits/bx per VFAT3, each bit representing the logical 'OR' of two adjacent strips, that is a pad. The data will then be sent to the Cathode Strip Chamber (CSC) Trigger Mother Board (TMB) to be combined with the CSC data and to improve the Level-1 trigger efficiency of the CSC system.

At an average particle rate of 10 kHz/cm^2, we expect 1.2 hit/bx/GEM, which means that most of the bits will be '0'. On the front-end FPGA a FSM will look for non-'0' bits and encode the pad position in the following way: 6 bits (padId) + 2 bits (ϕ column) + 3 bits (η-partition) = 11 bits.

Two optical fibers will connect the front-end FPGA to the CSC TMB. These fibers do exist and are located along the CSC detectors inside CMS. These fibers cannot sustain the GBT protocol. The 8B/10B protocol will be used instead, each providing 48 bits/bx for data. Consequently up to 8 trigger hits per GEM detector can be sent to the CSC TMB at each LHC bx.

The GEM trigger data should arrive at the CSC TMB within a latency of 17-18 bx. Table 4.1 shows the breakdown of the latency of the GEM-CSC trigger data path.

Table 4.1: Latency in bx of the GEM-CSC trigger data path.

Component	Latency (bx)
TOF	1 - 2
VFAT3	5
GEB	1
FPGA	2
SFP	5
Fiber (15 m)	3
Total	17 - 18

4.3 DAQ firmware and Software

4.3.1 MP7 and μTCA control

The μTCA standard does not specify any details of the communication between a control PC and an AMC beyond the low-level transport specification of gigabit Ethernet. The CMS Upgrade Working Group has adopted a standard protocol called IPBus to provide a uniform solution for communication across all CMS upgrades which will use μTCA. The protocol defines a virtual A32/D32 bus on each Ethernet target and allows the programmer to pack multiple read, write, bit-set, and bit-clear operations into a single Ethernet packet. The base protocol uses the User Datagram Protocol (UDP) over the Internet Protocol (IP). The use of UDP rather than bare Ethernet allows development of control code with no specialized drivers or enhanced machine access standard user accounts and interfaces can be used for all purposes. The use of UDP/IP instead of TCP/IP greatly reduces the complexity of the implementation in the FPGA firmware of the AMC. Reliable delivery is ensured by a software server layer which manages multiple parallel requests for the same resources across multiple clients. The IPBus protocol and firmware module are supported by the Bristol University group.

4.3.2 Overview of the online software

The online software of the GEM readout system is designed according to the general scheme of the CMS online software. The implementation is based on the generic solutions provided by the CMS software framework: XDAQ, Trigger Supervisor, etc.

The direct steering of the hardware is performed on the computers controlling the μTCA crates. The central control over the hardware is split in two:

- the XDAQ applications providing access to the AMC boards receiving the GEM tracking data and the AMC13 are managed by the GEM node of the Function Manager,
- the XDAQ applications providing access to the AMC boards receiving the GEM trigger data and the opto-hybrid boards are managed by the GEM cell of the Trigger Supervisor.

The software is abstracted into several layers. The Hardware Access XDAQ application is a custom class derived from the *Application* class provided by the XDAQ package. At the lowest level, are the interfaces to the IPBus protocol. Above this layer is the standard CMS μHAL layer which defines the access functions (Write, Read, ...). The next layer above becomes board dependent. However since the boards receiving the GEM trigger or the tracking data are the sames, the C++ classes will be essentially identical. Functions like Reset, Configue, Start, Finished, etc. are defined at this level.

4.3.3 DAQ Prototype

In 2014 a first GEM DAQ system is being developed to read-out VFAT2 chips, while the VFAT3 chip is being designed. The system is composed of new CMS VFAT2 hybrids mounted on the first version of the full size GEB board on which the first version of the opto-hybrid is placed. The layout of this first version of the opto-hybrid is shown in Figure 4.3. This version of the opto-hybrid can read-out only 6 VFAT2 chips. The opto-hybrid is read-out by a GLIB board installed in a μTCA crate, controlled through IPBus. Since the Spartan 6 FPGA does not have high-speed transceivers to run beyond 3.2 Gbps, the GBT protocol could not been implemented, but a simpler 8b/10b encoding. However the GBT protocol has been tested separately between a GLIB board and a Virtex 6 development board, successfully. This prototype is a proof of concept of the full GEM read-out chain, allowing the test among others the signal integrity in the GEB PCB as well as between the GEB and the opto-hybrid, to measure the power consumption, etc.

Although the DAQ prototype differs from the final design in multiple ways, the firmware developed for the first version of the opto-hybrid and the GLIB will be compatible with the later versions of the opto-hybrid and the MP7 respectively with minimal changes. The current version of the system focuses on the control of the VFAT2 hybrids through IIC which allows the software developers to test several functionalities of the chip as well as the communication between the several components of the DAQ chain.

To handle the communication between the computer and the back-end electronics, a dedicated IPBus slave has been implemented on the GLIB to translate the IPBus requests to a custom data format. The addresses used by IPBus to execute read/write operations are mapped to the physical registers in the VFAT2 hybrids by operating the translation described in Table . Each IPBus slave is connected to one optical link controller and thus one opto-hybrid. This means

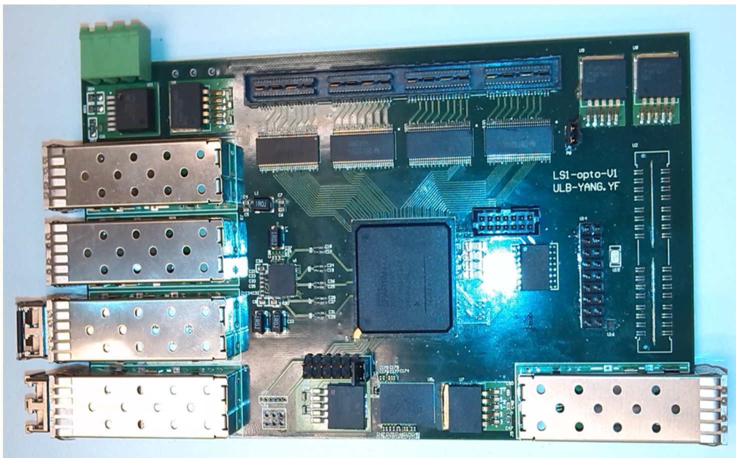

Figure 4.3: Layout of the opto-hybrid v1. It is equipped with a Spartan 6 FPGA.

that one slave can address up to 24 VFAT2 hybrids and in each of them 152 registers. Therefore, the *Chip select* parameter is used in order to select which VFAT2 on the GEB must be addressed and the *Register select* in order to pick the correct register in the VFAT2 hybrids.

Table 4.2: Mapping between the 32 bits IPBus addresses and the VFAT2 hybrids' registers for IIC requests.

0x4001	XX	XX
Fixed part of the address	Chip select on the GEB	Register select in the VFAT2

Once the data has been translated by the IPBus slave, it is transmitted to the optical link controller which is in charge of formatting the data to be sent to the opto-hybrid. This core also prioritizes the outgoing requests and dispatches the data coming from the opto-hybrid to the various components on the GLIB. In order for the data to be correctly received and interpreted by the opto-hybrid, it must be formatted as represented in Table 4.3. The latter is sent to the opto-hybrid over an optical link using the 8b/10b encoding.

The opto-hybrid decodes the packet and transmits the information to an IIC control core which addresses the VFAT2s mounted on the GEB. Upon response of the VFAT2 chips, the data is sent back to the GLIB through the reversed path using the same data format. Once the data has been dispatched on the GLIB, the IPBus slave formats the data to be sent over Ethernet to a host computer. As VFAT2 registers are only 8 bits long, the remaining 24 bits of the IPBus data packet is used to send other data. The complete data packet format is listed in Table 4.4.

The control of the DAQ through IPBus is performed using a small Python script on a host computer which allows for more flexibility and faster debugging that XDAQ. So far, we obtained an integrity of 100% for the GLIB data transfer and formating by creating a loop-back with the optical link. The communication with the opto-hybrid and the GLIB has also been tested and

Table 4.3: Formating of the data for an IIC request sent over the optical link.

47 - 40				39 - 32
IIC packet type ID				Fixed byte for comma detection
31	30	29	28 - 24	23 - 16
Error bit	Valid bit	Read/$\overline{\text{Write}}$	Chip select	Register select
15 - 8				7 - 0
Data				CRC

Table 4.4: Data format of an IIC IPBus request.

31 - 27	26	25	24	23 - 21	20 - 16	15 - 8	7 - 0
Unused	Error bit	Valid bit	Read/$\overline{\text{Write}}$	000	Chip select	Register select	Data

matches the requirements. The opto-hybrid is able to recognize and handle incoming requests. Finally, the control of the VFAT2s from the opto-hybrid over IIC also works as expected. The remaining step to perform is to transfer the data from the optical link to the IIC core on the opto-hybrid.

Chapter 5

Chamber Production and Quality Assurance

Editors: O. Bouhali, P. Karchin, L. Benussi, A. Sharma

5.1 GEM Production and Assembly plan

The final chamber quality and performance depend on the production quality and on the accuracy of the assembly operation. Throughout the production and assembly operations, systematic inspection are taken place. Standard procedures have been discussed and are implemented in the production centers involved in the project. A comprehensive workflow had to be defined to ensure a smooth production of components and their assembly.

5.1.1 Production protocols and assembly workflow

- List of components, their production origin, quantities, responsibility
- Procedure for different component validation

5.1.2 Production sites specification

The GE1/1 chamber assembly will be organised in 4 production site There is a minimum requirement of hardware and expertise for a site to be a production site. The site must have a well record track of GEM chambers production and testing experience, including quality control checkup, gain measurements, successful participation to test beam campaigns with the chambers produced from the center, sufficient manpower and skills. The following is a list of mandatory requirements for the production site:

- Personnel well trained in th assembly of GE1/1 chambers. The training will be done (at CERN?) on dedicated final prototypes. The personnel must also be trained to operate in a clean room and must understand the meaning of each single step of the whole process.
- Sufficient and adequate space with dedicated areas for testing, assembly and storage. It is mandatory the presence of a dedicated space for the unpacking of the different components coming from the different production sites and their optical inspections. It is also necessary the presence of a dedicated area in which safely pack the assembled chambers and store them before shipping to CERN.
- Clean room of good class (at least 1000) to assemble the GE1/1 chambers. The clean rom must have a vestibule necessary for the dressing of the personnel that will assemble the chambers. In the clean room there must be presente a assembly bench large enough to allow the full GE1/1 assembly. Must be present also auxiliary

benches to allow the placement of the several parts during the assembly procedure. The GE1/1 assembly must be done avoiding as much as possible the movement of the GEM foils before they final stretching so that the assembly bench must have around enough space to allow personnel to move freely around it during the assembly process. The clean room must be equipped with clean and dry nitrogen gas lines used to blow the different chambers part during assembly. The chamber must be also equipped with proper tools to clean the different components as clean tapes and sticky rolls to remove possible residual of dust on the GEM foils. The clean room must also contains cabinet for the storing of the assembly tools.

- The gas system must be realised with stainless steel pipes and leak proof. Any single component , i.e. valves, unions, manometers etc, must be deeply cleaned to remove any residual of oils from their production. The gas system mu be thought to be operated with CF4 based gas mixtures, which means that all gas system components must be suitable to be used with fluorine. There must be filters which will remove possible water contamination from the pipe. Obviously it is highly forbidden the use of oils bubblers or similar in any part of the gas system. Bubblers must be substituted with rotameters
- Dark currents measurement station. Must be a nitrogen flushed box of dimension large enough to comfortably house a GE1/1 foils. The chamber must also have electrical connection necessary to apply 500 V to the a single GEM foil under test and allow the current drawn. The nitrogen flushing in the dark current box must be absolutely dry and clean.
- Gain uniformity station X-ray setup to check the chambers uniformity (gain) **I will ask Brian to provide me the list of components of the gain measurment setup**
- **Gas leak measurement station. In this area the assembled chamber will be tested for gas leak. The station must be equipped with dry and clean nitrogen gas line and with a manometer to measure pressure drop of the order of few decimal of mbar/h. The proposed method is a U-shaped tube with millimetre scale for the reading. The U tube must be filled with water. No vaseline oil or similar is allowed. Since the gas leak measurement will be done with dry and clean nitrogen the piping can be done with cleaned plastic tube.**

5.1.3 Production protocols and assembly workflow at sites

Figure FIXME shows the workflow for chambers assembly and test at production sites.

Figure 5.1: Workflow of a standard assembly procedure at production sites

5.1.3.1 Production and quality check of components

Quality Control of HV divider The HV divider is a chain of resistors used to deliver the voltages to the drift plane and the three GEM foils (figure FIXME). It is a ceramic bar, coated with a layer of high-resistance materials. A HV test is applied to the divider and the I-V curve is used to check the resistor value at each stage of the chain. The HV divider is produced by the production sites themselves. **Drift PCB** An optical inspection is performed in the clean room to identify possible scratches and defects. A nitrogen gun is also used to clean the drift plane for possible dust. The drift plane is connected to the HV. The final step is a HV test with progressive HV ramping to check for possible sparks and/or changes in the impedance. **PCB Readout**In this part, PCB the readout is inspected for possible short between strips or interrupted strip-readout connection. A special connector is used to check simultaneously all the strips in one PCB readout set. **GEM foil** The GEM foil must be handled and tested in a clean room. An optical inspection is first performed to identify defects, scratches, irregular hole size, contact between top and bottom metals. A microscope is also used when necessary to further investigate micro defects. The quality of the foil (leakage current and impedance) is checked using Meg-ohmmeter. With an applied potential difference of 500 V between the GEM metal sides, the GEM foil should draw a current no more than 30 nA.

5.1.3.2 Detector assembly

The different components are assembled with a well documented procedure in each site. Figures FIXME1, FIXME2 and FIXME3 show respectively: the preparation of the drift plane, placement of one of the GEM foils, placement of the readout board before closing the detector.

The detector is then flushed with nitrogen.

Preliminary gain measurements are mad with a portable x-ray generator. Then a full test is performed using X-Ray generator and/or cosmic rays to check the gain and uniformity

The uniformity response test is one of the quality check procedures for final chamber acceptance. The full chamber is illuminated with a X-ray source. The signal is collected on each strip. More details on the uniformity test were given in chapter 2.

- QC0 - Control done by the site (most probably CERN) that will receive the material from companies with the aim to individuate bad production by visual inspections. The material passing the QC0 will by shipped to the assembly site. Shipping done following a checklist in order to be sure that all the material is sent to the sites
- Description of the different steps and stations of the production: gluing station, bonding station, HV test station,
- Preliminary QC of the assembled chamber

5.1.4 Gain uniformity test and chamber facility

- QC1 Assembly site will control materials received confirming that they are ok for assembling. Unboxing done by checking on the same checklist use for the shipping. GEM foil leak current test following the FIT plexi-box technique. Readout plane checked for possible bad connectors soldering. Test done with dedicated tool checking correct connectivity.
- QC2 after chamber assembly the chamber is tested for gas leak with pure, dry and filtered nitrogen. Chamber pressurised up to 20 mbar (maybe even more) and kept under such pressure for some hours. Chambers not leaking will be flown with Ar/C02 and after 12 hours (?) started to be turned on. Chamber not drawing too much current (how much??) will be declared passing QC2
- QC3 - Gain uniformity done with x-ray source. The X-ray sources must have the same target (Ag) for obvious data normalization reasons. 1) Which granularity we require for the gain uniformity? Do we really need to see that each strip is uniform" within some percent with the other strips, or it is enough to have a bin size of, i.e. 12 strips, in terms of gain uniformity? 2) It is reasonable to reject a chamber that has a "bad" strip, or in other words, which is the critical number of strips above which a chamber is rejected? 3) What we do with a rejected chamber? It is that is surely worthwhile to recover it directly in the corresponding assembly site, but maybe it could be also reasonable to plan to have a certain number of spare production cham-

ber (10% for each site) to absorb bad production (10% is a estimation based on no data basically). I mean, once we find a bad chamber not passing QC3, we keep it in ”standby” going on with the production, moving the chamber in the 10% of spare parts. Once the production is over, the corresponding production site will try to recover it. The reason of this ”pr tocol” is to not stuck the production in the recovery procedure.

5.1.5 Gain uniformity test and chamber facility

- Detailed description of the gain uniformity procedure, refer to uniformity studies of chapter 2
- Question: are all production sites equipped for gain uniformity test?
- Duration of the procedure, assembly and production frequency and timeline
- Criteria for chamber validation: gain variation, leakage current, number of dead channels, any alignment criteria?
- Detailed description of the gain uniformity procedure, refer to uniformity studies of chapter 2
- Question: are all production sites equipped for gain uniformity test?
- Duration of the procedure, assembly and production frequency and timeline
- Criteria for chamber validation: gain variation, leakage current, number of dead channels, any alignment criteria?

5.1.6 Reception of chambers at CERN and validation protocols (OB, PK, MA)

As discussed above, the production plan foresees the assembly of the chambers at specific sites outside CERN. The anticipated time for the assembly and production is NNN. After the production and quality checks at production sites, the chambers will be shipped to CERN where they will conduct additional uniformity tests and stored for final installation. Upon reception of chambers at CERN, it is very important to conduct a quality check procedure. This includes three steps:

5.1.6.1 HV training test

In this phase, the gas is flushed through the chamber and the high voltage is raised slowly with a rate of NNN V/hour. A HV point of NNN must be reached without problem. The chamber should stay at this HV point for 24 hours. HV stations (see Figure 5.2) are dedicated for this operation.

5.1.6.2 Electronic test

In this phase the electronics is tested. The goal is to identify possible dead/noisy channels and broken bondings that might arise from the shipping. A dedicated test station is foreseen for this procedure. The overall test procedure should not take more than NNN h/chamber.

5.1.6.3 uniformity test

Once the above tests are successful, we proceed to the response uniformity check over the large surface of the chambers. The operation has to be fast and efficient. We plan to achieve these goals by using the Gamma Irradiation Facility (GIF) at CERN (figure 5.3). Chambers will be fully scanned with a Cu-based X-ray beam. The test chambers will be placed at a distance of around 1m from the source. With this setup one can look at the chamber response across one

Figure 5.2: Schematic view of the HV station used for teh HV training test.

Figure 5.3: Schematic view of the setup used to study the gain uniformity as part of the quality control procedure.

fixed η-sector (figure **??**, left), and across the full active area of the test chamber (figure **??**, right). In previous test [**?**] no more than 15% variation was observed across the full active area of the chamber. This limit should be preserved during the final production.

5.1.7 Cosmic ray tests (OB, PK, MA)

In addition to the above-mentioned tests, a cosmic ray test is also foreseen. The goal of the setup is to validate the chamber performances and the electronics onboard. Figure 5.4 the cosmic stand setup built at CERN for tis purpose. The setup is made to allow several chambers (up to 3?) to be tested at the same time. The setup includes the following features:

- Fully automatic HV scan: to allow measurement of the gain, efficiency and spatial resolution.
- the setup allows to measure tracks with incident angles up to FIXME. It also allows to cover a large area of the chamber.
- DAQ system: comparable to the final one allowing to test the electronics onboard.
- Data Storage and analysis: raw data will be stored on disk for further offline processing. A central software code will be developed to allow fast online data analysis.

Once this stage is completed, the chamber is declared ready for final installation.

5.2 Super Chamber production

A super-chamber (SC) is fabricated by coupling together two back-to-back GEM chambers. The number of readout channels for each SC is FIXME.

5.2.1 Mechanical assembly and QC

Missing

5.2.2 Final electronics connectivity and integration

Missing

5.2.3 Final QC procedure

Missing the following items are left for a later discussion:

- Which sites are taking part in production/assembly?
- Backup sites for possible local problems
- Production proportion for each site

Figure 5.4: Schematic view of the Cosmic Stand at CERN.

5.3 Database

All aspects of assembly procedure and components are stored in a common database. The DB is based on Oracle and contains the following:

- Main detector components: the Chip FrontEnd, GEB board, GEM Frames, cooling. For each component the validation results will be recorded as well.
- Detector assembly: contains information about the assembly and quality check procedures of the chamber. It also includes preliminary validation tests: gas leak, connectivity channel, electrical tests..
- Detector performance: includes results from X-ray and cosmic rays tests. It will contain plots from Full HV scan, cluster size, noise and detector conditions (thresholds, gain + environmental conditions and site assembly, date, location, operator..)

Chapter 6

System Performance

Editors: P. Giacomelli, A. Colaleo, K. Hoepfner, A. Safonov

6.1 LHC Conditions for the operation of GE1/1

After the second long shutdown (LS2), planned for 2018 to upgrade the LHC injector chain, the instantaneous luminosity ($\mathcal{L}$) will approach, or exceed, 2×10^{34} cm^{-2}s^{-1}. Phase 1 of the LHC will end around 2022, when an integrated luminosity (L) of $\sim 300\,\text{fb}^{-1}$ is expected to have been collected. A high-luminosity upgrade to the LHC interaction regions is foreseen during a third long shutdown (LS3) to further increase the instantaneous luminosity to 5×10^{34} cm^{-2}s^{-1}.

Table 6.1: Possible operating scenarios for the LHC after LS1 [**?**].

Scenario	# bunches	I_p ($\times 10^{11}$)	Emittance (μm)	$\mathcal{L}$ (Hz/cm^2)	Pile-up	L (fb^{-1}/year)
25 ns	2760	1.15	3.5	9.2×10^{33}	21	24
25 ns low emit	2320	1.15	1.9	1.6×10^{34}	43	42
50 ns	1380	1.6	2.3	$0.9\text{–}1.7 \times 10^{34}$	40–76	45
50 ns low emit	1260	1.6	1.6	2.2×10^{34}	108	–

The CMS experiment is expected to make major new discoveries at the LHC and make precision measurements of the properties of the fundamental particles and interactions. The key to these discoveries and measurements is the ability to trigger on, and reconstruct, muons with high efficiency. The muon trigger and reconstruction algorithms are designed to achieve these goals. Here we present the current performance of the algorithms and the effects due to two additional layers of GEM in the most inner station of the forward muon station during the post LS2 LHC operation. Results do not include effects such as miscalibration or detector inefficiencies, except those caused by the detector geometry. Event environments and beam induced backgrounds are also studied.

6.2 Simulation: data samples and workflow (Ahmed and Yasser)

The performance of the algorithms has been evaluated using the full detector simulation with a magnetic field of 3.8 Tesla. The performance has been tested using muon gun samples generated with different values of p_T and flat distributions in η and ϕ and in the presence of more than one muon and with non-flat distributions.

6.3 Muon reconstruction (Anna)

The categories of reconstruction analyzed are

- Stand-alone reconstruction: this just uses hits in the muon detectors
- Global Reconstruction: this starts with the muon segment information and then adds tracker information
- Tracker Muon reconstruction: this starts with tracks found in the inner tracker and identifies them as muon by matching expected information from the calorimeters and muon system.

In all cases the beam spot position is used as a constraint.

6.3.1 Local Reconstruction (Anna, Raffaella)

Muon reconstruction is based on the concept of local reconstruction where the output of the data acquisition system is used to build the basic reconstructed objects to be used by the following reconstruction steps. In the muon detectors, the reconstructed objects may be simple points or segments giving both position and direction information. After the local reconstruction, muons can be reconstructed at regional (standalone muons), by using just the information of local reconstruction coming from the muon system, and at global level (global muons), by combining the information from all the muon system and the tracker. The CMS High Level Trigger follows exactly the three steps described above to carry out muon reconstruction for the on-line event selection. The HLT standalone and global reconstruction are called Level-2 and Level-3 reconstruction, respectively.

The reconstruction units providing local reconstruction in a detector module use as input real or simulated data (“digis”). The output from the reconstruction units are “recHits”, reconstructed hits which are typically position measurements (from times or clusters of strips or pixels) in tracking-type detectors (Muon and Tracker systems) and calorimetric clusters in Calorimeter systems. The RecHits are used as the input to the global reconstruction.

In the GEM subsystem the result of local reconstruction are points in the plane of the detector. First, a clustering procedure starting from all strips that carry signals is performed. The procedure consists of grouping all adjacent fired strips. Once all groups are formed, the reconstructed point is defined as the “center of gravity” of the area covered by the cluster of trapezoidal strips. The assumption here is that each group of strips is fired as a result of a single particle crossing and that this crossing can have taken place anywhere with flat probability over the area covered by the strips of the cluster. Errors are computed under the same assumption of flat probability as $\sigma_x = (\text{cluster size})/\sqrt{12}$

6.3.2 Tracking of Charged Particles and Parameter Measurements in CMS

The strategy for physics analyses in CMS is based on the reconstruction of high-level physics objects which correspond to particles traveling through the detector. The detector components record the signal of a particle as it travels through the material of the detectors, and this signal is reconstructed as individual points in space known as recHits. To reconstruct a physical particle traveling through the detector, the recHits are associated together to determine points on the particle trajectory. The characteristics of the trajectory as it travels through the detector are then used to define its momentum, charge, and particle identification.

Measuring the full trajectory in the space of a charged particle in a magnetic field provides a method to determine the momentum ($\overrightarrow{p} = m\gamma\overrightarrow{v}$) and charge, q. The Lorentz force provides a relation between the momentum and its motion in a magnetic field, and allows the determination of the equation of motion for the trajectory of the charged particle. Parameterizing the Lorentz force as a function of the distance along the trajectory, $s(t)$, the trajectory is given by the differential equation:

$$\frac{\mathrm{d}^2 \overrightarrow{r}}{\mathrm{d}s^2} = \frac{q}{p} \frac{\mathrm{d}\overrightarrow{r}}{\mathrm{d}s} B(r) \tag{6.1}$$

where $\frac{\mathrm{d}\overrightarrow{r}}{\mathrm{d}s}$ is the unit length tangent to the trajectory, and $\frac{\mathrm{d}^2 r}{\mathrm{d}s^2}$ is a measure of the trajectory's curvature.

The above parameterization does not take into account three important factors caused by the real CMS detector:

1. inhomogeneous $\overrightarrow{B}$ field;
2. the energy loss as the particle travels through the detector;
3. the multiple scattering which deflects the trajectory in a stochastic manner.

Therefore, a failure to include these effects biases the most important parameters that are extracted from the trajectory: the momentum and its direction. An accurate measurement of direction is critical in determining whether the particle came from the interaction point or a detached vertex. In order to take into account these effects we use a different set of parameters that scales with the changes mentioned.

The magnetic field is a function of the coordinates $\overrightarrow{B}(x, y, z)$, therefore to correctly describe the trajectory it is necessary to incorporate the magnetic field changes into the parametrization. The set of parameters $\{x, y, x', y', q/p\}$, at a reference surface $z = z_r$ together with the derivatives with respect to z, provides the change from the ideal trajectory. This new parametrization also scales with the effects of multiple scattering and localizes the trajectory to a plane region where the $\overrightarrow{B}$ field can be expanded as a perturbation to a good approximation. Thus, a solution to the trajectory in an inhomogeneous $\overrightarrow{B}$ field can be found by using a recursive method of Runge-Kutta.

In order to uniquely specify a trajectory of a helix in a region of known magnetic field, one needs to specify at least five degrees of freedom, where a unique determination would require infinite precision on the five parameters. For large momenta, the projection of the trajectories can be approximated by a straight line $y = a + bz$ in a plane containing the magnetic field and with a parabola $y = a + bx + (c/2)x^2$ in the plane normal to the magnetic field, with $c = -R_T^{-1}$. The uncertainties on the above parameters due to the intrinsic resolution of the detectors translates directly into an uncertainty on the momentum vector. Using typical values expected in CMS, the intrinsic momentum resolution of the detector has the following features:

1. the resolution grows linearly in momentum and drops as B^{-1} and L^{-2};
2. the transverse resolution dominates over the full η range in CMS.

6.3.2.1 Material Effects

A charged particle will be deflected by random Coulomb scattering with the material of the detector. For sufficient material (length L), the deflection angle from its unperturbed trajectory becomes Gaussian distributed around zero. The scattering introduces an uncertainty in the position measurements and a correlation in the measurements after the material scattering. In cases where the multiple scattering dominates the uncertainty, the momentum resolution does not depend on the momentum, but there is a weak dependence on the number of measurements for a fixed amount of material and on the length of the spectrometer. Although ionizing single atoms in a medium requires a relatively small amount of energy transfer, the additive effects do contribute in a well understood manner. The average energy loss for charged particles heavier than the electron is given by the Bethe-Bloch formula, that provides the statistical energy loss per unit x (density $\times$ length). The loss of energy has to be incorporated in the equations of motion.

6.3.3 Muon Reconstruction in the Muon Spectrometer

Based on the Kalman filter technique, track reconstruction starts with the estimation of the seed state from track segments in the off-line reconstruction and from the trajectory parameters estimated by the Level-1 trigger in the on-line. The track is then extended using an iterative algorithm which updates the trajectory parameters at each step and, in order to reduce the possible bias from the seed, a pre-filter can be applied before the final filter. Once the hits are fitted and the fake trajectories removed, the remaining tracks are extrapolated to the point of closest approach to the beam line. In order to improve the p_T resolution a beam-spot constraint is applied.

The track reconstruction handles the DT, CSC, RPC and GEM reconstructed segment/hits and it can be configured in such a way as to exclude the measurements from one or more muon subsystems. The independence from the subsystem from which the measurements come is achieved thanks to a generic interface also shared with the inner tracking system. This allows the tracker and the muon code to use the same tracking tools (such as the Kalman filter) and the same track parametrization.

6.3.3.1 Seed Generator

The algorithm is based on the DT, CSC and GEM segments.

A pattern of segments in the stations is searched for, using a rough geometrical criteria. Once a pattern of segments has been found (it may also consist of just one segment), the p_T of the seed candidate is estimated using parametrisations of the form:

$$p_T = A - \frac{B}{\Delta\phi} \qquad (6.2)$$

For DT seed candidates with segments in MB1 or MB2, $\Delta\phi$ is the bending angle of the segment with respect to the vertex direction. This part of the algorithm assumes the muon has been produced at the interaction point. If segments from both MB1 and MB2 exist, the weighted mean of the estimated p_T's is taken. If the seed candidate only has segments in MB3 and MB4, the difference in bending angle between the segments in the two stations is used to calculate p_T.

In the CSC and overlap region, the seed candidates are built with a pair of segments in either the first and second stations or the first and third stations. $\Delta\phi$ is the difference in ϕ position between the two segments. Otherwise, the direction of the highest quality segment is used.

The segment in a GEM system is be combined in the CSC algoritm: pair of segments in GEM and first CSC station or in GEM and second CSC station are considered in order to measure the difference in ϕ position between the two segments.

This algorithm is used for the off-line seeding and can also be used in the High-Level Trigger (HLT) chain as an intermediate step between L1 and L2.

6.3.3.2 Pattern Recognition

6.3.4 Regional reconstruction: Standalone muon (Anna,Archie)

The standalone/Level-2 muon reconstruction uses only data from the muon detectors. Both tracking detectors (DT, CSC and GEM) and RPCs participate in the reconstruction. Despite the coarser spatial resolution, the RPCs complement the tracking chambers, especially where the geometrical coverage is problematic, mostly in the barrel-endcap overlap region. The reconstruction starts with the track segments from the muon chambers obtained by the local reconstruction. The state vectors (track position, momentum, and direction) associated with the segments found in the innermost chambers are used to seed the muon trajectories, working from inside out, using the Kalman-filter technique. The predicted state vector at the next measurement surface is compared with existing measurements and updated accordingly. In the barrel DT chambers, reconstructed track segments are used in the Kalman filter procedure while, in the endcap CSC chambers, the individual reconstructed constituents (three-dimensional hits) of the segments are used instead. Reconstructed hits from the GEM and RPC chambers are also included. A suitable χ^2 cut is applied in order to reject bad hits, mostly due to showering, delta rays and pair production. In case no matching hits (or segments) are found, e.g. due to detector inefficiencies, geometrical cracks, or hard showering, the search is continued in the next station. The state is propagated from one station to the next using specific software, which takes into account the muon energy loss in the material, the effect of multiple scattering, and the nonuniform magnetic field in the muon system. The track parameters and the corresponding errors are updated at each step. The procedure is iterated until the outermost measurement surface of the muon system is reached. A backward Kalman filter is then applied, working from outside in, and the track parameters are defined at the innermost muon station. Finally, the track is extrapolated to the nominal interaction point (defined by the beamspot size) and a vertex-constrained fit to the track parameters is performed.

6.3.5 Global Muon Reconstruction (Anna,Cesare)

The global/Level-3 muon reconstruction consists in extending the muon trajectories to include hits in the silicon tracker (silicon strip and silicon pixel detectors). Starting from a standalone reconstructed muon, the muon trajectory is extrapolated from the innermost muon station to the outer tracker surface, taking into account the muon energy loss in the material and the effect of multiple scattering. Silicon layers compatible with the muon trajectory are then determined, and a region of interest within them is defined in which to perform regional track reconstruction. The determination of the region of interest is based on the track parameters and their corresponding uncertainties of the extrapolated muon trajectory, obtained with the assumption that the muon originates from the interaction point.

Inside the region of interest, initial candidates for the muon trajectory (regional seeds) are built from pairs of reconstructed hits. The 2 hits forming a seed must come from 2 different tracker layers, and all combinations of compatible pixel and double-sided silicon strip layers are used in order to achieve high efficiency. In addition, a relaxed beam-spot constraint is applied to track candidates above a given transverse momentum threshold to obtain initial trajectory parameters. Starting from the regional seeds, a track-reconstruction algorithm, based on the Kalman-filter technique, is used to reconstruct tracks inside the selected region of interest. The track-reconstruction algorithm consists of the following steps:

- **trajectory building (seeded pattern recognition):** the trajectory builder transforms each seed into a set of trajectories. Starting from the innermost layer, the trajectory is propagated to the next tracker reachable layer, and updated with compatible measurements found on that layer;
- **trajectory cleaning (resolution of ambiguities):** the trajectory cleaner resolves ambiguities between multiple trajectories that may result from a single seed on the basis of the number of hits and the χ^2 of the track fit;
- **trajectory smoothing (final fit):** all reconstructed tracks are fitted once again, without a beam-spot constraint, using the hits in the muon chambers from the original standalone reconstruction together with the hits in the silicon tracker. To resolve possible ambiguities a second cleaning step is performed which selects the final muon candidates on the basis of a χ^2 cut.

The selected trajectories are then refitted excluding measurements (hits or segments) with high χ^2 values in muon stations with high hit occupancy. In addition the trajectories are refitted using only silicon tracker hits plus hits in the innermost muon station (excluding RPC hits?) and the χ^2 probability of the fit is compared with the χ^2 probability of the tracker-only trajectory in order to detect muon bremsstrahlung or any kind of significant energy loss of the muon before the first muon station. This procedure is important for the accurate momentum reconstruction of very high-p_T (TeV) muons. The precise reconstruction of these objects is very challenging because of catastrophic energy loss and severe electromagnetic showers in the muon system.

6.3.6 Muon identification

Particles detected as muons are produced in pp collision from different sources which lead to different experimental signatures:

- **Prompt muons:** the majority of muon chamber hits associated with the reconstructed muon candidate were produced by a muon, arising either from decays of W, Z, and promptly produced quarkonia states, or other sources such as Drell-Yan processes or top quark production.
- **Muons from heavy flavour:** most of muon chamber hits associated to the muon candidate were produced by a true muon. The muon's parent particle can be a beauty or charmed meson, a tau lepton.
- **Muons from light flavour:** most of muon chamber hits associated to the muon candidate were produced by a true muon. This muon originated from light hadron decays (π and K) or, less frequently, from a calorimeter shower or a product of a nuclear interaction in the detector.
- **Hadron punch-through:** most of muon chamber hits of the muon candidate were produced by a particle other than a muon. The so called "punch-through" (i.e. hadron shower remnants penetrating through the calorimeters and reaching the muon system) is the source of the most of these candidates ($\sim$ 88% for Global Muons) although "sail-through" (i.e. particles that does not undergo nuclear interactions upstream of the muon system) is present as well.
- **Duplicate:** if one particle gives rise to more than one reconstructed muon candidate, the one with the largest number of matched hits is flagged according to one of the other categories. Any others are labelled as "duplicate". These are duplicate candidates created by instrumental effects or slight imperfections in the pattern recognition algorithm of the reconstruction software.

The standard CMS reconstruction provides additional information for each muon, useful for muon quality selection and identification (ID) in physics analyses.

- A muon is required to be identified both as a tracker (TRK) and a global muon (GLB). This is effective against decays-in-flight, punch-through and accidental matching (with noisy or background tracks or segments).
- The number of hits in the tracker track part of the muon. Generally tracks with small number of hits give bad p_T estimate. In addition decays in flight give rise in many cases to lower hit occupancy in the tracks.
- There should be at least one pixel hit in the tracker track part of the muon. The innermost part of the tracker is an important handle to discard non-prompt muons. By requiring just a minimal number of hits we introduce negligible reconstruction inefficiency.
- A minimal number of tracker layers involved in the measurements. This guarantees a good p_T measurement, for which some minimal number of measurement points in the tracker is needed. It also suppresses muons from decays in flight.
- The muon track has to have a minimum number of chamber hits in different stations with "matching" (consistent with the propagated to the muon chambers tracker track) segments. This is also to comply with a similar looser requirement in the trigger.
- Very bad fits are rejected by requiring reasonable global muon fit quality. If there is a decay in flight inside the tracking volume, the trajectory could contain a sizeable "kink", resulting in a poorer χ^2 of the fit used to determine the trajectory.
- The global muon has to contain at least one "valid" muon hit. This requirement assures that the global muon is not a "bad" match between the information from the muon system and the tracker. This could happen in particular for non-prompt muons.
- The impact parameter (d_{xy}), defined as the distance of closest approach of the muon track with respect to the beamspot has to be compatible with the interaction point hypothesis (muon from the interaction point). This is effective against cosmic background and further suppress muons from decays in flight.
- Also the longitudinal impact parameter (d_z) is used to further suppress cosmic muons, muons from decays in flight and tracks from pile-up.
- Muon can be required also to be matched a particle flow muon.

6.4 Performance (Anna, Cesare, Raffaella, Archie)

The muon reconstruction algorithms have been described in Section 6.3 and the performance of these algorithms has been evaluated using the full detector simulation with a magnetic field of 3.8 Tesla. In addition the performance of reconstruction in the inner tracker alone is determined since such tracks are fundamental for global muon reconstruction.

The performance has been evaluated using samples of muon gun samples (two muons per event, one per hemisphere) generated with different values of p_T and flat distributions in η and ϕ (Table 6.2) using CMSSW_6_2_0_SLCH3.

Using these samples we have measured the efficiencies, the resolutions and the pulls of the track parameters. In this analysis in order to match the simulated muon with the reconstructed

Table 6.2: Samples used for the study of the muon reconstruction performance ($0.90 < |\eta| < 2.45$ and $-\pi < \phi < +\pi$).

Transverse Momentum (GeV/c)	Number of events
5	200000
10	200000
50	200000
100	200000
200	200000
500	200000
1000	200000

track, a cone criterion has been used, $\Delta R = sqrt(\Delta\phi)^2 + (\Delta\eta)^2$ as well as an association algorithm which matches simulated hits and reconstructed hits. Only the cases in which the matching between reconstructed tracks and muon simulated tracks is one to one are considered in the eta region covered by GE1/1. The single particle generated events include also the anti-particle in order to study reconstruction of particles with different charges. No charge dependant differences were observed. In the following analysis, therefore, no distinction is made between the two charges and all quantities are determined using the full samples.

6.4.1 Local Muon Reconstruction: GEM spatial resolution

In order to study the GEM subsystem resolution, the residuals and pulls of the GEM recHit local coordinate x and global coordinate ϕ are studied in this section. In general the pull of a variable a is defined as:

$$Pull = \frac{a^{rec} - a^{gen}}{\sigma_a}. \tag{6.3}$$

For a normally distributed variable a the pull distributions are Gaussian with null mean value and unit variance. Deviation from unit indicates incorrectly estimated uncertainties. More precisely, if $\sigma_{pull} < 1$ the error is overestimated, while $\sigma_{pull} > 1$ means the error is under-estimated. Figure 6.1 shows the recHit x residual and pull distributions. The RMS of the x residual is expected to be compatible with the expected GEM resolution, in this case the obtained value is higher because of the strip orientation in the local system that produces a Δx up to $\sim$0.5 cm.

In order to understand if the recHit resolution is compatible with the expected GEM resolution, we have then looked at the ϕ residual distribution shown in Figure 6.2. The RMS of the distribution is compatible with the expected value calculated as $\Delta\phi_{strip}/\sqrt{12}$, where $\Delta\phi_{strip} = 10^\circ \times CLS/384$ and CLS is the mean cluster size obtained from the test beams ($\sim$ 1.4 strips).

6.4.2 Global Reconstruction: Efficiencies

For the stand-alone and global reconstruction we have studied the fraction of reconstructed tracks that make use of at least one GEM recHit. Therefore the numerator and denominator in the efficiency calculation are defined as follows:

Numerator: Number of stand-alone or global muon tracks with at least one GEM recHit used in the track fitting matched to a muon simulated track in $1.64 < |\eta| < 2.1$

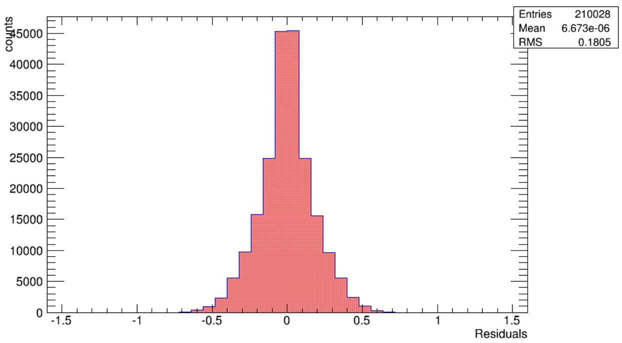

(a) Residual distribution.

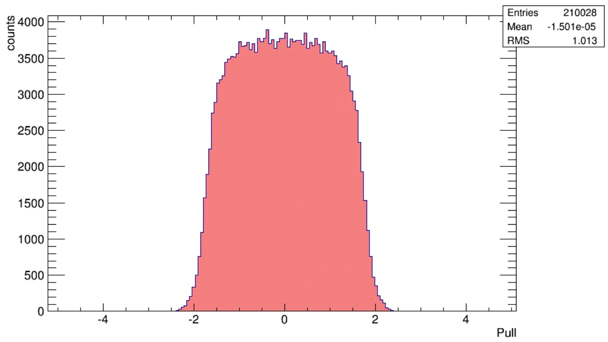

(b) Pull distribution.

Figure 6.1: RecHit x residual (a) and pull (b) distributions.

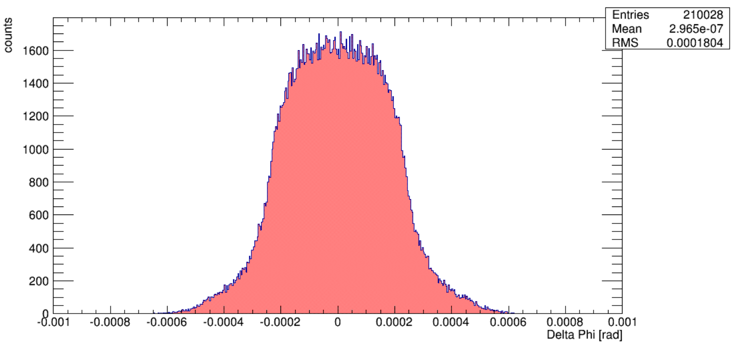

Figure 6.2: $\Delta\phi$ distribution for a muon GEM recHit that mached with simHit in events with only one muon simHit per roll.

Denominator: Total number of stand-alone or global muon tracks (i.e. GEM recHits can be used or not) matched to a muon simulated track in $1.64 < |\eta| < 2.1$

We have plotted the efficiencies as a function of the simulated p_T, η and ϕ and the results are shown in Figure 6.3. The plots assure that the GEM recHits are correctly used in the track fitting and that we are full efficient, that is almost all the tracks folling in the eta region of interest make use of at least one GEM recHit.

6.4.3 Global Reconstruction: Resolutions and Charge Misidentification

In this section we analyse the track resolutions and the charge misidentification probability when the GEM recHits are used in the track fitting compared to the standard reconstruction.

The resolution, q/p_T, is the variable of interest because it is, locally, directly proportional to the curvature in the bending plane, which is what is measured by the tracking system. Moreover q/p_T is more suitable than p_T because it distributes normally around the true value. The resolution on this parameter is defined as the Gaussian width of:

$$\frac{\delta(\frac{q}{p_T})}{\frac{q}{p_T}} = \frac{q^{Rec}/p_T^{Rec} - q^{Sim}/p_T^{Sim}}{q^{Sim}/p_T^{Sim}}, \tag{6.4}$$

where q is the charge and p_T^{Sim} and p_T^{Rec} are the simulated and reconstructed transverse momenta, respectively. The values of q/p_T are obtained by fitting the q/p_T distribution to the $mean \pm 2 \times RMS$, while its errors is obtained from a difference to the fits on the core and a wider range to take into account the tails of the distribution. Another interesting quantity to look at is the RMS of the q/p_T distribution in order to understand the effect of the GEM subsystem over the core width but also on the tails where the majority of the badly reconstructed tracks are. Both quantities are shown as a function of the simulated p_T and η for the stand-alone and global reconstruction in Figure 6.4.

The charge misidentification probability is defines as the number of reconstructed muon tracks (matched to a simulated muon track) in the GEM eta region with wrong charge assigment, i.e. $q^{Rec} \times q^{Sim} < 0$, over the total number of reconstructed muon tracks (matched to a simulated muon track) in the GEM eta region. Also this quantity is useful in order to understand the impact of GEMs on one of the track parameters. The results for both the stand-alone and global reconstruction are shown as a function of the simulated p_T and η in Figure 6.5.

6.4.3.1 TeVmuon, TrackerMuon and recoMuon

6.5 Radiation background in the muon stations (Silvia Costantini)

FIXME: the new FLUKA geometry with improved shielding has been released only on June 6th therefore we still need to compare and validate the flux values Plots and tables will be updated in the next days.

Background radiation levels in the GE1/1 region of interest are an important consideration in the design of the Muon system upgrade. Low-energy gamma rays and neutrons are expected to contribute to up to 99% of the radiation background [?]. Together with low momentum primary and secondary muons, punch- through hadrons, and with LHC beam-induced

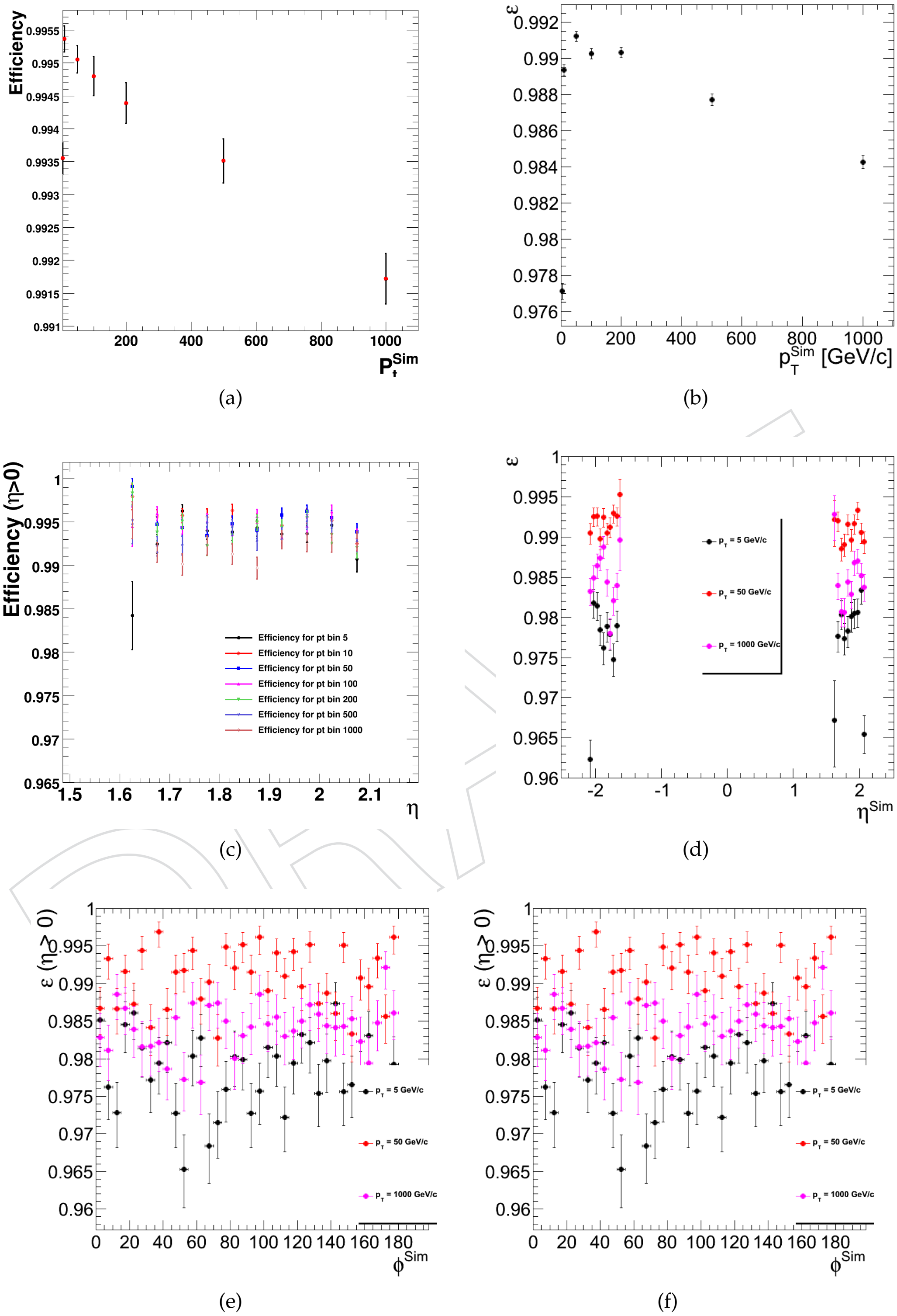

Figure 6.3: Efficiencies as a function of the simulated p_T, η and ϕ for the stand-alone (left column) and global reconstruction (right column).

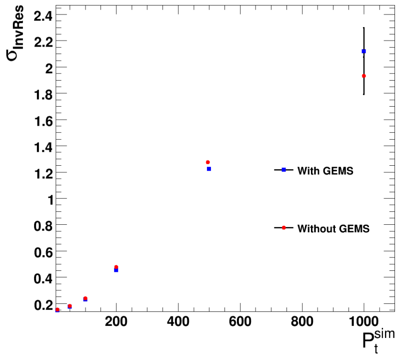

(a)

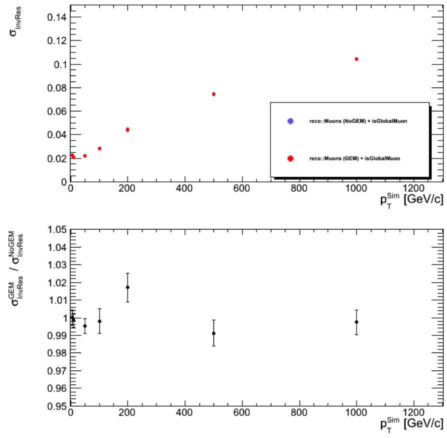

(b)

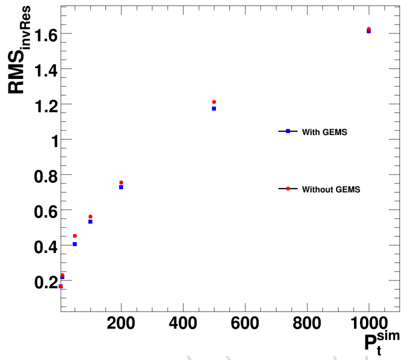

(c)

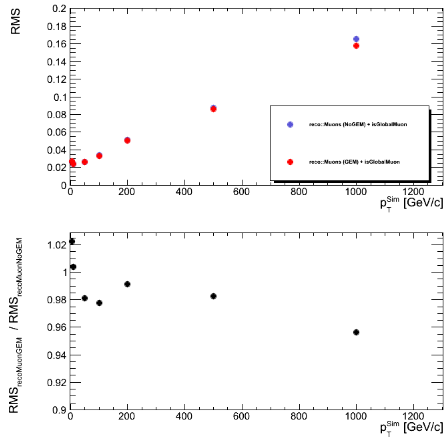

(d)

Figure 6.4: q/p_T resolutions and RMS as a function of the simulated p_T and η for the stand-alone (plots on the left) and global reconstruction (plots on the right).

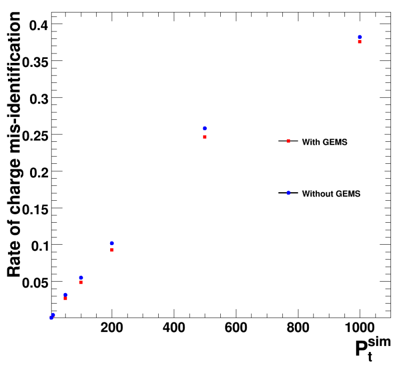

(a)

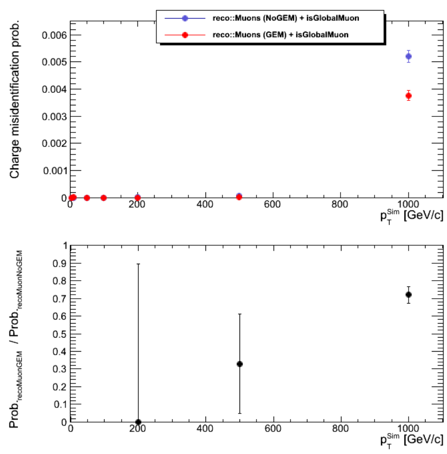

(b)

Figure 6.5: Charge misidentification probability as a function of the simulated p_T and η for the stand-alone (left column) and global reconstruction (right column).

backgrounds (primary and secondary particles produced in the interaction of the beams with collimators, residual gas, and beam pipe components), the background rate could exceed the detector rate capability and could affect the muon trigger performance. In addition, excessive radiation levels can cause aging of the detectors. The expected rate needs therefore to be carefully studied.

The expected background rate discussed in this Section is mainly estimated from FLUKA [**?**] simulation studies. The simulation was validated through accurate comparison with the data collected by the CSCc and RPCc from 2010 to 2012 [**?**] (etc.). Extrapolations of the existing CSC and RPC measurements to higher values of the LHC instantaneous luminosity have given compatible results, in the regions covered by those subdetectors.

Typical flux values are shown in Table 6.3 for a centre-of-mass energy $\sqrt{s} = 14$ TeV, corresponding to a total inelastic cross section of 80 mb [**?**], and for values of the LHC instantaneous luminosities equal to 10^{34} cm^{-2} s^{-1} or 10^{35} cm^{-2} s^{-1}. Flux values corresponding to other luminosities can be obtained by linearly rescaling the values shown in the Tables. This is justified by the fact that a linear relationship between the measured rate and the instantaneous luminosity has been observed in the 2010-2012 data over several order of magnitudes, from 10^{29} cm^{-2} s^{-1} to $0.7 \cdot 10^{34}$ cm^{-2} s^{-1}.

The total flux expected from all particles is shown in the first row of Table 6.3, followed by the flux due to neutrons only, photons only, and charged particles only.

Table 6.3: Expected flux values in the GE1/1 region of interest. The (R,z) coordinates where the flux is evaluated and the particle type are given.

Particle type	R (cm)	z (cm)	Flux (cm^{-2} s^{-1}) for $\mathcal{L} = 10^{34}$ cm^{-2} s^{-1}	Flux (cm^{-2} s^{-1}) for $\mathcal{L} = 10^{35}$ cm^{-2} s^{-1}	Flux uncertainty (%) (%)
All	150	560	$1.4 \cdot 10^4$	$1.4 \cdot 10^5$	10%
All	180	560	$8.3 \cdot 10^3$	$8.3 \cdot 10^4$	12%
All	250	560	$1.4 \cdot 10^3$	$1.4 \cdot 10^4$	22%
Neutrons	180	560	$5.6 \cdot 10^3$	$5.6 \cdot 10^4$	12%
Photons	180	560	$2.5 \cdot 10^3$	$2.5 \cdot 10^4$	20%
Charged	180	560	$1.2 \cdot 10^2$	$1.2 \cdot 10^3$	40%

Typical average rates at $\mathcal{L} = 5 \cdot 10^{34}$ cm^{-2} s^{-1} are expected not to exceed a few hundreds Hz/cm^{-2} and are therefore well within the GEM rate capability.

6.5.1 GEM sensitivities to neutrons and photons

Preliminary version

GEM sensitivities 6.5.1 to neutrons, photons, and charged particles have been determined with Geant4 [**?**] as the number of "signals" over the total number of particles hitting the detector. A valid signal is assumed to be produced if at least one charged particle reaches the transfer or the first drift gap, which gives an upper limit to the sensitivity.

BaclgroundFigs/GE11_sensitivity_beam_front.png

Figure 6.6: GE1/1 sensitivities to neutrons, photons, electrons, and positrons, as a function of the particle energy, for a perpendicular beam coming from the front of the chamber.

FIXME add comparison with test beam results

6.5.2 Energy spectra of neutrons and photons

6.6 Particle fluxes in the muon chambers (KH, Archie Sharma)

On top of the radiation background, discussed in the previous section, charged particle tracks from pile-up (PU) and punch-through will contribute additional flux. Those charged particles rates (muons, jets) depend on the luminosity and pile-up and increase strongly beyond eta>1.6. While the ratio of PV muons / PU muons, was about 1:1 in 2012 (8 TeV, 50 ns), it will increase by one order of magnitude to 1:10 (14 TeV, 50ns).

Fig. XXX shows the fraction of muons as a function of eta for three different PU scenarios. A similar behavior could be shown for jets. The triggering aspect of this high backgrounds in discussed in SEC TRIGGER. Even if triggered in a clean fashion, muon tracking has to operate, as was shown in SEC DPG PERFORMANCE.

6.7 Muon performance measurements (Anna)

This section summarizes the performance for CSC+GEM in the region $1.5< |\eta| <2.2$

For muons with pT<200 GeV- which is the momentum range of Higgs, SM and other ongoing physics - the stand-alone muon resolution improves (RMS) from 62% to 58%. **FIXME: show plot from Slava**

6.8 Muon trigger performance (?)

Presumably this section will discuss the performance of the combined CSC+GEM trigger. Also technicalities of implementation.

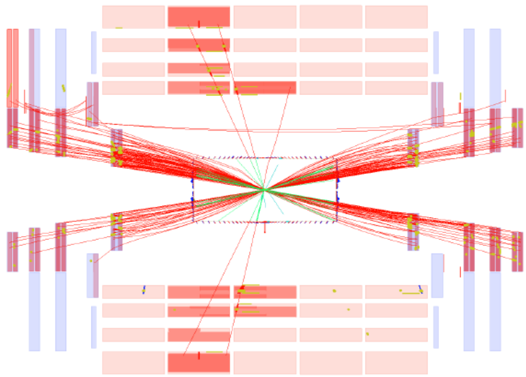

Figure 6.7: Illustrating the high-rate environment in the forward region. LOW QUALITY, PLACEHOLDER PLOTS

Where do we put the plots of impact of lowering the trigger threshold on H2Tau? Proposal: physics section

6.9 Performance for representative physics processes (Kerstin and Paolo)

Muon ID and quality selection steps are very similar to the present analyses, except the required muon isolation which had to be tuned for higher PU. SHOULD WE SHOW A PLOT FOR THE TUNE? The Muon selection uses: p_T >20 GeV, tight PF Muon ID, $|d0|$ <0.02 cm, $|dz|$ <0.2 cm. The modified/tuned isolation is: PF relative isolation ($\Delta\beta$ correction) is below 0.15 (PU35) and below 0.25 (PU50).

GE1/1 in the high-rate forward region

For analyses such as Z$\rightarrow 2\mu$, H$\rightarrow 4\mu$ and H$\rightarrow 2\tau$ all final state muons need to be reconstructed for the full kinematic event reconstruction. These channels yield muons with p_T's typically up to O(50) GeV, an example of which is shown in Fig. 6.8 for muons from H$\rightarrow 2\tau$. For all these channels about 20% of the events have at least one muon in the GE1/1 instrumented region. More precisely for $1.5 < \eta < 2.2$ 18% of the Z$\rightarrow 2\mu$ (p_T >15 GeV) events, 27% of the H$\rightarrow 4\mu$ (p_T >5 GeV) events and 23% of the H$\rightarrow 2\tau$ events (nearly independent of p_T). Note that this is a difficult region because of B-field and increasing background (see plot with no.muons as fct of eta). If we lose a CSC in that region, events are lost. Any broken CSC or chamber with a reduced efficiency can be recovered by GE1/1 (see plots). The present H$\rightarrow 2\tau$ analysis only uses the acceptance up to $|\eta|$ 2.1 to avoid the high fraction of misreconstructed muons between $2.1 < |\eta| < 2.4$. Extending it to 2.4 would only yield a modest 7% higher acceptance based on GE1/1. In H$\rightarrow 4\mu$ the four muons cover a rather wide p_T range, from 5 GeV to as high as 60 GeV, as can be seen on Fig. 6.8.

The GE1/1 region is presently only instrumented with CSCs and a reduced efficiency of any of these chambers could yield a loss of the event, particularly important for channels with a small cross section and/or a small signal selection efficiency. As an example, if the CSC local efficiency is reduced to 95%, an additional GE1/1 will recover this 5% and provide nearly 100% detection efficiency. This affects 27% of all H$\rightarrow 4\mu$ events (see Fig. 6.9).

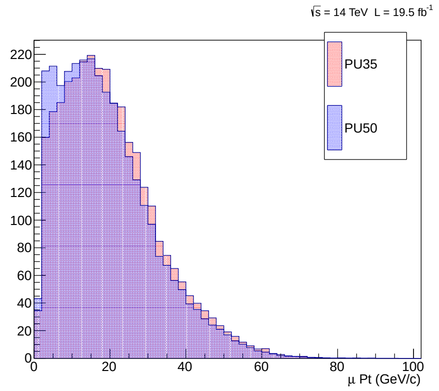

Figure 6.8: Left: average p_T of muons in H→ 2τ → μ for two PU scenarious. These muons are pretty soft. Right: p_T distribution of the 4 muons from H→ 4μ events. PLACEHOLDER PLOTS

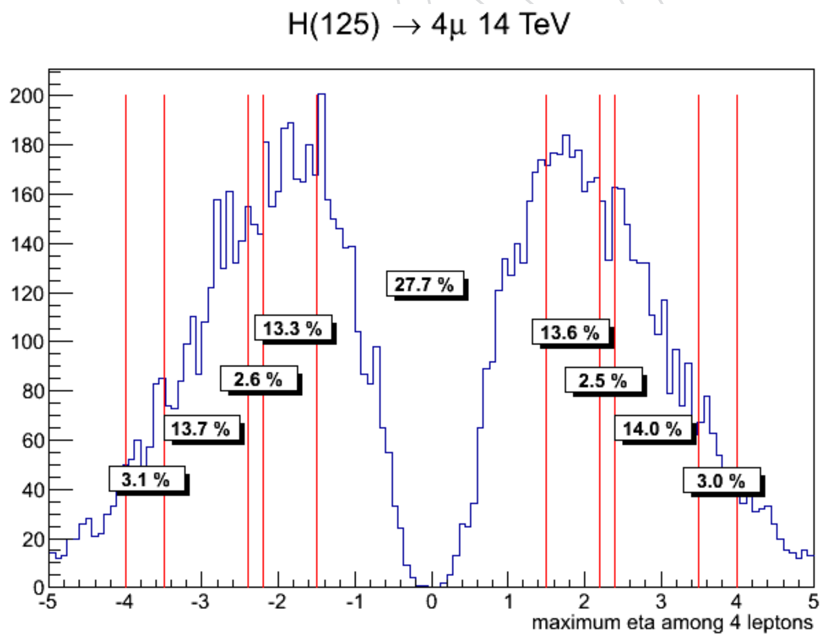

Figure 6.9: Distribution of the highest η muon from H→ 4μ. PLACEHOLDER PLOTS

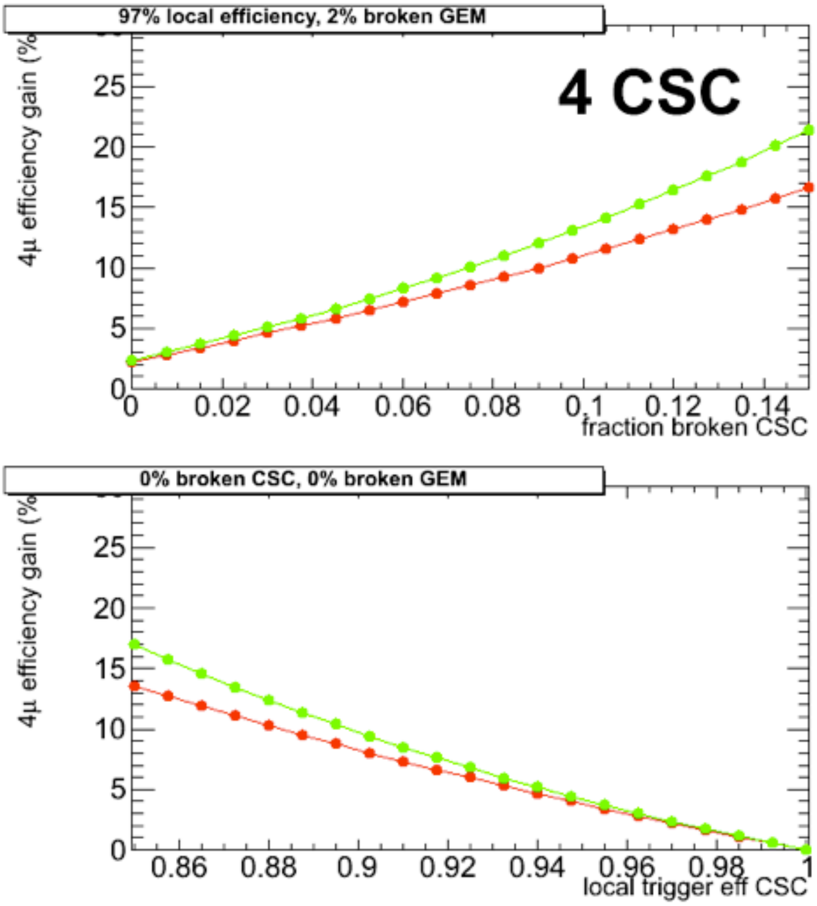

Figure 6.10: Redundancy. PLACEHOLDER PLOTS

Lowering the trigger threshold

H→ 2τ is an important channel probing the Higgs coupling to the third family. From the various tau decay channels, the relevant here are the channels where one or both tau leptons decay to a muon with 16% BR. Such muons are very soft as shown in Fig. 6.8-left. Triggering H→ 2τ events can either be achieved with a hadronic di-tau (jet) signature, (high BR but relatively high threshold), or based on the lepton from the leptonic tau decay. For the latter, muons provide a clean signal although a soft momentum spectrum thus low trigger thresholds. The fraction of selected H2Tau signal events as a function of eta for different trigger thresholds is shown in Fig. 6.11. The overall selection efficiency is less than 1%. The overall number of reconstructed events increases by about 20% when lowering the trigger threshold by 5%. With the anticipated muon trigger threshold (single or double) of 20 GeV 3000 evts would be selected. This number would increase to 4000(5000) or by 20(40)% if the treshold could be lowered to 15(10) GeV.

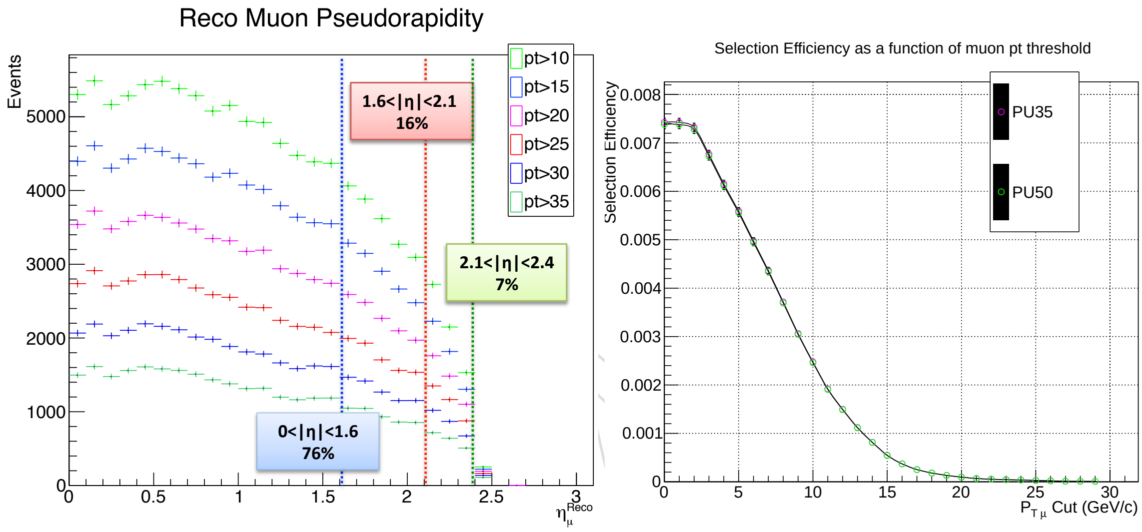

Figure 6.11: The H→ $2\tau \to \mu$ channel. Left the fraction of events as a function of eta. About 7% of the events could be used with the phase-1 detector but are not included in the present analysis due to the high fraction of misreconstruction in the region 2.1-2.4. Right: IS PROBABLY THE BETTER PLOT shows the gain in selection efficiency as a function of the trigger threshold. Make this for 300/fb. PLACEHOLDER PLOTS

6.10 Track-based Detector Alignment Performance (?)

Chapter 7

Integration, Installation and Commissioning in CMS

Editors: H. Hoorani, A. Lanaro, A. Marinov, M. Tytgat

7.1 Introduction

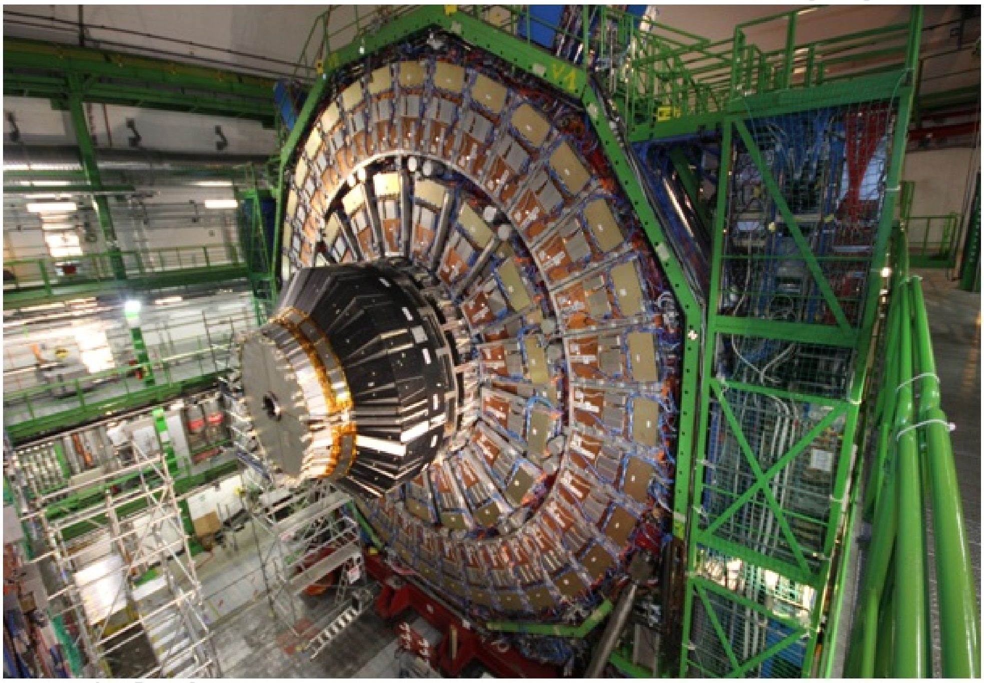

Figure 7.1: General view of the YE-1 endcap

The high eta part of CMS is shown in fig. 7.1, where we have a picture of the YE1 endcap part. The dark part of the endcap is the nose which is physically the region of interest to install the new muon detector to cover the η region $1.6 < |\eta| < 2.1$. At the present moment this zone is vacant and only CSC - ME1 is located there as the only muon detector. The present thesis is focused on the option of using a GEM based detectors which can be instrumented and installed in this zone.

7.2 Mechanical aspects and Alignment

Output from the Alignment group is under discussion.

7.2.1 Description of the GE1/1 Location

In Fig. 7.2 is shown the quarter cut of the CMS detector. There in details is shown the location of the GE1/1 zone, which sites just in front of the ME1/1 detectors. The GE1/1 are mounted on the side of the back-flange which is located 5674 mm away from the interaction point. Mechanically there is no solid attachment to the CSC chambers. The back-flange is made of non magnetic stainless steel transparent for the magnetic forces. This puts the GE1/1s in good favor where the expected excursion of the chambers due to the CMS magnetic filed is foreseen to be only in Z direction with couple of millimeters.

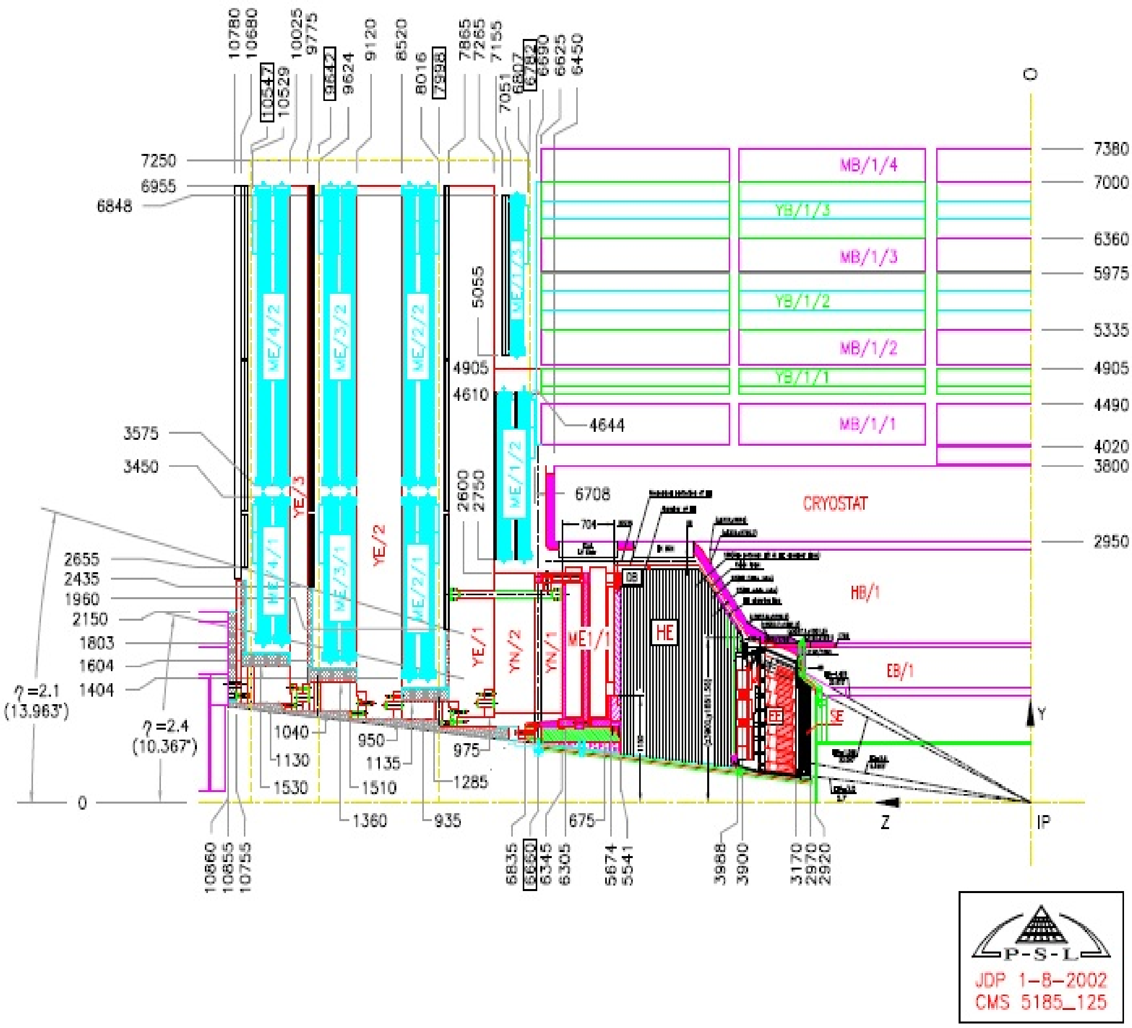

Figure 7.2: Quarter cut of the CMS detector. The GE1/1 super-chambers will be installed on the back-flange on 5674 mm away from the interaction point.

General view of the GE1/1 installation slots is shown in fig. 7.3. In the figure we can see the ME1/1 detectors placed in their positions as well as their blue LV cables. The small pockets between the black covers of the nose and the ME1/1s are physically the installation slots for the GE1/1 super-chambers. As it is shown in the figure the only one accessible zones of the GEM detectors will be their patch-panels.

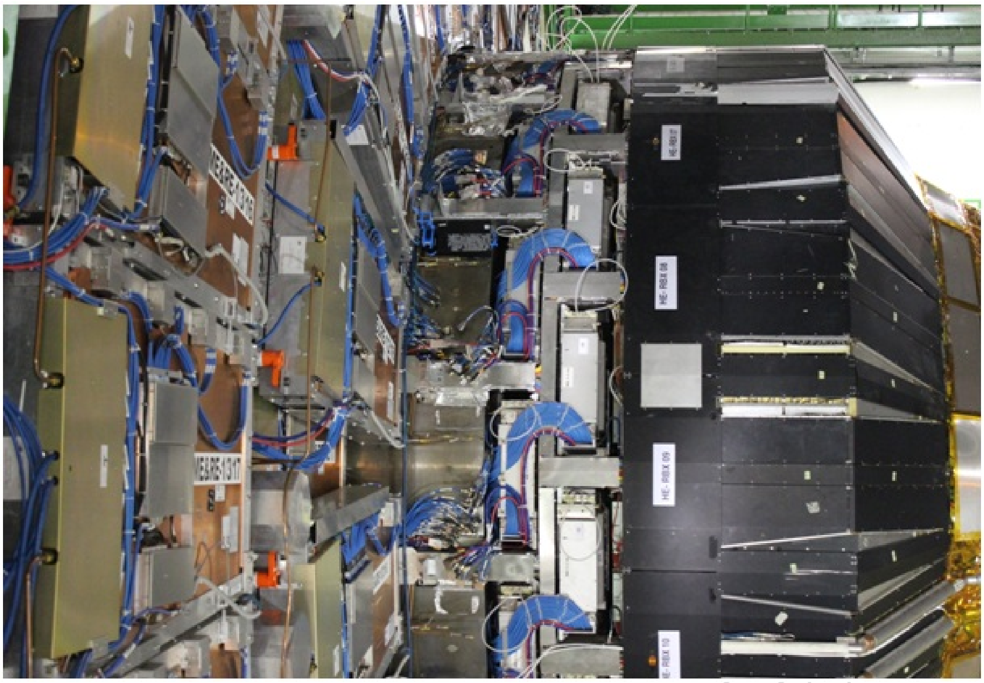

Figure 7.3: General view of the GE1/1 Installation slots

7.2.2 Installation Procedures and Tools

Rails, Palonier etc.

7.2.3 Position Monitoring

7.2.4 Alignment

7.2.4.1 Introduction

The GE detector on each side of CMS can be considered as a double-layer disk (GE-disk) formed by 36 super-chambers mounted on the back-plane of the HE calorimeter. The knowlwdge of the chamber positions in the CMS coordinate system is splitted to two tasks: the positions of the chambers in the coordinate system of the GE-disk and the location of the entire disk in CMS. The chambers themselves can be considered as rigid bodies.

The requirements for precision of the chamber positioning in the GE-disk are not identical for the six degrees of freedom. The most demanding directions are the R*phi and R requiring the knowledge of position with $\sim$100 micrometer accuracy while in the other directions the mm-range installation accuracy is enough.

The initial position of the whole GE-disk after closure will change and also its deformation (displacement of the chambers with respect to each other) cannot be excluded due to magnetic field and thermal effects so the requirements to define the position of the GE-disk in CMS are the same as for the chambers inside the GE-disk.

7.2.4.2 Alignment concept

Different methods to solve the task of alignment are already used in CMS for other subsystems ([?],[?]). This experience has been used to work out the concept for the GE-chambers.

As the readout strips that are relevant for the alignment cannot be observed aflter the assembly

Figure 7.4: General view of the CMS back-flange

of the chambers the first step is to transfer the strip positions to special fiducial elements on the outside of the chamber body during the construction. These fiducial elements can be monitored at the installation and during the running period. Two types of elements are planned to be used: removable survey targets and capacitive sensors. The survey targets help to locate the chambers with moderate ($\sim$mm) precision during the installation. The capacitive sensors measure the R-phi and the R distances between the adjacent chambers and capable to define the chamber positions in the GE-disk coordinate system with the required precision. Finally, track-based alignment methods can define the entire GE-disk in the CMS coordinate system, crosscheck the results of the HW-alignment system and further improve the precision of the alignment.

This concept based on three different, independent and complementary methods can guarantee the precise and robust solution of the alignment task.

7.2.4.3 Strip position transfer to the outer side

The production technology of the readput boards cannot the positioning of fiducial marks on the opposite (to the strips) side precisely enough (within 20 micron) related to the strips we plan to establish the precise connection using the via holes. This can be made by full mapping of both sides of the readout board at CERN before the GEM-assembly by a 2D scanning table (made or purchased).

The 2D scan -besides the alignment needs- is opening a possibility to check the board quality and also to detect and measure their possible differences.

7.2.4.4 Capacitive sensors

The sensor measures the capacitance between two parts, the tranducer and the target. The transducer will be mounted (glued) on the readout board and the grounded surface of the frame on the chamber periphery will be used as target. The transducer is connected to the frontend via single thin coaxial cable that can be as long as 10-20m allowing us to put the electronics on the balcony racks. The dimension of the tranducer (10x10x50 mm^2) is occupying minimal space on the readout board.

Following the layout of the GE-disk the plan is to put transducers on the long chambers only: two on each phi-side and two in R-direction (Fig. 7.5). The total number of sensors planned to be used for the full project is 432 (6 per long chamber).

7.2.4.5 Location (calibration) of the alignment elements

After the installation the alignment elements and the chamber frames their positions have to be measured with respect to the outside fiducial marks on the outer side of the readout boards. This step is planned to be made by using CMM (Coordinate Measuring Machine) installed at CERN. All the measurements (together with the 2D scan results) are stored as calibration data and will be used during the position reconstruction of he chambers inside the GE-disk.

7.2.4.6 Technological steps during the construction - summary

The construction of the GE-alignment system can be summarised as follows:

Preparatory steps:

- Construction/purchase of the scanning table including the control/data software and its installation at CERN,

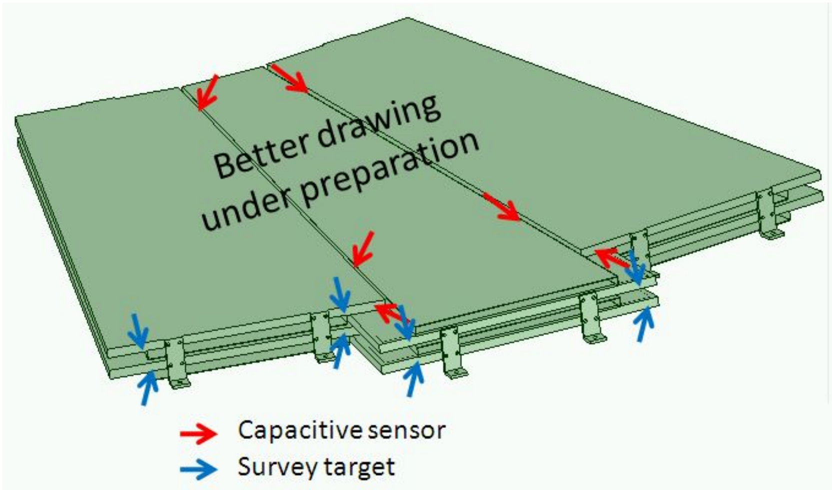

Figure 7.5: Locations of the transducers and survey targets.

- Purchase of the CMM machine and its installation at CERN,
- Production of the Survey target holders (288 oices + spare) and the Capacitive transducers (432 pieces + spare).

Construction steps:

- Full scan of both sides of the readout boards at CERN on the scanning table before the GEM-assembly,
- Installation (glueing) of the transducers on the ready GEM-chambers at CERN,
- Fixation of the frames on GEM-chambers,
- Measurement of the positioning elements and frame-surfaces by the CMM machine.

7.2.4.7 GE-alignment R&D

There are still areas for R&D work concerning the GE-alignment hardware system. The design of the capacitive transducer is in the prototype phase, the optimization of the geometry and the readout electronics, the noise as well as the radiation hardness and magnetic field questions are still to be studied. Considerable work is still required the pattern recognition program for the scanning table to ensure fast, reliable and precise data-evaluation. The simulation ofthe accuracy of the proposed system based on optogeometrical modelling is still under work. Finally, the development of the software package performing the position reconstruction from the calibrated and measured data is to be optimized.

7.3 Power System

7.3.1 HV Power System

7.3.1.1 Multi-channel HV powering system

It is Under development

7.3.1.2 Single-channel HV powering system

The general view of the single-channel HV powering configuration is shown in fig. 7.6. It represents a standart system adopted from other sub-detectors in CMS and it is based on commercial

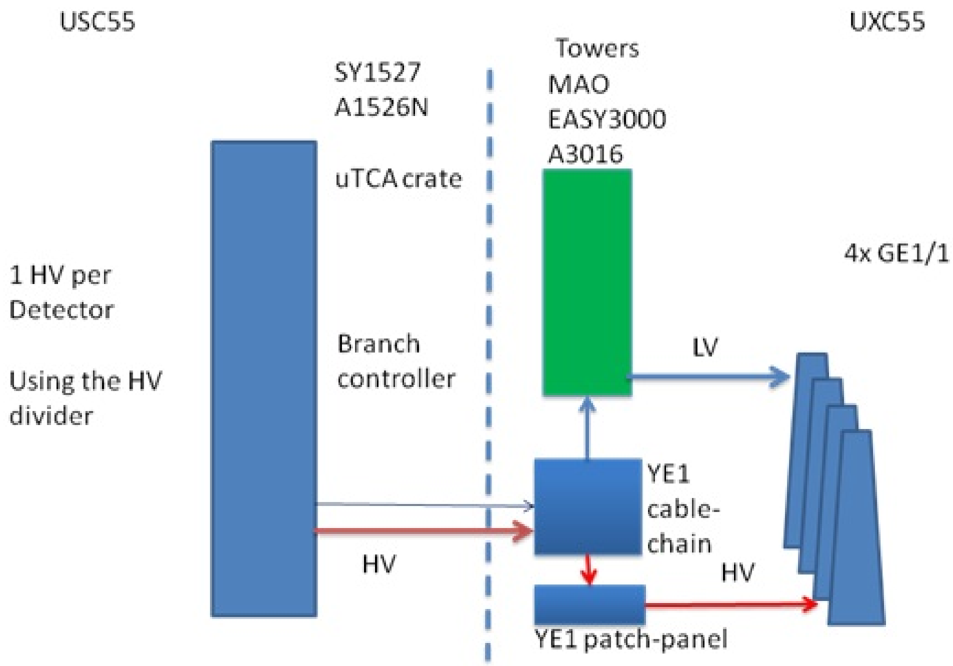

Figure 7.6: Diagram of the GE1/1 Powering configuration with single-channel HV system

modules from CAEN company. Here as it is shown we are deviding the system in to two parts. The USC one which is on the left and the UXC, the right. In the USC where is the service cavern of CMS will be placed the actual HV Power Supply modules A1526N . They are placed in a main frame crate SY1527. Each HV module can provide six output channels where the maximum current per channel is 1 mA at 15 kV. If GE1/1 HV powering system is one channel per super-chamber we need 72 HV channels for the total project. The usage of single-power HV system has the advantage that the HV cables of RE1/1 are already placed in the nose and can be used for the GE1/1s. To transport the HV currents from teh USC to the experimental cavern UXC is used long multi-core HV cable which goes from the bottom level of USC to the YE1 cable chains and reached the YE1 HV patch-panne located on the X1 near side.

7.3.2 LV Power System

7.4 Cabling

7.4.1 HV Cabling

Multi-core or single-core cabling

7.4.2 LV Cabling

7.5 Cable Routing

The general routing plan of all the cables for GE1.1 is shown in fig. 7.7. There as bold red line is shown the theoretical path of all the cables from the GE1/1 super-chambers, which are shown as orange rectangular and to the periphery of the YE1 disk. Here also is shown the routing on top of the ME1/2 and ME1/3 chambers where dismounting of these detectors will be not necessary.

The complicity in front of this project is the fact that all the cable trays inside the nose are

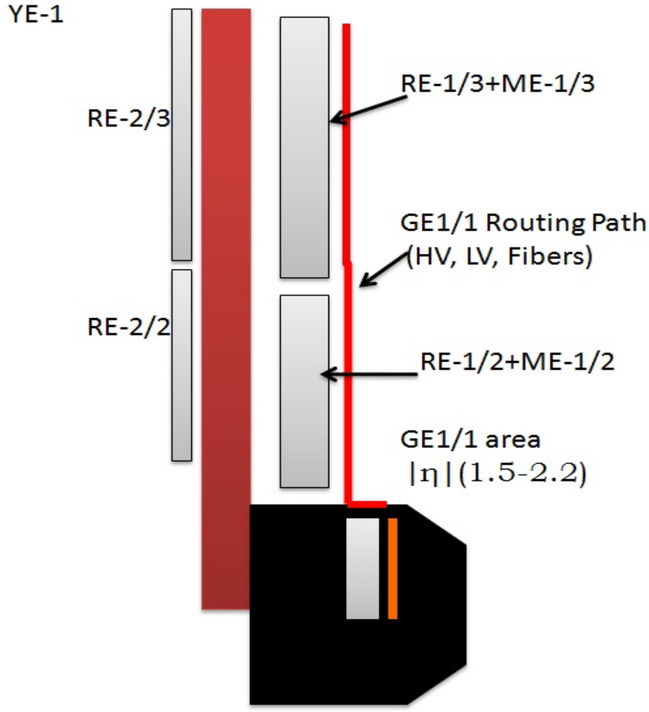

Figure 7.7: Diagram of the general cable routing in the nose and on the disk

already full with services for other sub-detectors. Based on this, a strategy to avoid the standard pats was developed. In fig. 7.8 is shown how is planned to route the cables inside the YE1 nose structure. This technique is valid only when all cables as LV, HV and fibers are placed inside flexible duct in order to secure and maintain the cable package volume. The GE1/1 Cables will follow the path of the ME1/1 cooling pipes which is marked in the figure as zig-zag blue dashed line. By this way the the necessity of using the nose cable trays is not any more valid. Simply will route our cables close to right side of the trays as we are looking it from the interaction point.

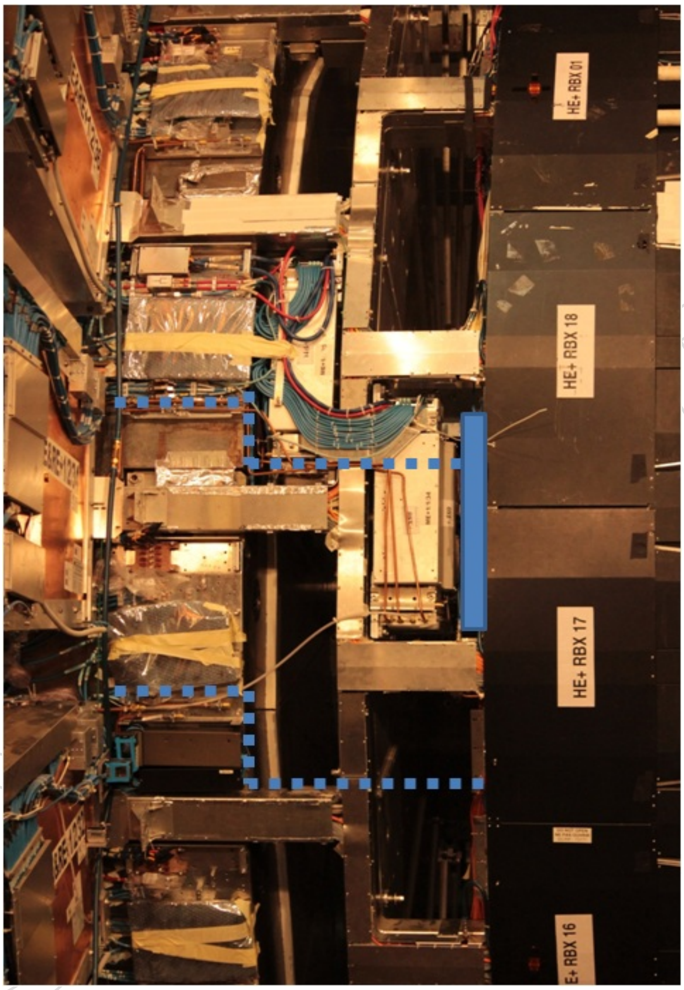

Figure 7.8: The cable routing inside the nose. The blue rectangular represents the GE1/1 patch-panel and the dashed lines, the cable path.

Fig. 7.9 shows the clearance available between the top of the small cable tray, placed in ϕ and the YE1 Nose covers. The represents the most critical point of the cable path inside the nose. In the picture is shown distance about 30 mm but for safety we are counting it 20 mm.

In fig. 7.10 is shown as steps the routing starting from right to the left picture. . The right one shows the ME1/1 and the Cu cooling pipe starting from the detector. Just in front, toward the interaction point, will be the GE1/1 super-chamber. In the middle picture is shown the overall path of the cable duct which will be exact as the Cu cooling pipe shin in the figure. On the left part is the breaking point which will go from the nose to the YE1 disk. On the disk part of the endcap the duct will be placed on top of ME1/2 and ME1/3 till the periphery of the disk where

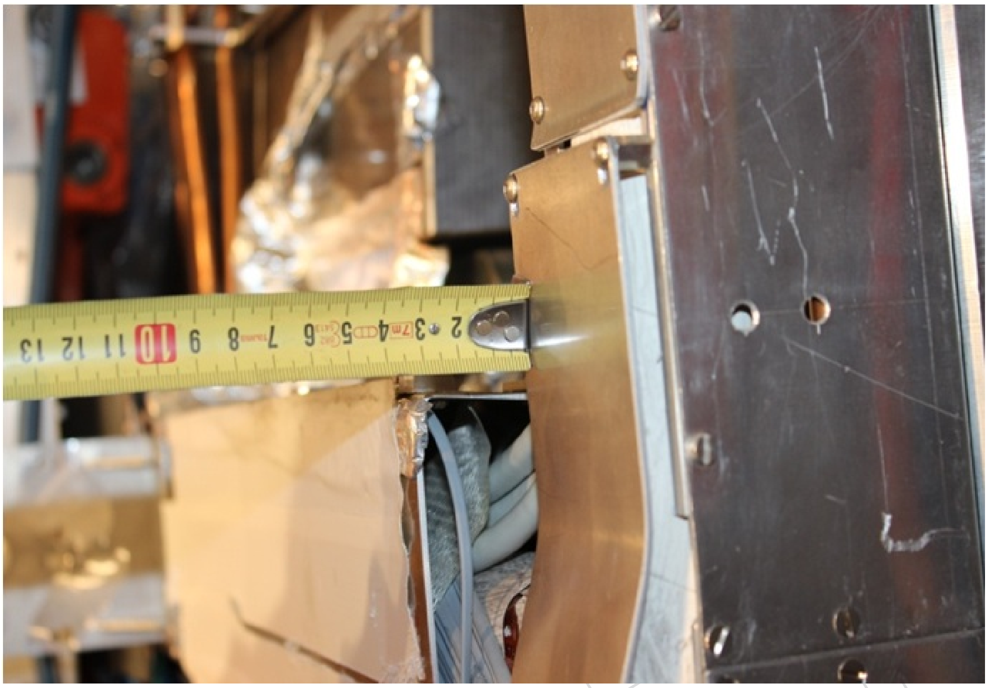

Figure 7.9: The maximum clearance available to place the cables from the CSC to the GE1/1 patch-panel.

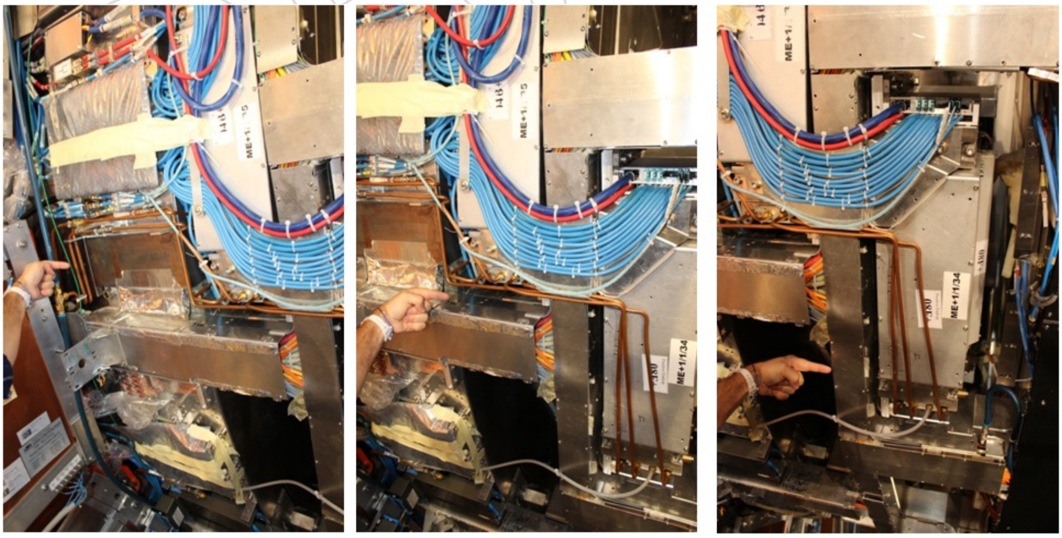

Figure 7.10: Showing the cable routing inside the nose from GE1/1 to the disk

the racks with the crates are located.

7.6 Readout and Control

7.6.1 Optical Links and Architecture

7.6.2 Radhard Optical Lines YE1

7.6.3 Fibers from UXC to USC

7.6.4 Commissioning

7.7 Gas System

The GE1/1 detectors are using a gas mixture of $ArCO_2CF_4$ $45 - 15 - 40\%$. It is similar to the CSC mixture, but with different fractions of the main gas compositions. The usage of Tetrafluoromethane (CF4) puts the demand of using only coper and stainless steel pipes in order to avoid the water absorption and the formation of hydrofluoric acid, which is very danger for the detector electrodes. The GE1/1 gas system partially is using the existing RE1/1 Gas infrastructure in particular the previously installed Cu pipes which runs between the GE1/1 installation zones and the gas distribution rack which is located on YE±1 X1 far side.

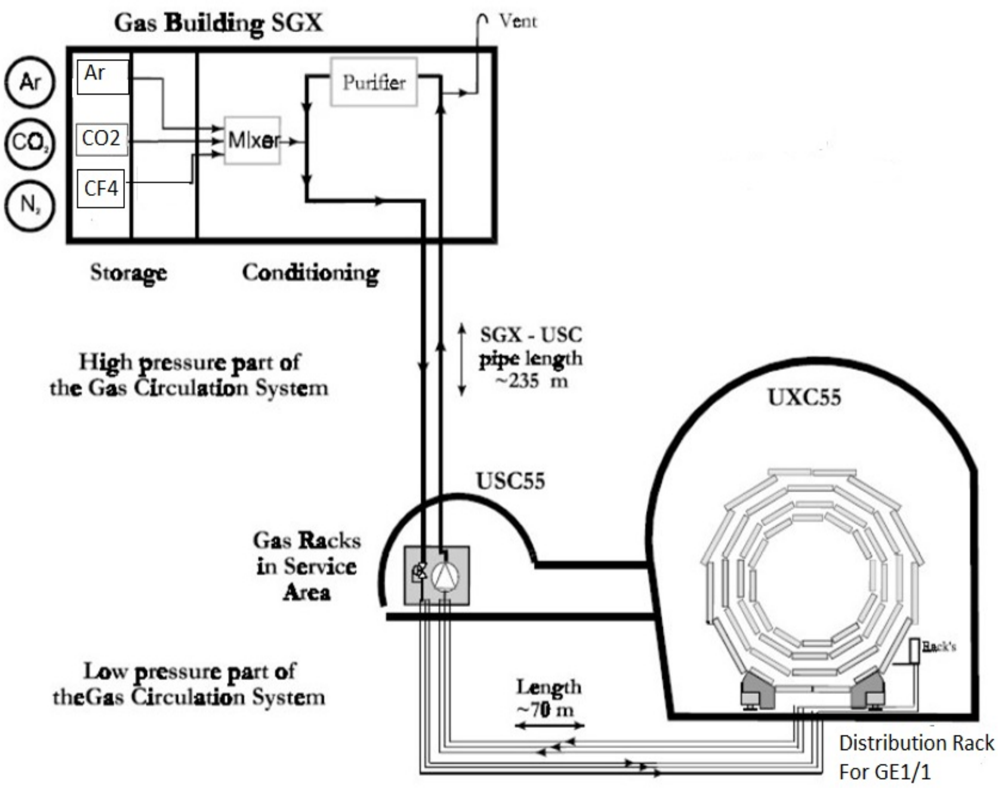

Figure 7.11: Overview of the GE1/1 Gas system

In Fig. 7.11 is shown the overview of the gas supply system for the GE1/1 Gem detectors. The main gas mixer with the supply cylinders is placed in the gas building located on the surface. The composed $ArCO_2CF_4$ $45 - 15 - 40\%$ mixture is transported to the detector cavern tough a 254 m long transfer pipe made of 30 mm stainless steel which runs in the PM54 shaft and connects the surface gas building with the Gas racks Service in USC55.

7.8 Cooling System

The YE1/1 cooling circuit is shown in fig. 7.12 where we can see the 12 cooling loops for the ME1/1, RE1/1 and the RBX. The GE1/1 project will use the RE1/1 place for the cooling.

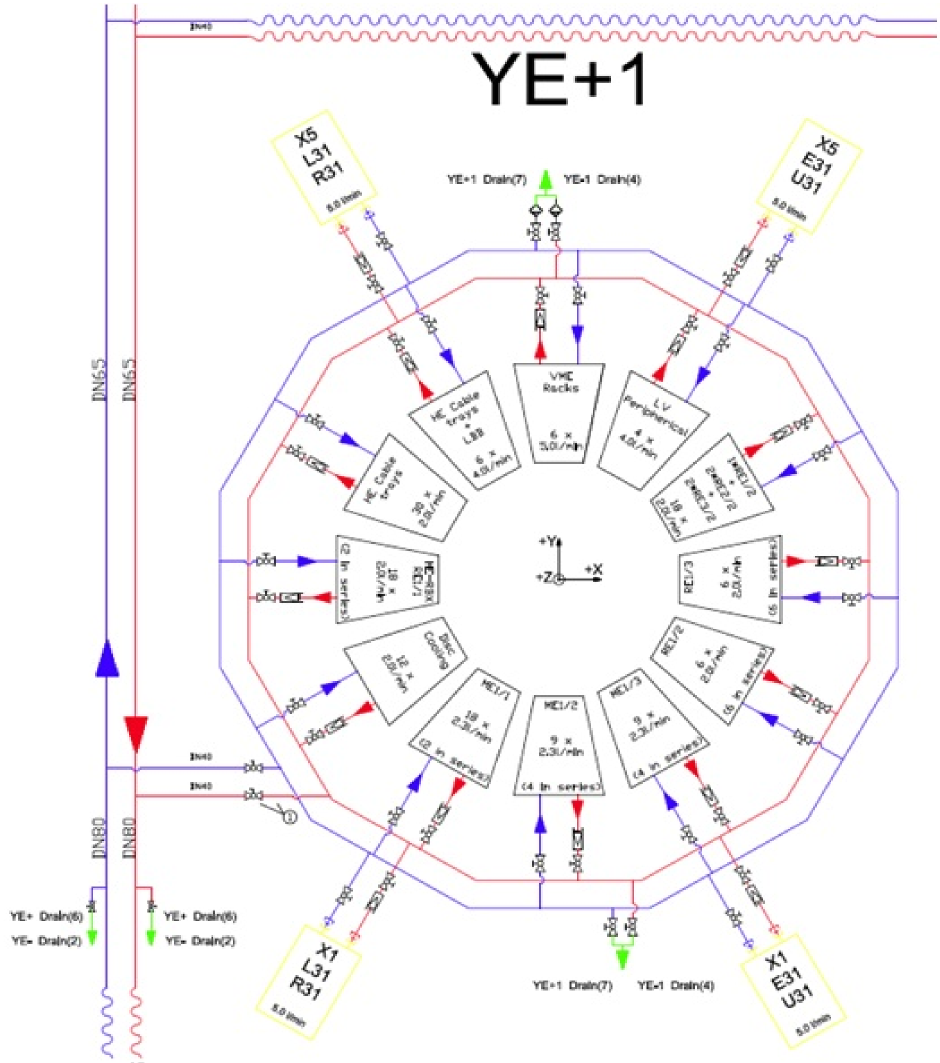

Figure 7.12: Overview of the YE1/1 cooling circuit

In fig. 7.13 is shown one of the 12 cooling loops from the YE1/1 circuit. There we can see that the GE1/1 super-chambers are connected in serial with the RBX. The amount of cooling power per super-chamber is planned to be 240W with included extra margins. This will give a negligible impact to the present cooling system of the endcap and will not perturbate the work of the near by sub-detector systems.

7.9 Database

Cable mapping in database

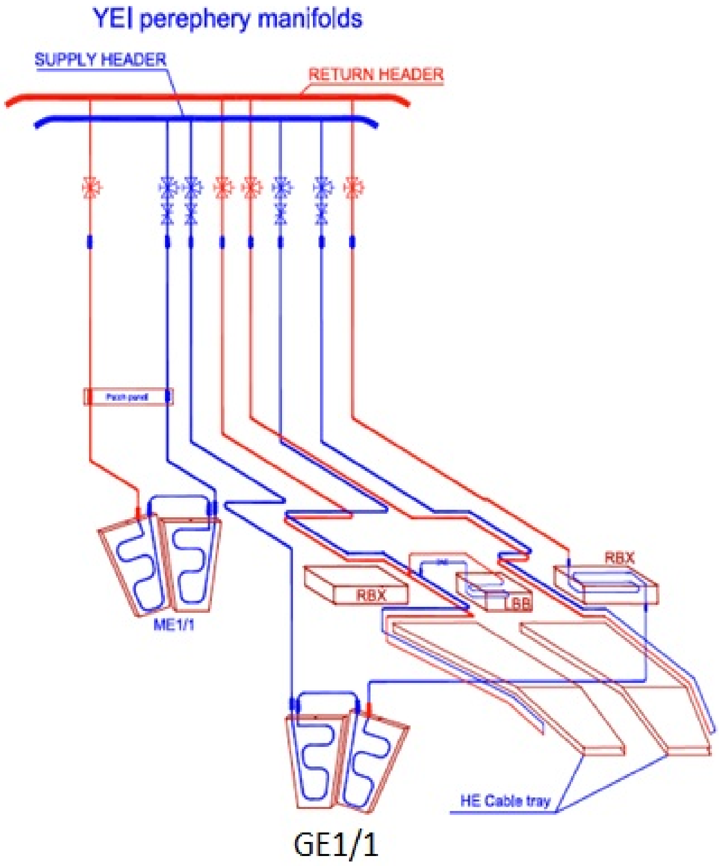

Figure 7.13: Overview of single YE1/1 cooling loop

7.10 Commissioning

Chapter 8

Controls and Monitoring

Editors: A. Cimmino, M. Maggi

8.1 Introduction

The dimensions and complexity of the GEM system demand a high level of automation to reduce human errors and optimize recovery procedures. At CMS, safe operation of the experiment and monitoring of detector status and performance is carried out by the Detector Control System (DCS). Data quality and certification of reconstructed data, instead, is a tasked covered by the and Data Quality Monitoring (DQM) system. Both these systems provid a homogeneous environment across various subdetector and trigger monitoring applications allowing each subsystem to design and implement its own the monitoring and control function depending on thier specific needs. Data from each subsystem are made available to central control systems which, in return, provides console hardware and software, archiving and other higher level services. In the following chapter, the design and implementation of both DCS and DQM systems for the GEM sub-detector are presented.

8.2 Detector Control System

The CMS Detector Control System (DCS) [15] provides complete control over all subdetectors, all infrastructure, services, its active elements, the electronics on and off the detector, the environment at and in proximity of the experiment, as well as communications with the accelerator. All of these tasks are historically referred to as "slow controls" and include: handling the power supply to the detector, control of cooling facilities, environmental parameters, gas system, crates, and racks, as well as safety related functions. The DCS is integrated in the DAQ system [16] (see chapter **??**) as an independent partition and, during data taking, it is supervised by the Run Control and Monitoring System [17].
The RCMS controls the subdetector and central data acquisition systems. It provides the hierarchical control structure needed to control around O(10^4) applications that in turn control electronics or handle the event building and processing. The applications themselves are developed using the C++ based XDAQ [18] data acquisition framework, that provides hardware access, powerful data transport protocols and services. XDAQ is a software platform designed at CERN specifically for the development of distributed data acquisition systems. XDAQ is a middleware that eases the tasks of designing, programming and managing data acquisition applications by providing a simple, consistent and integrated distributed programming environment. The interconnection among DCS, RCMS, DAQ, and XDAQ is schematically shown in figure 8.1

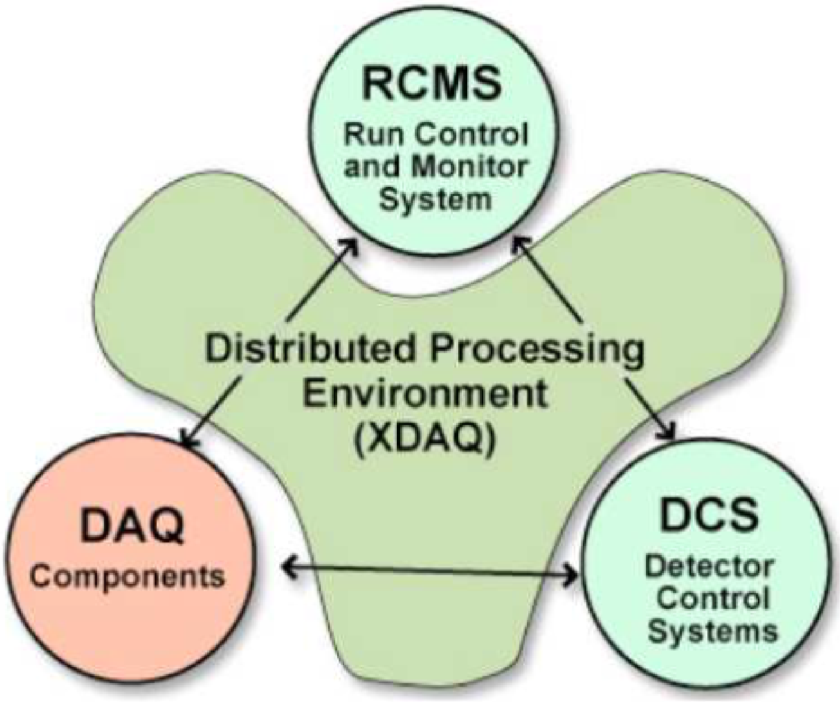

Figure 8.1: Schema of the interconnection among DCS, RCMS, DAQ, and XDAQ. [19]

A general set of system requirements for DCS are: partitionability, modularity, homogeneity, scalability, automation and radiation tolerance. Further more, the high radiation and magnetic field make the experimental hall non-accessible in running conditions. Therefore, the control system must be fault-tolerant and allow remote diagnostics. Many of its functinalities are needed at all time. To ensure this continuity UPS and redundant software and hardware systems are implemented in critical areas. Besides these general requirements, each subdetector has some specific ones resulting from its unique design and implementation. Requirements specific to the GEM sub-detector will be discussed in the following section.

8.2.1 GEM Detector Control System

The GEM Detector Control System (GDCS), provides continuous control and monitoring of the detector, the trigger, and all ancillary sub-systems (high voltages, low voltages, environmental, gas, and cooling). It takes appropriate corrective and automatic actions when pathological conditions are detected to maintain operational stability and ensure high quality data. It monitors and controls the environment at and in proximity of the experiment, handling electricity supply, cooling facilities, environmental parameters, crates, and racks. Also, safety related functions such as detector interlock are foreseen by the GDCS in collaboration with the Detector Safety System (DSS) [20**?**]. The DSS, in fact, provides uninterrupted and autonomous detector protection in case of major hazards such as fire, gas leakage, or oxygen deficiency. It should be noted, at this point, that the GDCS is not designed to be a personnel safety system.
The GDCS is hierarchically organized in a tree-like structure and divided in sub-components: High Voltage (HV), Low Voltage (LV), environmental (humidity, temperature, and pressure), front-end electronics, gas, and cooling systems. Each component can work standalone, or in parallel distributed over different machines. A supervisor level is required in order to gathers and summarizes all information and present it in a simplified but coherent interface to the operators. The architecture of each sub-system can be divided in Front-End (FE) hardware com-

ponents (i.e. sensors, actuator, power supplies, etc) located around all experimental area, and a Back-End (BE) system, composed by the DCS computers network and software applications. Because of the large variety of equipment to be controlled, the standardization of the hardware and of the software interfaces is of primary importance for the homogeneous control of all different detector components. It assures the development of a uniform operator interface as well as minimizes the implementation and maintenance efforts. In accordance with CMS official guidelines, all back-end applications are developed using the commercial Simens SCADA (Supervisory Control And Data Acquisition) [21] software, SIMATIC WinCC Open Architectura (WinCC OA) [22] and the Joint Control Project (JCOP) framework components [23] designed to enhance WinCC OA functinalities. JCOP includes componets to control and monitor the most commonly used hardware at the LHC experiments, effectively the reducing development effort and creating a homogeneous system at the same time. It also defines guidelines for alarm handling, control access, and partitionin to facilitate the coherent development of sub-detector specific components in view of their integration in the central sytem.
The GDCS offers onlines monitoring and control of the values and currents of all HV and LV channel, of the temperatures sensors, gas flow and composition, and front-end and trigger configuration parameters. All this information regarding running conditions and logging, refered to as conditions data, needs to be stored in order to monitor system behavior over time and off-line analysis. The GDCS stores conditions data in the CMS Online Master Data Storage (OMDS), used by all the online subsystems. In its final configuration, the amount of GDCS data stored should be $\sim$ 5 GBytes/year. These data are not easily searchable and viewable from outside the CMS site due to security restrictions. A natural method to convey and display this information is through a web server. Thus, a Web Based Monitoring (WBM) tool, which uses Apache Tomcat application container [24] [25] and Java Servlet technology, is in place and accessible via web browsers for collaborators locally and remotely, anywhere and anytime.

8.2.2 GEM Finite State Machine

Detector controls are organized in a tree-like Finite State Machine (FSM) hierarchy representing the logical structure of the detector, where commands flow down and states and alarms are propagated upwards. FSMs offers an easy and powerful way to model detector behavior through the definition of a finite number of states, transitions, and actions. All the subdetectors control systems are integrated in a single control tree headed by the central DCS to ensure a homogeneous and coherent experiment operation. States and commands for top and conjunction nodes are fixed by CMS in order to have a uniform structure. The states are: ON, OFF, STANDBY, and ERROR and the commands are: ON, OFF, and STANDBY. This ensures uniformity and compatibility with the central DCS, permitting adequate transitions between the states. During a transition between states, the FSM takes care of loading the correct parameter values and alarm settings from the configuration database. Figure 8.2 describes the FSM schema for a high voltage (HV) channel. The “transitional” states, RAMPING UP and RAMPING DOWN, describe the situation in which one or more HV channels are ramping in voltage towards the setted value.

8.3 Data Quality Monitoring System

The CMS Data Quality Monitoring (DQM) framework [26] provides, within the more general CMS framework, common tools for creation, filling, storage, and visualization of histograms and scalar elements. It offers standardized algorithms for statistical tests and automated data certication. It is a set of user defined algorithms. It is intended to be used both online, during data taking, and offline, during reconstruction and re-reconstruction stages. Its final purpose

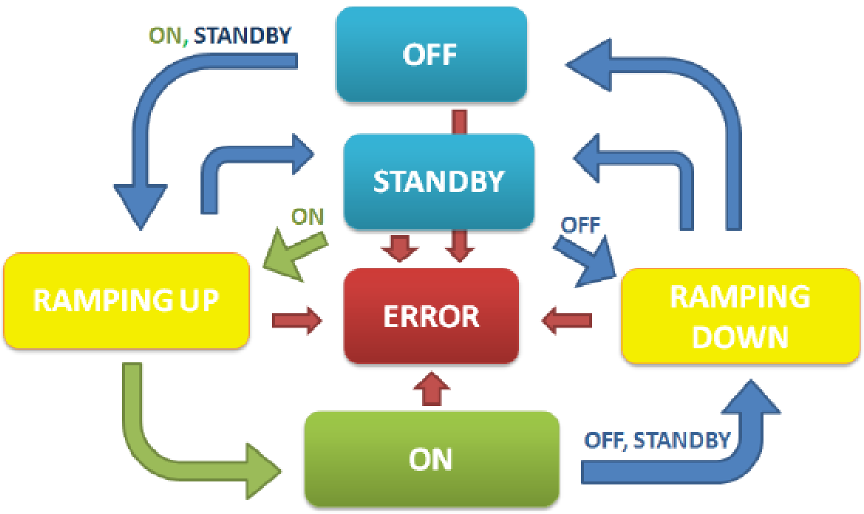

Figure 8.2: FSM schema for a high voltage (HV) channel.

is to monitor and certify the quality of recorded data.

Online DQM applications are an integral part of the event data processing. Each application, usually one per subsystem, receives event data through a dedicated Storage Manager event server. A special stream of events is used to perform DQM operations [27]. The stream contains detector and trigger raw data, Level-1 and High Level Trigger (HLT) summary results, in addition to HLT by-products essential for monitoring trigger algorithms. There is no event sorting nor handling, and no guarantee parallel applications receive the same events. Starting and stopping DQM online applications is centrally managed by the RCMS.

On the other hand, Offline DQM runs as part of the reconstruction process at Tier-0, of the re-reconstruction at the Tier-1s, and of the validation of software releases, simulated data, and alignment and calibration results. Despite the difference in location, data content and timing of these activities, offline monitoring is unique and formally divided into two steps. First, histograms are created and filled while data are processed event by event. The second step is the harvesting when histograms and monitoring information, produced in step one, are extracted and merged to yield full statistics. Efficiencies are calculated, summary plots are produced, and quality tests are performed. The automated data certification decision is taken here.The disadvantage of offline monitoring is the latency of reconstructed to raw data, which can be as long as a several days. On the other hand, the advantages are substantial. All reconstructed events can be monitored and high level quantities are available. This allows for rare or slowly developing problems to be identified.

8.3.1 Architecture of the GEM DQM System

The GEM DQM system is developed within the compass of the CMS reconstruction and physics analysis software framework, CMSSW, and is based on object-oriented programming languages: C++ and Python. It has been designed to be flexible and easily customizable so to be used within different monitoring environments: online/offline DQM and standalone programs for private analyses. Every data analysis and monitoring algorithm is implemented in a separate module, completely independent from the others. Each module inheritates from the parent class DQMEDAnalyzer specifically designed for monitoring purposes. Modules may be added or eliminated from the monitoring sequence at need. Different parameter configuration

files allow to run on both detector and simulated date without requiring code changes nor re-compilation. The modules have been organized in a source/client structure.
Source modules access information on an event-to-event basis, define the quantities to be monitored, and fill histograms. Histograms are defined for each chamber η partition and for each ring. Event selection is performed at this level using specific trigger paths. Offline applications instead run on muon enriched samples during the event-reconstruction stage. Client modules, instead, periodically access the histograms and perform analyses. Frequency of the access depends on the monitored quantity, varying from every luminosity section to once a run. Clients have the tasks of: creating summary histograms, performing quality tests, calculating alarm levels, saving the output in ROOT files, and taking a preliminary data certification decision.
Histograms are organized in a hierarchical tree-like folder structure reproducing detector geometry. The parameters monitored are: single hit multiplicity, bunch crossing, number of reconstructed hits, cluster size, occupancy, and detection efficiency. These parameters are monitored for each chamber eta-partion and it is possible to monitor each signal channels individually. This summs up to few thousand histograms and navigating through them is complicated for non-experts. Therefore, special layouts containing only summary histograms are prepared for both GEM and central DQM shifters, thus allowing the shift crew to quickly identify problems and take action. These histograms are meaningful, not overwhelmed with information and equipped with a clear set of instructions. Reference histograms may be superimposed and Quality Tests (QT) are applied. QTs are standardized and integrated within the CMS DQM framework. They include among others: comparison with reference histogram using ROOT χ^2 algorithm and ROOT Kolmogorov algorithm, check that histogram contents are between (Xmin,Xmax)/(Ymin,Ymax), evaluation of the fraction of bins whose content is above a threshold, compared to neighboring ones fraction of bins that passed the test, and test that the mean value is within expected range.

8.3.2 DQM Graphical User Interfaces

DQM output, which includes histograms, alarm states and quality test results, is made available in real time to a central graphical user interface (GUI) [28], accessible form the web. Being web-based, this central GUI permits users all over the world to access the data and check results without installing experiment specific software. Monitoring data is also stored to ROOT files periodically during the run. At the end run, final result files are uploaded to a large disk pool on the central GUI. Subsequently, files are merged to larger size and backed up to tape. Recent monitoring data (several months worth) are cached on disk for easy access. The GUI was custom built to fulfill the need of shifters and experts for efficient visualization and navigation of DQM results and not meant as a physics analysis tool. A selected view of the CMS DQM GUI may be seen in figure [**?**]

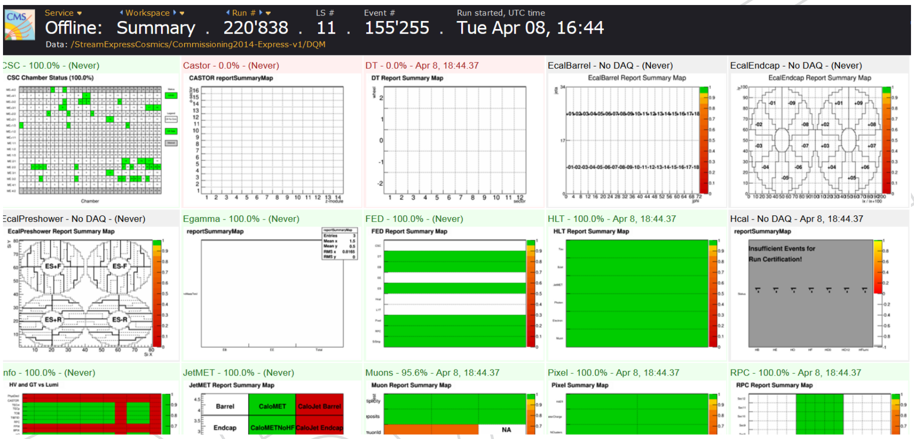

Figure 8.3: Selected view of the CMS DQM GUI.

Chapter 9

Project Organization, Schedule and Costs

Editors: The GEM Project Management

9.1 Participating institutes

9.2 Organization

The proto-collaboration pursuing the GEM upgrade project for CMS described here constituted itself during the CMS week in March 2011 as the "GEM Collaboration (GEMs for CMS)". We anticipate that the collaboration will rename itself simply as CMS GEM Collaboration (in analogy to the CMS DT, RPC, and EMU collaborations) if this technical proposal is accepted and the project moves forward. This international proto-collaboration currently comprises 20 institutions and ≈ 120 collaborators with 19 of the 20 institutions full CMS institutions and one associated institution. Ten additional CMS institutions have signaled their interest in joining the collaboration by signing this technical proposal.

An overview of its current organizational structure is shown in the organigram[1] in Fig.9.1.

An interim management board was formed at the time of constitution that comprises the interim project manager, Archana Sharma (CERN), and her interim deputy, Michael Tytgat (Gent), and the interim chair of the collaboration board (Marcus Hohlmann, Florida Tech). Duccio Abbaneo (CERN) served as interim deputy chair of the collaboration in 2011, but cannot continue due to other obligations at CERN. A new interim deputy chair is to be named by the proto-collaboration in early 2012. Technical working groups on detector issues and software issues were formed that report to the project managers. Financial issues related to production and testing of prototypes are being overseen by a resource manager. A Publications and Conference Board coordinates review and submission of abstracts and proceedings to relevant conferences via the CMS CINCO system. In 2011, the collaboration contributed presentations to eight international conferences and published six proceedings papers. Project managers, resource manager, and Publication & Conferences Board report to the institution board.

[1] For this document the author list has been broadened to include collaborators who support the proposal and may join the project in future, while the structure and size of the collaboration that has carried out the feasibility studies so far is described here.

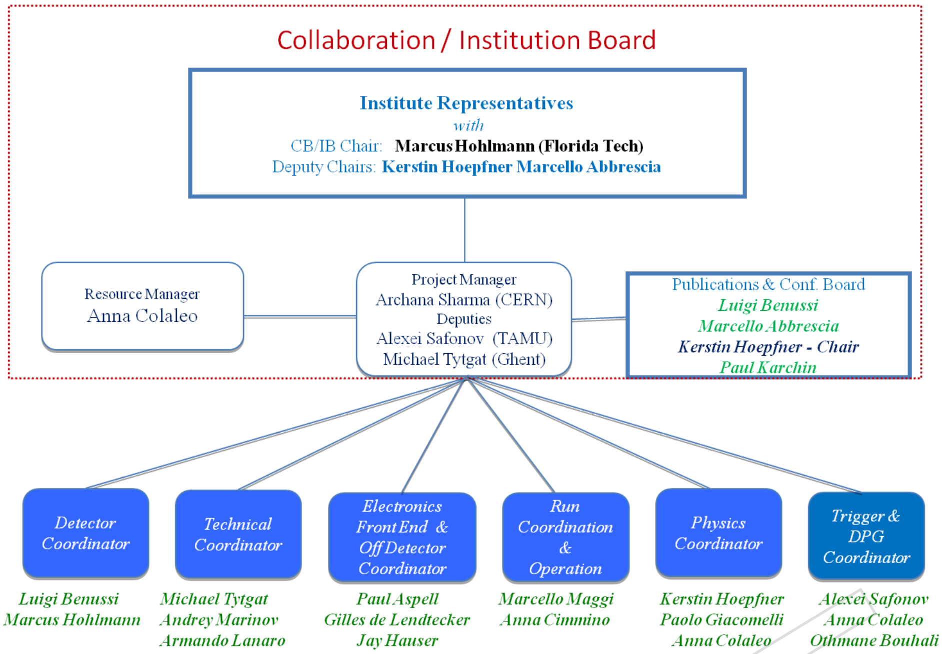

Figure 9.1: Current organigram of the proto-collaboration.

A twiki page (`https://twiki.cern.ch/twiki/bin/view/MPGD/CmsGEMCollaboration`) has been set up to facilitate communication within the proto-collaboration. It provides, for example, links to the conference contributions and publications produced by the proto-collaboration.

9.3 Construction responsibility

9.4 Schedule and Milestone

The overall schedule for the production of two stations GE1/1 and GE2/1 is presented (next page) as a function of months and years from the approval of the construction project. It is assumed that the production of GEM foils will take place at CERN in the surface treatment workshop, as explained in Sect. **??**.

The two stations will be launched as soon as the project is approved and it is estimated that assembly tests and quality control procedures will be completed in two years per station. We will have two assembly lines in the new workshop and the TIF. Detector tests with final electronics will be done after the delivery of the final electronics in a final stage before installation in LS2.

Distributing the detector assembly in different sites and institutions to optimize time and resources has been considered. Detailed plan of sharing the tasks will be made after project approval.

The major milestones are shown in Table 9.1.

9.5 Estimated Costs

The budget and resources are shown in Table 9.2 for the construction of 160 Triple-GEM detectors. The price of the GEM foils has been largely reduced recently due to technological advances in the last two years. With most of the fabrication taking place at CERN using the new

Table 9.1: Summary of milestones.

Milestones	**Activities**	**Time (months)**	Time (years)
Milestone 1	Baseline detector validation	11	0.9
Milestone 2	Construction of 36 GE1/1 SuperChambers (SC)	28	2.3
Milestone 3	Construction of 36 GE2/1 SuperChambers (SC)	32	2.7
Milestone 4	VFAT final validation	24	2
Milestone 5	Board production	19	1.6
Milestone 6	Assembly and QC	28	2.3
Milestone 7	Final QC	27	2.3
Milestone 8	Installation	40	3.3

assembly and production facilities being prepared (see Section **??**), the drift planes, readout planes and the complete detector assembly will be done under one roof lending an optimization of the resources shown under the heading “Detectors”.

The quality control of the detectors will be done as explained in Section **??** and the relevant cost is shown under the heading of ’Chamber QC’. The installation of the two stations and services namely gas and cooling, comprise a large fraction of the costs as explained in items 3-6. These costs are extrapolated from the actual costs incurred in the installation and commissioning of the RPC stations.

The total cost is 7.5 MCHF, of which 4 MCHF is the cost of electronics. The number of channels that have been considered is 270 K for the GE1/1 station and 2.5 million for the GE2/1 station to enhance also the tracking and triggering option in the best possible manner, as discussed in Section **??**. The cost for number of channel is marginal once the initial cost for electronics developments have been incurred.

The participating institute await the approval to approach their respective funding agancies for commitment to the project and initial indications are positive. In comparison the present RPC system readout is 70 K channels for the barrel and 40 K channels in the forward system.

[1]To be done based on the granularity ≈1.5 times electronics for GE1/1.
[2]Electronics to be added.
[3]Electronics for the GE2/1 to be added.

Table 9.2: Budget and resources based on previous experience. We have considered approximately 2.2 MCHF for the electronics; this includes approximately 522 kCHF for the front-end ASIC silicon cost.

Item	GE1/1 80 detectors GE2/1 160 detectors	GE1/1 [kCHF]		GE2/1 [kCHF]		GE1/1 & GE2/ [kCHF]
	Deliverables	**price/detector**	**tot station**	**price/detector**	**tot station**	**tot price**
1	DETECTORS	5	400	5	800	1200
	Readout circuits	0.4		0.4		
	GEMs and drift planes	3.6		3.6		
	Drift board	0.5		0.5		
	Frames	0.05		0.05		
	Detector assembly	0.3		0.3		
	HV, connectors	0.05		0.05		
	Testing	0.1		0.1		
2	CHAMBER QC		500		500	1000
	Infrastructure at site		220		220	
	Assembly consumables		100		100	
	QC tools		130		130	
	Shipments		50		50	
3	INSTALLATION		350		350	700
	Consumables		50		50	
	Mechanics / tooling		100		100	
	Commissioning		150		150	
4	GAS SYSTEM		50		50	100
5	COOLING		50		50	100
6	ELECTRONICS		1900		[1]	1900[1]
	On-detector		1000		1500	
	Off-detector		900		1350	
	SUB TOTAL		**3250**		**1750**[2]	
	GRAND TOTAL	**5 MCHF**[3]				

Appendix A

The GE1/1 Slice Test

Editors: H. Hoorani, A. Marinov, M. Tytgat

A.1 Introduction

Description of slice test, motivation, goals

In June 2013, CMS approved the installation of a limited number of GE1/1 chambers into the muon endcaps, in order to gain first operational experience with this new subsystem and also to demonstrate the integration of the GE1/1 chambers into the trigger. During the 2016-2017 Year-End Technical Stop, 2 (4?) GE1/1 superchambers covering a 20° sector will be installed in YE1/1, at the location depicted in Fig. A.1.

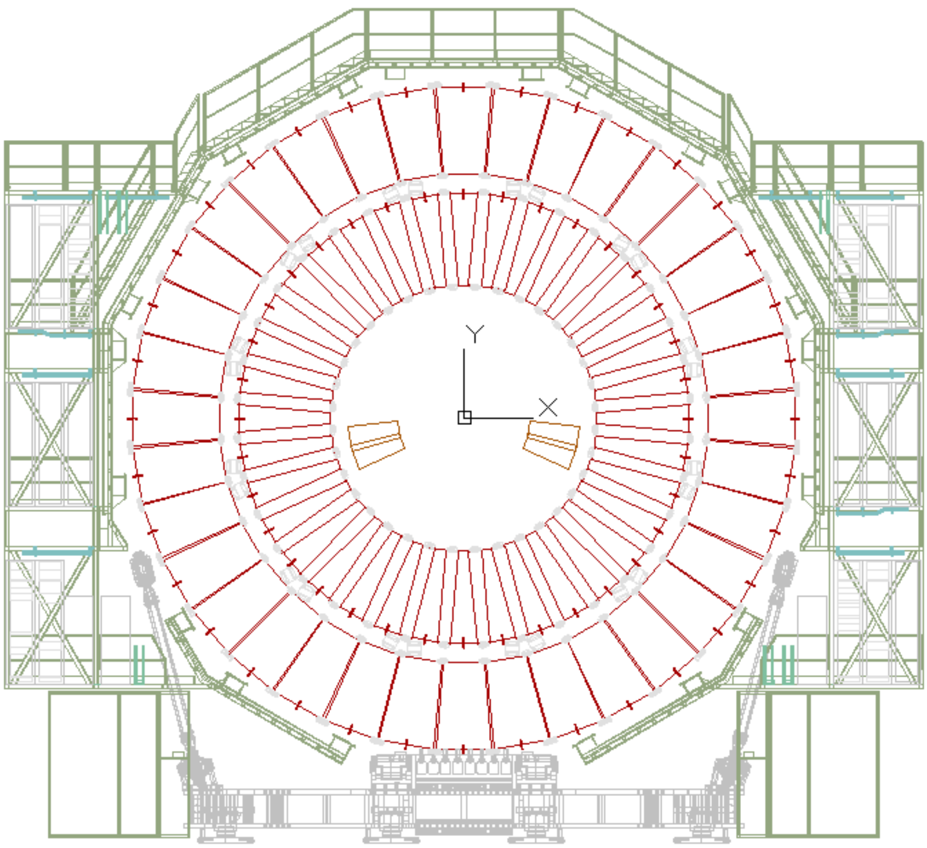

Figure A.1: Location of the Slice Test GE1/1 superchambers in YE1.

A.2 Detector Configuration

detectors and services

As described in Chapt. 7, during LS1, most (all ?) of the required services and cabling for the GE1/1 station will be in place and tested. With few exceptions, the final GE1/1 services and cabling configuration will be used for the Slice Test chambers as well.

Given the installation of the Slice Test chambers at the end of 2016, the construction and commissioning of the GEM gas mixer will be completed latest after the Summer in 2016. For the Slice Test, a gas flow of about 10l/h, for a total detector volume of about 20l is foreseen.

The front-end electronics power dissipation for the Slice Test detectors is assumed to be less than 250W in total for the 2 superchambers. This will have a negligible impact on the presently available YE1 cooling system.

A.3 Front-end Electronics and DAQ

Due to the still ongoing developments of the front-end chip and GBT chip set in the coming years, it is foreseen that the readout of the chambers during the Slice Test will be close to but nonetheless slightly different from the final system that is described in Chapt. 3. The on-detector electronics will be based on the VFAT2 instead of VFAT3 ASIC, and on the 2nd instead of the final (3rd) version of the GEB and opto-hybrid. The latter will already include the GBT chip set.

Since the VFAT2 design is not compatible with the GBT chipset all the data (trigger and tracking data) will transit through the front-end FPGA (Virtex 6) located on the opto-hybrid. The number of optical links per detector will be the same as in the LS2 system. The trigger data link towards the CSC TMB will also be the same as the LS2 system.

For the back-end electronics, the system should be the same as for the LS2 installation but with less components : one μTCA crate hosting one MP7 board and one AMC13 board.

A.4 Online Monitoring Tools

Appendix B

Integrated Charge Estimation

Here we briefly detail the estimation of the charge per area that will be integrated in the GE1/1 chambers over a lifetime of 20 years at the HL-LHC as stated under the design requirements in section 2.1.1. The integrated charge Q_{int} per area is given by:

$$Q_{int} = R_{max} \times n_{tot}^{ion} \times g \times e \times t_{HL-LHC} \,, \tag{B.1}$$

where R_{max} is the maximum charged-particle hit rate per area produced by all particles incident on the chamber, n_{tot}^{ion} is the total number of ion-electron pairs produced by charged particles traversing the drift gap in the chamber, g is the gas gain of the GE1/1, e is the electron charge, and t_{HL-LHC} is the total time in seconds that the HL-LHC will be providing collisions over 20 years.

We use R_{max} = 5 kHz/cm^2 as the rate estimate in the hottest area of the GE1/1 and $g = 2 \times 10^4$ as the typical gas gain value for a Triple-GEM. In an Ar/CO_2 70:30 gas mixture, on the average 93 ion-electron pairs are produced per cm. The largest path length l in the GEM drift gap that occurs for ionizing particles when they traverse the GE1/1 is $l = d/\cos\theta$. Here $d = 0.3$ cm is the drift gap of the Triple-GEM and $\theta \approx 25^o$, which corresponds to $\eta = 1.5$, is the largest angle relative to the normal onto the chamber under which particles are incident on the GE1/1. This gives l =0.33 cm and $n_{tot}^{ion} = 31$ ion-electron pairs in the GE1/1. Assuming that the HL-LHC will have an annual duty factor of $\approx 1/3$ as is typical for collider operations, we estimate that the chambers will be exposed to charged particles for $\approx 10^7$ seconds each year.

Multiplying these factors together, we find an estimated integrated charge per area for a projected GE1/1 lifetime of 20 years of:

$$\mathbf{Q_{int}} \approx 5 \cdot 10^3\, s^{-1} cm^{-2} \times 31 \times 2 \cdot 10^4 \times 1.6 \cdot 10^{-19}\, C \times 20 \cdot 10^7\, s = \mathbf{99\ mC/cm^2} \tag{B.2}$$

Gas mixtures containing in addition CF_4 in any percentage will produce very similar integrated charges because the total ionization of CF_4 (100 pairs/cm) is quite close to that of Ar (94 pairs/cm) and CO_2 (91 pairs/cm). Specifically, for Ar/CO_2/CF_4 45 : 15 : 40 the total ionization is 96 pairs/cm which gives Q_{int} = 101 mC/cm^2 for the GE1/1.

References

---

[1] COMPASS Collaboration, "The COMPASS experiment at CERN", *Nucl.Instrum.Meth.* **A577** (2007) 455–518, `doi:10.1016/j.nima.2007.03.026`, `arXiv:hep-ex/0703049`.

[2] B. Ketzer et al., "A triple-GEM Detector with pixel readout for high-rate beam tracking in COMPASS", *IEEE Nucl.Sci.Symp.Conf.Rec.* (2007) 242–244, `doi:10.1109/NSSMIC.2007.4436323`.

[3] W. Anderson et al., "Design, Construction, Operation and Performance of a Hadron Blind Detector for the PHENIX Experiment", *Nucl.Instrum.Meth.* **A646** (2011) 35–58, `doi:10.1016/j.nima.2011.04.015`, `arXiv:1103.4277`.

[4] B. Surrow, "The STAR forward GEM tracker", *Nucl.Instrum.Meth.* **A617** (2010) 196–198, `doi:10.1016/j.nima.2009.09.012`.

[5] TOTEM Collaboration, "Performance of the TOTEM Detectors at the LHC", *Int.J.Mod.Phys.* **A28** (2013) 1330046, `doi:10.1142/S0217751X13300469`, `arXiv:1310.2908`.

[6] A. Cardini, G. Bencivenni, and P. De Simone, "The Operational Experience of the Triple-GEM Detectors of the LHCb Muon System: Summary of 2 Years of Data Taking", *IEEE Nucl.Sci.Symp.Conf.Rec.* (2012) 759–762.

[7] D. Abbaneo et al., "An overview of the design, construction and performance of large area triple-GEM prototypes for future upgrades of the CMS forward muon system", *JINST* **7** (2012) C05008, `doi:10.1088/1748-0221/7/05/C05008`.

[8] D. Abbaneo et al., "Characterization of GEM Detectors for Application in the CMS Muon Detection System", *IEEE Nucl.Sci.Symp.Conf.Rec.* **2010** (2010) 1416–1422, `doi:10.1109/NSSMIC.2010.5874006`, `arXiv:1012.3675`.

[9] D. Abbaneo et al., "Test beam results of the GE1/1 prototype for a future upgrade of the CMS high-η muon system", *IEEE Nucl.Sci.Symp.Conf.Rec.* **2011** (2011) 1806–1810, `doi:10.1109/NSSMIC.2011.6154688`, `arXiv:1111.4883`.

[10] D. Abbaneo et al., "Beam Test Results for New Full-scale GEM Prototypes for a Future Upgrade of the CMS High-eta Muon System", `doi:10.1109/NSSMIC.2012.6551293`, `arXiv:1211.3939`.

[11] V. Bhopatkar et al., "Beam Test of a Large-Area GEM Detector Prototype for the Upgrade of the CMS Muon Endcap System", *presentation at annual April meeting of Am. Phys. Soc., available in CMS CINCO repository* (2014).

[12] D. Abbaneo et al., "The status of the GEM project for CMS high-η muon system", *Nucl.Instrum.Meth.* **A732** (2013) 203–207, doi:10.1016/j.nima.2013.08.015.

[13] M. Tytgat et al., "Construction and Performance of Large-Area Triple-GEM Prototypes for Future Upgrades of the CMS Forward Muon System", *IEEE Nucl.Sci.Symp.Conf.Rec.* **2011** (2011) 1019–1025, doi:10.1109/NSSMIC.2011.6154312, arXiv:1111.7249.

[14] P. Moreira et al., "The GBT-SerDes ASIC prototype", *Journal of Instrumentation* **5** (2010), no. 11, C11022.

[15] R. Arcidiacono et al., "CMS DCS design concepts",.

[16] G. Bauer et al., "The run control and monitoring system of the CMS experiment", *PoS* **ACAT** (2007) 026, doi:10.1088/1742-6596/119/2/022010.

[17] CMS Collaboration Collaboration, "CMS: The TriDAS project. Technical design report, Vol. 2: Data acquisition and high-level trigger",.

[18] V. Brigljevic et al., "Using XDAQ in application scenarios of the CMS experiment", *eConf* **C0303241** (2003) MOGT008, arXiv:hep-ex/0305076.

[19] C. Collaboration, "CMS trigger and data-acquisition project: Technical Design Report",.

[20] S. Schmeling, B. Flockhart, S. Luders, and G. Morpurgo, "The detector safety system for LHC experiments", *IEEE Trans.Nucl.Sci.* **51** (2004) 521–525, doi:10.1109/TNS.2004.828631.

[21] A. Daneels and W. Salter, "What is SCADA?", *Conf.Proc.* **C991004** (1999) 339–343.

[22] "SIMATIC WinCC Open Architectura".

[23] M. Gonzalez-Berges, "The Joint COntrols project framework", *eConf* **C0303241** (2003) THGT006, arXiv:physics/0305128.

[24] "Axis is an XML based Web Service Framework".

[25] "The Apache Tomcat Servlet container".

[26] L. Tuura, A. Meyer, I. Segoni, and G. Della Ricca, "CMS data quality monitoring: Systems and experiences", *J.Phys.Conf.Ser.* **219** (2010) 072020, doi:10.1088/1742-6596/219/7/072020.

[27] CMS Collaboration Collaboration, "Commissioning of the CMS High-Level Trigger with Cosmic Rays", *JINST* **5** (2010) T03005, doi:10.1088/1748-0221/5/03/T03005, arXiv:0911.4889.

[28] L. Tuura, G. Eulisse, and A. Meyer, "CMS data quality monitoring web service", *J.Phys.Conf.Ser.* **219** (2010) 072055, doi:10.1088/1742-6596/219/7/072055.